



POLITECNICO
MILANO 1863

SCUOLA DI INGEGNERIA INDUSTRIALE
E DELL'INFORMAZIONE

A multi-physics oxygenation model: from biological derivation to the numerical simulation of real-life scenarios

TESI DI LAUREA MAGISTRALE IN
MATHEMATICAL ENGINEERING - INGEGNERIA MATEMATICA

Author: **Manfred Nesti**

Student ID: 953032

Advisor: Dr. Francesco Regazzoni

Co-advisors: Dr. Pasquale Claudio Africa, Dr. Ivan Fumagalli

Academic Year: 2021-22

Abstract

The myocardium requires a continuous oxygen supply to work properly: oxygenated blood reaches the heart through the coronaries and perfuses the whole muscular tissue, allowing the exchange of oxygen at the microvasculature level. Oxygen delivery can be jeopardized due to reduced flow either because of coronary arteries obstructions, aortic valve regurgitation, or left ventricular hypertrophy, as well as in the case of pathologies such as SARS-CoV-2 infection [93]. The iHEART project represents one of the first attempts in the world to create a complete mathematical model of the human heart and aims to build a digital-twin capable of describing in detail the interactions that take place within it.

This thesis aims at extending the project computational toolbox by introducing an innovative mathematical model of cardiac oxygenation capable of simulating the space-time evolution of quantities such as saturation and oxygen concentration within the cardiac capillaries and muscle tissue. In this work, the oxygenation model is coupled with models governing the fluid dynamics of blood in the coronary arteries and gradually smaller vessels through a perfusion model. The equations characterizing the oxygenation model and their coupling with the other physics were discretized and implemented within the life^x cardiac simulation library [1]. After a careful calibration of the physical parameters so that the model fully reflects the real scenarios, we tested the model through simulations on idealized coronary and myocardial geometries. Finally, through simulations on real geometries, we simulated physiological and pathological scenarios (i.e., patient with SARS-CoV-2 infection), both in the case of a patient at rest and under stress, confirming that the model is in agreement with the literature and an interesting improvement of the state of the art.

Keywords: Cardiac modeling, Cardiac muscle oxygenation, SARS-CoV-2, iHEART, life^x, Partial Differential Equations, Numerical simulations, Computational Fluid Dynamics, Finite Element Method

Abstract in lingua italiana

Il miocardio necessita di un continuo apporto di ossigeno per funzionare correttamente: il sangue ossigenato raggiunge il cuore attraverso le coronarie e percorre tutto il tessuto muscolare, consentendo lo scambio di ossigeno a livello del microcircolo. L'ossigenazione può essere compromessa a causa di flusso ridotto da ostruzioni delle arterie coronarie, rigurgito della valvola aortica o ipertrofia ventricolare sinistra, oppure in caso di patologie come l'infezione da SARS-CoV-2 [93]. Il progetto iHEART rappresenta uno dei primi tentativi al mondo di creare un modello matematico completo del cuore umano e mira a costruirne una copia virtuale in grado di descrivere minuziosamente le interazioni che avvengono al suo interno.

Questa tesi mira ad estenderne gli strumenti computazionali introducendo un innovativo modello di ossigenazione cardiaca in grado di simulare l'evoluzione spazio-temporale di grandezze quali la saturazione e la concentrazione di ossigeno all'interno dei capillari cardiaci e del tessuto muscolare. In questo lavoro, il modello di ossigenazione è accoppiato con modelli che governano la fluidodinamica del sangue nelle arterie coronarie e nei vasi via via più piccoli attraverso un modello di perfusione. Le equazioni che costituiscono il modello di ossigenazione e il loro accoppiamento con le altre fisiche sono state discritte e implementate all'interno della libreria di simulazione cardiaca life^x [1]. Dopo un'attenta calibrazione dei parametri fisici affinché il modello rispecchi a fondo gli scenari reali, abbiamo testato il modello attraverso delle simulazioni su geometrie idealizzate di coronarie e miocardio. Infine, attraverso delle simulazioni su geometrie reali, sono stati simulati scenari sia fisiologici, sia patologici (i.e., paziente con infezione da SARS-CoV-2), sia nel caso di paziente a riposo, sia nel caso sotto sforzo, confermando che il modello è in accordo con la letteratura ed un interessante miglioramento dello stato dell'arte.

Parole chiave: Modellizzazione cardiaca, Ossigenazione del muscolo cardiaco, SARS-CoV-2, iHEART, life^x, Equazioni alle Derivate Parziali, Simulazioni numeriche, Fluidodinamica computazionale, Metodo degli Elementi Finiti

Contents

Abstract	i
Abstract in lingua italiana	iii
Contents	v
List of abbreviations	vii
1 Introduction	1
1.1 Anatomy	1
1.1.1 Heart anatomy	1
1.1.2 Coronary circulation	3
1.2 Physiology	4
1.2.1 Physiology of the cardiac muscle	4
1.2.2 Physiology of gas exchange and diffusion	6
1.2.3 Respiration and gas diffusion in tissues	8
1.2.4 Physiology of myocardial perfusion and oxygenation	13
1.3 State of the art of mathematical models	17
1.3.1 Models for blood dynamics in epicardial coronary arteries	18
1.3.2 Models for blood dynamics in intramural coronary vessels	20
1.3.3 Models for oxygen exchange in microvasculature	23
2 Mathematical models	31
2.1 Blood dynamics in epicardial coronary arteries	31
2.2 Blood dynamics in intramural coronary vessels	33
2.3 Oxygen exchange in microvasculature	36
2.3.1 Oxygen-hemoglobin association/dissociation	37
2.3.2 Mass conservation	37
2.3.3 Equations in terms of SO_2 and PO_2	41
2.3.4 Oxygen dynamics inside the muscle	43
2.3.5 Parameters calibration	44
2.3.6 Quasistatic-chemistry approximation	47
2.4 Coupling conditions	48
2.4.1 Fluid dynamics and perfusion	49
2.4.2 Oxygenation and perfusion	51
2.4.3 Multi-physics oxygenation problem	52

3 Numerical schemes	53
3.1 Weak formulation	54
3.2 Space discretization	55
3.3 Time discretization	56
3.4 Algebraic formulation	57
3.5 Runge-Kutta method for the 0D model	58
3.6 Oxygen fluxes approximation	60
3.7 Coupling schemes	61
3.7.1 Iterative splitting for fluid dynamics and perfusion	61
3.7.2 One-way coupling between oxygenation and perfusion	63
4 Tests and results	65
4.1 Output of 0D model	65
4.2 Tests on idealized geometry	68
4.2.1 Comparison between complete and reduced 0D model	68
4.2.2 Comparison between 3D and 0D model	70
4.2.3 Comparison between coupled and uncoupled model	72
4.3 Results on real geometries and discussion	77
4.3.1 Comparison between real and idealized geometry	77
4.3.2 Effects of physical activity	84
4.3.3 Effects of SARS-CoV-2 infection	87
4.3.4 Effects of physical activity and SARS-CoV-2 infection	91
5 Conclusions and further developments	95
Bibliography	97
List of Figures	109
List of Tables	111
List of Symbols	113

List of abbreviations

A-V	atrioventricular	H⁺	hydrogen ion
I-V	interventricular	H₂O	water
LAD	left anterior descending coronary artery	CO	carbon monoxide
RCA	right coronary artery	NO	nitric oxide
LCA	left main coronary artery	CO₂	carbonic dioxide
LCX	left circumflex coronary artery	H₂CO₃	carbonic acid
PDA	posterior descending artery	HCO₃⁻	hydrogen carbonate
CBF	coronary blood flow	O₂	oxygen
HR	heart rate	Hb	hemoglobin
RBC	red blood cells	Hb-O₂	oxyhemoglobin
IVR	capillary intravascular resistance	Mb	myoglobin
MTC	mass transfer coefficient		

AE	algebraic equation
ODE	ordinary differential equation
PDE	partial derivative equation
FDM	finite-difference method
FEM	finite-element method
CG	conjugate gradient
Pe	Péclet number

1 | Introduction

In this chapter, we provide some basic notions of anatomy and physiology that we employ in the following chapter. In particular, in Section 1.1 we summarize the anatomic features of the heart and the coronary circulation. In contrast, in Section 1.2, we provide some basic knowledge of cardiac muscle physiology, gas exchange, diffusion, myocardial perfusion, and oxygenation. Finally, in Section 1.3, we review the literature about mathematical models for blood dynamics in epicardial coronary arteries and intramural coronary vessels, and for oxygen exchange in the microvasculature.

1.1. Anatomy

We give some basic notions about the anatomy of the heart in Section 1.1.1 and about the coronary circulation in Section 1.1.2. These are the main anatomical aspects involved in this work, and the given level of details is intended to be enough to understand the following. More details can be found in medical manuals such as [36, 40, 51].

1.1.1. Heart anatomy

The heart is a muscular organ located in the mediastinum, an anatomical region delimited anteriorly by the sternum, posteriorly by the column, and laterally by the lungs. This organ is about 12 cm long, 9 cm wide and 6 cm thick, and is composed of a particular muscular tissue, the myocardium. The muscle is surrounded by a membranous sac, the pericardium, which consists of two parts: a superficial fibrous layer composed of connective tissue that anchors the heart in the mediastinum and a deeper serous layer. The serous pericardium forms a double layer around the heart: the outer-parietal one is fused to the fibrous pericardium, and the inner-visceral one, also called the epicardium, adheres to the surface of the cardiac muscle. The pericardial cavity contains pericardial fluid between the parietal and visceral layers, reducing friction between the pericardial membranes as the heart moves. Finally, the endocardium is a thin connective layer that covers the internal walls of the heart's chambers and valves and is continuous to the endothelial lining of the blood vessels [51].

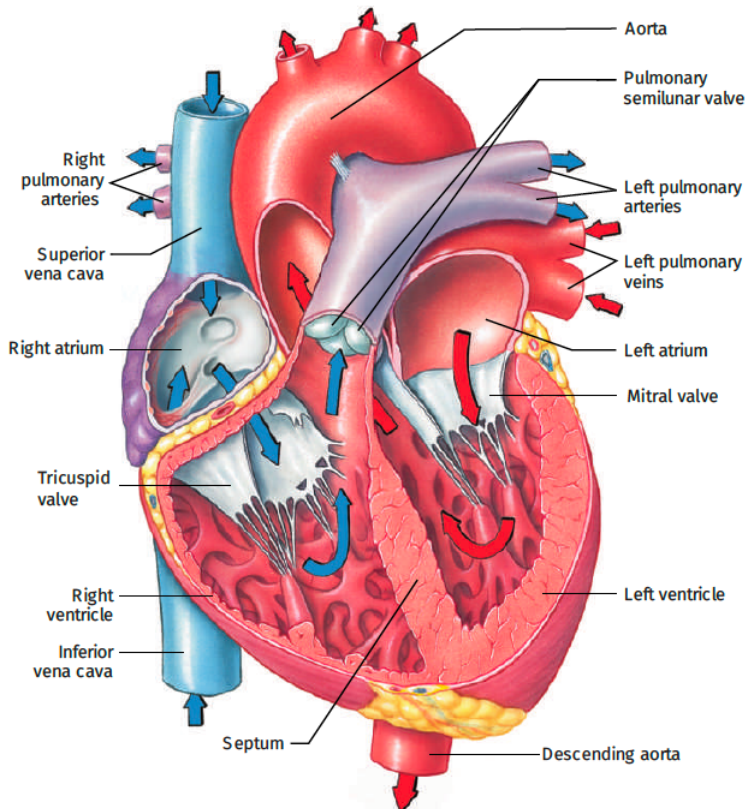


Figure 1.1: Illustration of the human heart [104].

The heart contains four chambers: the two upper chambers are the atria, and the two lower ones are the ventricles. It is functionally divided into two parts: the right and left heart. The right heart receives deoxygenated blood from the systemic veins and pumps it into the pulmonary circulation; the left heart receives oxygenated blood from the pulmonary veins and pumps it into the systemic circulation. Each part consists of an atrium and a ventricle separated by an atrioventricular (A-V) valve, which permits blood to flow in only one direction.

The valve between the right atrium and ventricle is the tricuspid valve, whereas the valve between the left atrium and ventricle is the mitral valve. A semilunar valve separates each ventricle from its corresponding outflow vessel: the pulmonary valve separates the right ventricle from the pulmonary artery. In contrast, the aortic valve separates the left ventricle from the aorta, ensuring a one-way blood flow. The interatrial and interventricular (I-V) septa separate the left and right hearts, which avoid the mixture of oxygenated and deoxygenated blood [51].

1.1.2. Coronary circulation

The heart's blood supply is provided by a specialized vascular structure, the coronary circulation. It originates just above the aortic valve, from the coronary ostia in the sinuses of Valsalva, with two main vessels: the right coronary artery (RCA) and the left coronary artery (LCA) [36, 40].

The RCA arises from the anterior aortic sinus; it passes between the right atrial auricle and pulmonary trunk and descends almost vertically in the A-V groove. It then curves posteriorly, reaching the diaphragmatic surface of the heart, and continues downward in the posterior I-V sulcus. The RCA, with its branches, supplies the right atrium, the right ventricle, a portion of the left ventricle, and the A-V node. The LCA arises from the left posterior aortic sinus; it passes between the pulmonary trunk and the left atrial auricle. It is usually very short: in the proximity of the A-V groove, it bifurcates into two main branches: the left anterior descending artery (LAD) and the left circumflex artery (LCX) [52].

The LAD proceeds along the I-V sulcus. In one-third of specimens, it terminates in the apex, while in most of the population, it passes beyond the apex into the posterior I-V sulcus, where it meets the distal branches of the RCA. The LAD gives rise to several diagonal vessels, which supply the anterior, lateral, and apical portion of the left ventricle, and to the anterior septal perforating arteries, which supply the majority of the I-V septum. The LCX travels along the left part of the A-V groove. From the LCX originate the marginal branches and the left posterolateral branches, which supply the left ventricle's left atrium and the posterior and lateral walls. The posterior descending artery (PDA) is an additional sizeable coronary artery that perfuses a little portion of the I-V septum. The heart is left or right dominant, whether the PDA derives from LCX or RCA. The blood coming from capillaries is drained by the coronary venous system into the coronary sinus, located in the posterior part of the A-V groove on the diaphragmatic surface of the heart. The principal tributaries of the coronary sinus are the great cardiac vein, which drains the left atrium and the ventricles, the middle cardiac vein, which drains the ventricles, the small cardiac vein, which drains the right atrium and ventricle, and the anterior cardiac veins which drain the right ventricle [51]. Then the coronary sinus returns the blood into the right atrium, although some small coronary veins empty directly in the right atrium. Notice that the coronary circulation has no standard pattern: several patterns can be found in each heart.

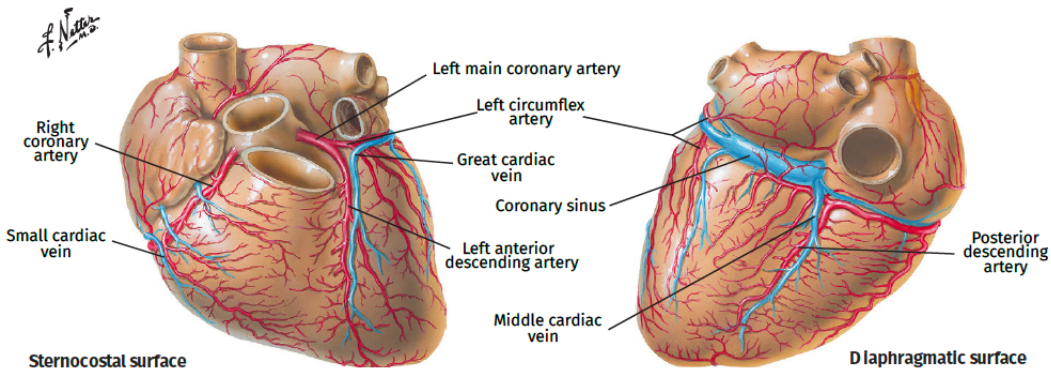


Figure 1.2: Anatomy of the main coronary arteries [40].

1.2. Physiology

In this section, we give some physiological notions required in the next part of this work. In particular, we can find some physiological concepts about

- cardiac muscle in Section 1.2.1;
- gas exchange and diffusion in Section 1.2.2;
- respiration and gas diffusion in tissues in Section 1.2.3;
- myocardial perfusion and oxygenation in Section 1.2.4.

More details can be found in some physiology manuals as [8, 11, 51].

1.2.1. Physiology of the cardiac muscle

Conduction system

Although cardiac muscle is striated, like skeletal muscle, it is involuntary like smooth muscle, and its contraction is triggered by an electrical excitation originating from the heart's natural pacemaker, the sinoatrial node. The source of this electrical activity is a network of specialized cardiac muscle fibers called autorhythmic, which repeatedly and rhythmically generate action potentials that trigger heart contractions [51]. Autorhythmic cells also form a conduction system that delivers action potentials throughout the heart. The electrical signal spreads from the sinoatrial node throughout the atrial muscle, stimulating atrial contraction, and arrives at the A-V node. The A-V node slows down the transmission of the signal, which then enters the bundle of His. It travels through the main bundle branches and a network of conductive tissue, called Purkinje fibers, reaching both the ventricles and stimulating their contraction from the apex to the base [36].

Cardiac cycle

The cardiac cycle comprises all the events associated with one heartbeat. It consists of alternate cardiac muscle contraction and relaxation periods, the systole and the diastole, respectively. In each cardiac cycle, contraction of the atria and then of the ventricles forces blood from areas of higher pressure to areas of lower pressure. As each chamber of the heart contracts, blood pressure within it increases, pushing blood into a ventricle or out of the heart into an artery [51]. The cardiac cycle can be divided into four phases.

- *Ventricular filling and atrial systole.* Once the atrial pressure exceeds the ventricular pressure, the A-V valve opens, allowing blood to flow into the ventricle, which then relaxes and expands while pressure increases slightly. In the last phase of filling, the atrium contracts (atrial systole), contributing to the last 20% of the ventricular filling.
- *Isovolumic contraction.* After the filling phase, the ventricular pressure rises, causing a retrograde flow, which closes the A-V valve. Since both A-V and semilunar valves are closed, the pressure and the tension inside the ventricle rise without changing blood volume.
- *Ventricular ejection.* When the pressure inside the ventricle exceeds the pressure in the outflow vessel (~ 70 mmHg in the aorta and ~ 10 mmHg in the pulmonary trunk), the semilunar valve opens, ejecting the blood into the corresponding circulation. The ventricular volume decreases, but the pressure keeps growing. The pressures of the aorta and the pulmonary trunk increase according to the elastic properties of the arterial wall: at first, the pressure difference between each ventricle and its corresponding outflow artery guarantees a blood acceleration, but when the ventricle stops its active contraction, such pressure difference decreases, and at the end it is reverted, causing a deceleration of the blood. However, the blood continues to flow in the artery because when the active contraction stops, the ventricle releases the accumulated elastic energy, resulting in a passive contraction that allows blood ejection. When, due to deceleration, the blood flow becomes negative, the semilunar valve closes, and blood ejection stops.
- *Isovolumic relaxation.* With both valves closed, the volume remains constant in each ventricle, but the ventricular pressure decreases due to the ventricle relaxation. When the ventricular pressure falls under the atrial pressure, the A-V valve opens, and the cardiac cycle starts again.

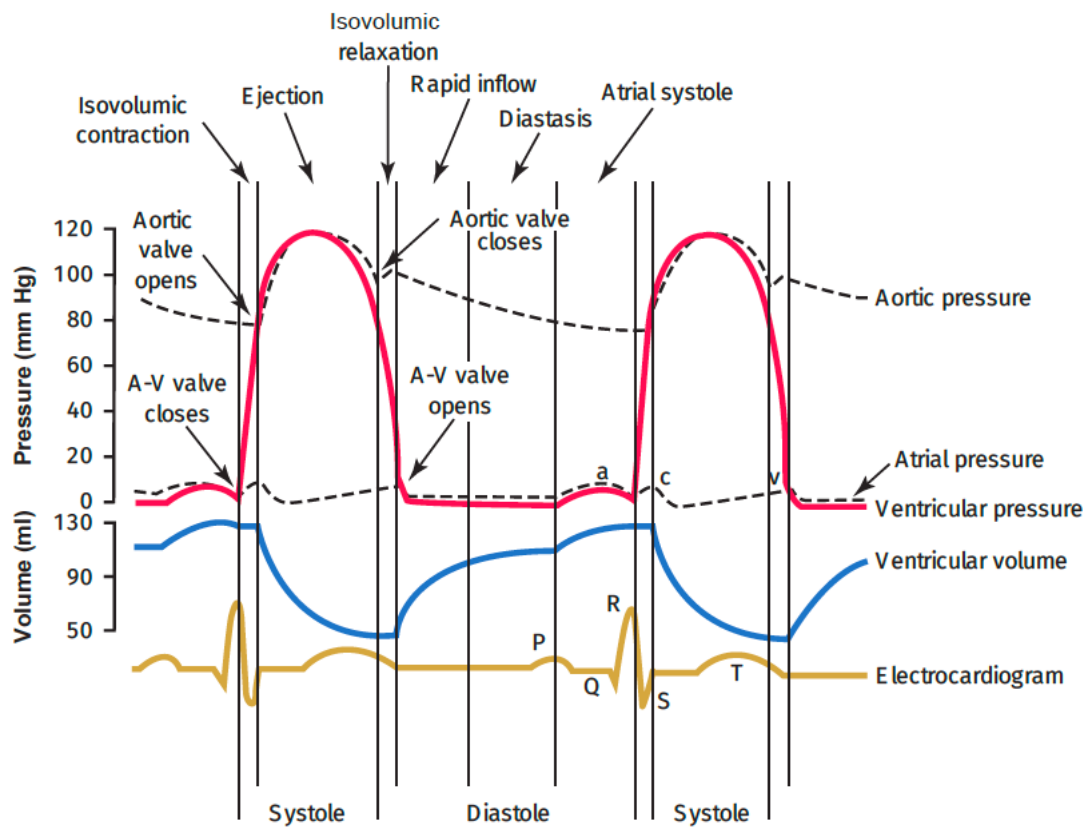


Figure 1.3: Events of the cardiac cycle for the left ventricle (Wiggers diagram) [39].

Although these mechanisms are the same for both the right and the left heart, the latter works at a higher pressure regime than the former since the systemic circulation presents higher resistances than the pulmonary one (peak systolic pressures are about 120 mmHg and 25 mmHg, respectively) [25].

1.2.2. Physiology of gas exchange and diffusion

Systemic and pulmonary circulation

With each beat, the heart pumps blood into two circuits: the pulmonary circulation carrying blood to the air sacs (alveoli) of the lungs and the systemic circulation carrying blood to the rest of the body. These two circuits are arranged in series so that the output of one becomes the input of the other. The right side of the heart is the pump for pulmonary circulation.

The right atrium receives deoxygenated blood from the systemic circulation, and the right ventricle pumps it into the pulmonary trunk. The pulmonary trunk divides into right and left pulmonary arteries that carry blood to the corresponding lung. In each

lung, blood flows through arteries to smaller-diameter pulmonary arterioles and finally into extensive beds of pulmonary capillaries. In the thin-walled pulmonary capillaries, deoxygenated blood unloads CO₂ and picks up O₂. This oxygenated blood flows into pulmonary venules and eventually into more prominent pulmonary veins.

The left side of the heart is the pump for systemic circulation. Oxygenated blood from pulmonary veins enters the left atrium, passes into the left ventricle, and is ejected into the aorta. The aorta branches into progressively smaller systemic arteries that carry the oxygenated blood to all body organs, except for the air sacs (alveoli) of the lungs, which are supplied by the pulmonary circulation, and the arteries give rise to systemic arterioles, which finally lead to systemic capillaries. The exchange of nutrients and gas occurs across the thin capillary walls. Blood unloads O₂ and picks up CO₂. Blood flows from capillaries into systemic venules that carry deoxygenated blood away from tissues and merge to form more prominent systemic veins. Ultimately, the blood flows back to the right atrium through three veins: the superior vena cava, inferior vena cava, and coronary sinus [51].

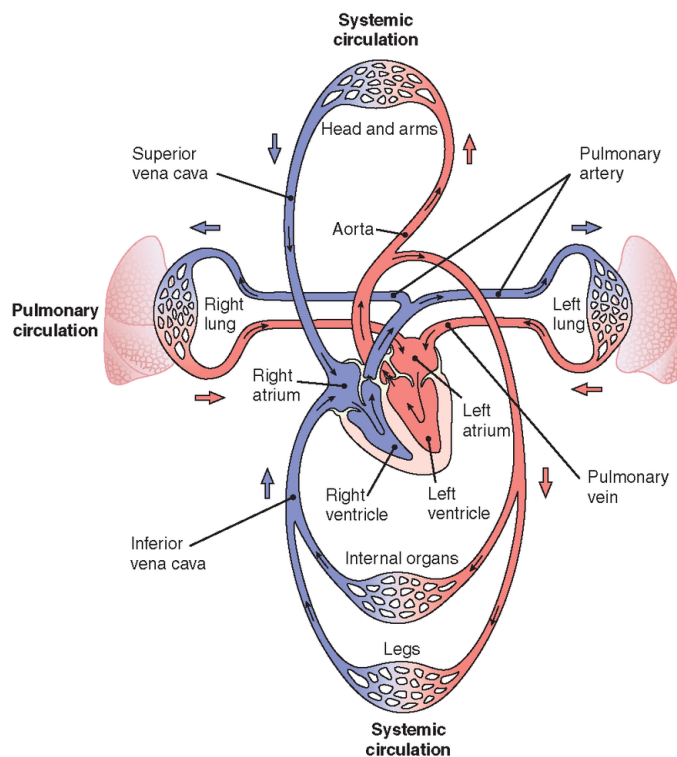


Figure 1.4: Systemic and pulmonary circulation [76].

Gas exchange and diffusion

The exchange of oxygen and carbon dioxide between alveolar air and pulmonary blood occurs via passive diffusion, which is governed by two gas laws:

- Dalton's law, describing how gas moves down their pressure gradients by diffusion;
- Henry's law, explaining how the solubility of a gas relates to its diffusion.

According to Dalton's law, each gas in a mixture of gas exerts its pressure as if no other gas were present. The pressure of a specific gas in a mixture is called its partial pressure and is denoted as P_X (where X denotes the chemical formula of the gas). The mixture's total pressure is calculated by adding all the partial pressures. The partial pressure determines the movement of gas from the area where it is more concentrated to the area where it is less concentrated. For this reason, O_2 and CO_2 diffuse from the atmosphere to the lungs, the lungs to the blood, and the blood to body cells.

Henry's law states that the quantity of a gas that will dissolve in a liquid is proportional to the partial pressure of the gas and its solubility. In body fluids, the ability of a gas to stay in solution is more remarkable when its partial pressure is higher and when it has a high solubility in water. In blood plasma, much more CO_2 is dissolved in comparison to oxygen because the solubility of CO_2 is 24 times greater than that of O_2 [51].

1.2.3. Respiration and gas diffusion in tissues

We define as external respiration the diffusion of O_2 from the air into alveoli to the blood in pulmonary capillaries and the diffusion of CO_2 in the opposite direction. External respiration in the lungs converts deoxygenated blood from the right ventricle into oxygenated blood, returning to the left atrium. As blood flows through the pulmonary capillaries, it picks up O_2 from alveolar air and unloads CO_2 . In a resting person, O_2 diffuses from alveolar air, where its partial pressure is 105 mmHg, into the blood in pulmonary capillaries, where PO_2 is only 40 mmHg. Diffusion continues until the PO_2 of pulmonary capillary blood matches the PO_2 of alveolar air. Nevertheless, blood leaving pulmonary capillaries near alveoli mixes with a small volume of deoxygenated blood; thus, the PO_2 of blood in the pulmonary veins leaving the lungs is about 100 mmHg. The CO_2 , on the contrary, diffuses oppositely from capillary blood to alveolar air. The PCO_2 of deoxygenated blood is 45 mmHg in a resting person, while the PCO_2 of alveolar air is 40 mmHg. Because of this partial pressure, carbon dioxide diffuses from deoxygenated blood into the alveoli until the PCO_2 of the blood decreases to 40 mmHg. Thus, oxygenated blood returning to the left side of the heart has a PCO_2 of 40 mmHg.

The exchange of O₂ and CO₂ between systemic capillaries and tissue cells is called internal respiration, and unlike external respiration, which occurs only in the lungs, it occurs in tissues throughout the body. As O₂ leaves the bloodstream, oxygenated blood is converted into deoxygenated blood. The PO₂ of blood pumped into systemic capillaries is higher than the PO₂ in tissue cells (100 mmHg versus about 40 mmHg at rest) because the cells constantly use O₂ to produce ATP. Due to this pressure difference, oxygen diffuses from the capillaries into tissue cells, and blood PO₂ drops to 40 mmHg. At the same time, CO₂ diffuses in the opposite direction. Tissue cells constantly produce CO₂, thus the PCO₂ of cells (45 mmHg at rest) is higher than that of systemic capillary blood (40 mmHg). As a result, CO₂ diffuses from tissue cells into systemic capillaries until the PCO₂ in the blood increases to 45 mmHg.

At rest, tissue cells need about 25% of the available O₂ in oxygenated blood, and despite its name, deoxygenated blood retains 75% of its O₂ content. During exercise, more O₂ diffuses from the blood into metabolically active cells, which use more O₂ for ATP production, causing the O₂ content of deoxygenated blood to drop below 75%.

The rate of pulmonary and systemic gas exchange depends on several factors.

- *Partial pressure difference of the gas.* The diffusion rate is faster when the difference between PO₂ in alveolar air and pulmonary capillary blood is more significant. During exercise, the differences between PO₂ and PCO₂ in alveolar air versus pulmonary blood increase. The partial pressures of O₂ and CO₂ in alveolar air also depend on the airflow rate into and out of the lungs. Pathological conditions which slow ventilation, decrease the amount of O₂ and CO₂ that can be exchanged between alveolar air and blood.
- *Surface area available for gas exchange.* The surface area of the alveoli is vast (about 70 m²), and many capillaries surround each alveolus, so many that as much as 900 mL of blood can participate in gas exchange at any instant. Any pulmonary disorder that decreases the functional surface area of the respiratory membranes decreases the rate of external respiration.
- *Molecular weight and solubility of the gas.* O₂ has a lower molecular weight than CO₂, so it could be expected to diffuse across the respiratory membrane about 1.2 times faster. However, the CO₂ solubility in the fluid portions of the respiratory membrane is about 24 times greater than that of O₂. For these reasons, net outward CO₂ diffusion occurs 20 times more rapidly than net inward O₂ diffusion. Consequently, when diffusion is slower than usual, O₂ insufficiency (hypoxia) typically occurs before significant CO₂ retention (hypercapnia).

- *Diffusion distance.* The respiratory membrane is thin, and diffusion occurs quickly. Furthermore, the capillaries are so narrow that the red blood cells must pass through them in a single file, which minimizes the diffusion distance from alveolar airspace to haemoglobin inside red blood cells. The build-up of interstitial fluid between alveoli, as occurs in pulmonary edema, slows the rate of gas exchange because it increases diffusion distance.

Oxygen transport

Oxygen does not dissolve easily in water, so only about 1.5% of O₂ in the blood is dissolved into the blood plasma. About 98.5% of blood O₂ is bound to hemoglobin in red blood cells (RBC) [51]. Hemoglobin is an iron-containing protein of the red blood cells (erythrocytes). It has a tetrahedral structure of four heme groups surrounding a globin group. Globin consists of two linked pairs of polypeptide chains. Heme is composed of a ringlike organic compound, a porphyrin, to which an iron atom is attached. The iron atom binds oxygen as the blood travels between the lungs and the tissues. Each hemoglobin molecule has four iron atoms, which accordingly can bind four oxygen molecules. [16]. Oxygen binds to hemoglobin (deoxyhemoglobin) to form oxyhemoglobin (Hb–O₂). The 98.5% of the O₂ bound to hemoglobin is trapped inside RBC, so only the dissolved O₂ (1.5%) can diffuse out of tissue capillaries into tissue cells.

Oxygen and hemoglobin

The multiple factors that influence oxygen binding to and dissociation from hemoglobin are the following.

- *Oxygen partial pressure.* The most critical factor that determines how much O₂ binds to hemoglobin is the PO₂: the higher the PO₂, the more O₂ combines with Hb. When deoxyhemoglobin (Hb) is completely converted to oxyhemoglobin (Hb–O₂), the hemoglobin is said to be fully saturated: every available iron atom has combined with a molecule of O₂. In the other cases, when iron atoms are still available, hemoglobin is only partially saturated. The percent saturation of hemoglobin expresses the average saturation of hemoglobin with oxygen. For instance, if each hemoglobin molecule has bound two O₂ molecules, then the hemoglobin is 50%. The oxygen-hemoglobin dissociation curve illustrates the relationship between the percent saturation of hemoglobin and PO₂.

When the PO₂ is high, hemoglobin binds with large amounts of O₂ and is almost 100% saturated. When PO₂ is low, hemoglobin is only partially saturated. Therefore, in pulmonary capillaries, where PO₂ is high, much of O₂ binds to hemoglobin. In tissue capillaries, where the PO₂ is low, hemoglobin does not hold as much O₂, and the dissolved O₂ is unloaded via diffusion into tissue cells. Note that hemoglobin is still 75% saturated with O₂ at a PO₂ of 40 mmHg, the average PO₂ of tissue cells in a person at rest. Only 25% of the available O₂ unloads from hemoglobin and is used by tissue cells under resting conditions.

When the PO₂ is between 60 mmHg and 100 mmHg, hemoglobin is 90% or more saturated with O₂. Thus, the blood picks up a nearly full load of O₂ from the lungs even when the PO₂ of alveolar air is as low as 60 mmHg; as a consequence, people can still perform well even though PO₂ may drop as low as 60 mmHg (e.g., at high altitudes or when they have certain cardiac and pulmonary diseases). Note also in the curve that at a considerably lower PO₂ of 40 mmHg, hemoglobin is still 75% saturated. However, oxygen saturation of Hb drops to 35% at 20 mmHg. Between 40 mmHg and 20 mmHg, large amounts of O₂ are released from hemoglobin in response to only small decreases in PO₂. In active tissues, such as contracting muscles, PO₂ may drop well below 40 mmHg. Then, a large percentage of the O₂ is released from hemoglobin, providing more O₂ to metabolically active tissues.

- *Acidity.* Metabolically active tissue cells need O₂ and produce acids (CO₂) and heat as wastes. As acidity increases (pH decreases), the affinity of hemoglobin for O₂ decreases, and O₂ dissociates more readily from hemoglobin. Increasing acidity enhances the unloading of oxygen from hemoglobin. During exercise, metabolically active tissues release lactic acid and carbonic acid, which promotes O₂ release from hemoglobin.
- *Carbon dioxide partial pressure.* As PCO₂ rises, hemoglobin releases O₂ more readily. PCO₂ and pH are related factors because low blood pH (acidity) results from high PCO₂. As CO₂ enters the blood, much of it is temporarily converted to carbonic acid (H₂CO₃). This reaction is catalyzed by an enzyme in red blood cells called carbonic anhydrase, and it reads



The carbonic acid, thus formed in red blood cells, dissociates into hydrogen and bicarbonate ions. As the H^+ concentration increases, pH decreases. Thus, an increased PCO_2 produces a more acidic environment, which helps to release O_2 from hemoglobin. During exercise, the lactic acid produced by anaerobic metabolism also decreases blood pH. Thus, hemoglobin releases more O_2 as blood flows through active tissues producing more CO_2 .

- *Temperature.* As temperature increases, so does the amount of O_2 , which is released from hemoglobin. Active tissues produce more heat, which elevates the local temperature and promotes the release of O_2 from oxyhemoglobin. Fever produces a similar result. In contrast, cellular metabolism slows during hypothermia (lowered body temperature), the need for O_2 is reduced, and more O_2 remains bound to hemoglobin.

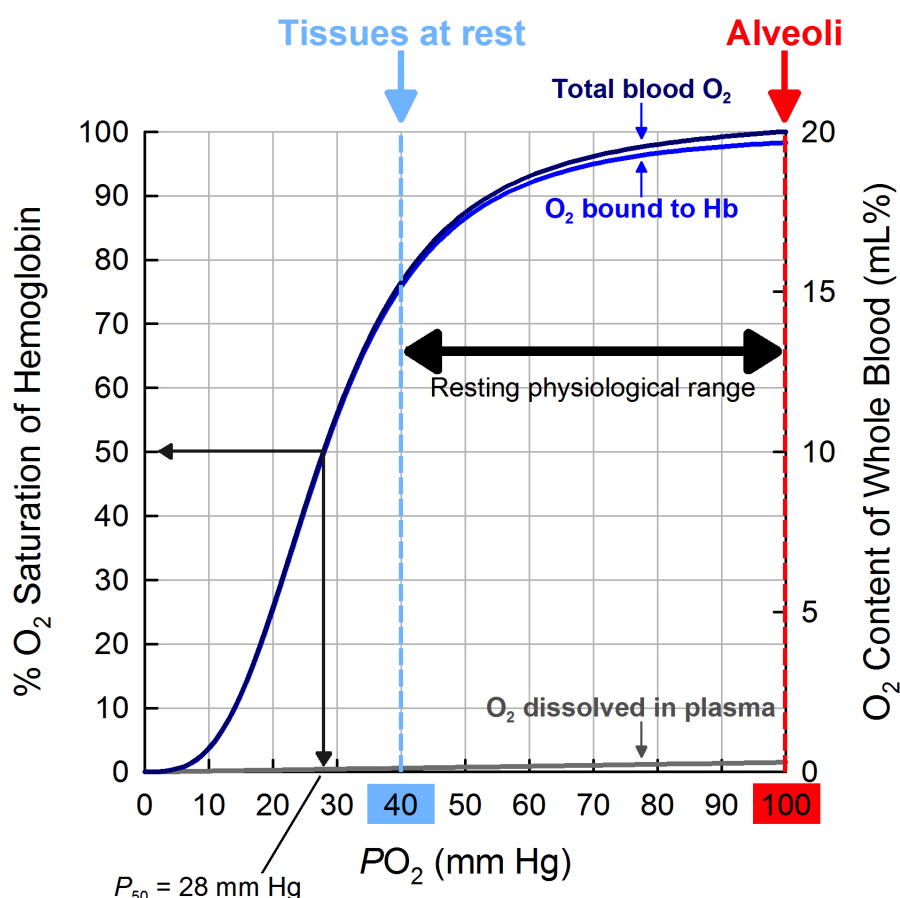


Figure 1.5: Oxyhemoglobin dissociation curve [83].

Carbon dioxide transport

Carbon dioxide is transported in the blood in three main forms.

- *Dissolved carbon dioxide.* The smallest percentage (about 7%) is dissolved in blood plasma and, when it reaches the lungs, rapidly diffuses into the alveolar air.
- *Bound to amino acids.* About 23% of CO₂ is bound to amino acids and blood proteins. Since hemoglobin is the most prevalent protein in blood cells, CO₂ is mainly bound to hemoglobin. The CO₂ binding sites are the amino acids of the globin portions. Hemoglobin bound CO₂ is called carbaminohemoglobin: in tissue capillaries, PCO₂ is high, promoting carbaminohemoglobin formation. On the contrary, in pulmonary capillaries, PCO₂ is low, and CO₂ rapidly splits apart from globin protein and diffuses in the alveoli.
- *Bicarbonate ions.* The most significant percentage of CO₂ (about 70%) is transported in blood plasma as bicarbonate ions (HCO₃⁻). As CO₂ diffuses in capillaries, it enters RBC and reacts with water, in the presence of carbonic anhydrase, forming carbonic acid, which dissociates in bicarbonate ions (HCO₃⁻) and hydrogen ions (H⁺). Thus, as blood picks up CO₂, HCO₃⁻ accumulates inside RBC, and some HCO₃⁻ moves out into the blood plasma, down its concentration gradient. The net effect of these reactions is that CO₂ is removed from tissue cells and transported in blood plasma as HCO₃⁻. As blood passes through pulmonary capillaries in the lungs, all these reactions reverse, and CO₂ is exhaled [51].

1.2.4. Physiology of myocardial perfusion and oxygenation

Myocardial perfusion

The cardiac muscle requires continuous oxygen and nutrients supply to maintain proper functionality. In the rest condition, the heart receives about 5% of the cardiac output, although it represents less than 0.5% of total body weight.

The cardiac output is the volume of blood ejected by a ventricle per minute, and it can be computed as the stroke volume (blood volume ejected by the ventricle during each contraction) multiplied by the heart rate (HR). In a typical resting adult, stroke volume averages 70 mL beat⁻¹, and HR is about 75 beat min⁻¹. Thus, the average cardiac output in a resting adult is 5250 mL min⁻¹ (5.25 L min⁻¹). When body tissues use more or less oxygen, cardiac output changes to meet the need. Factors that increase stroke volume or make the heart beat faster, such as exercise, increase cardiac output. Conversely, factors that decrease stroke volume or HR decrease cardiac output [51].

Coronary blood flow

The morphology of the coronary arterial tree has a well-defined outside-in structure [34]: large arteries ($\sim 1 \div 5$ mm of diameter), which lay on the epicardium, and are defined as epicardial arteries [62]; arteriole ($\sim 100 \div 300$ μm of diameter); capillaries ($\sim 5 \div 10$ μm of diameter), which penetrate into the muscular tissue, and are defined as intramural vessels [62],

Experimental evidence from high-resolution cryomicrotome imaging suggested that distinct coronary arteries supply different myocardial territories [18, 50, 108, 110]. Moreover, microscope analysis showed capillary end loops in the border zone of such regions [78]. These territories are defined as perfusion regions [19, 59, 79, 82], and their mass is called fractional myocardial mass [54, 122]. Besides, the coronary circulation can also be provided with anastomotic channels, defined as collateral vessels, which connect different perfusion regions and are recruited only in case of need.

For a standardized visualization of the regional myocardial perfusion, the American Heart Association (AHA) recommends a 17-segment model of the left ventricle [19]. The left ventricle is divided into four parts perpendicular to the long axis of the heart: the basal, the mid, the apical, and the apex (i.e., the extreme tip of the ventricle where there is no more extended cavity present). Then the mid and basal are divided into six 60° segments, whereas the apical is divided into four segments of 90° each because of myocardial tapering, as in Figure 1.6.

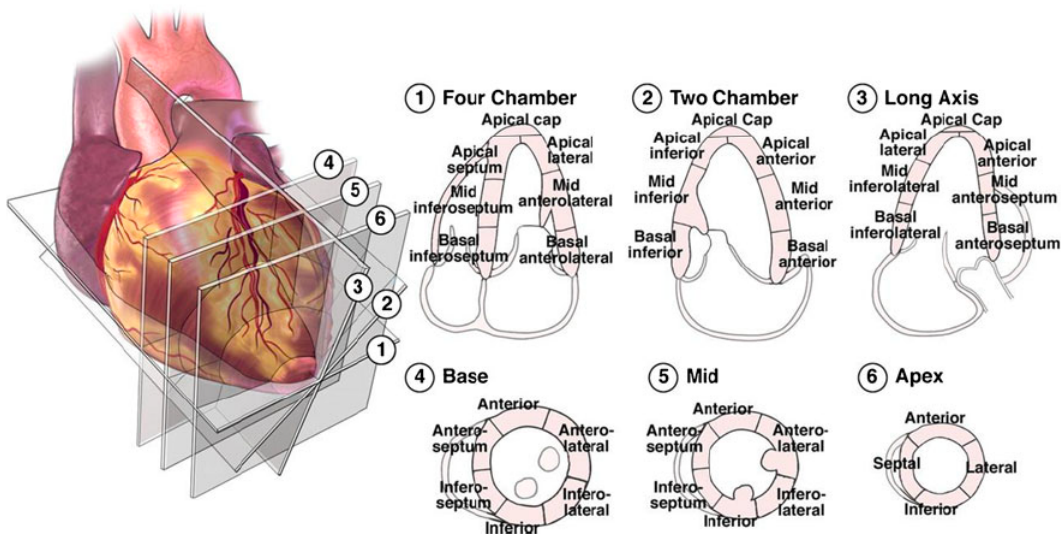
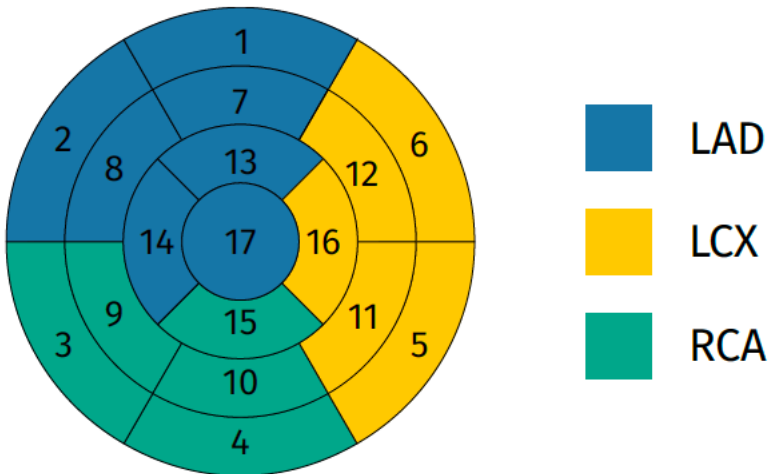


Figure 1.6: Segmental analysis of left ventricle based on schematic view [25].

The functional values measured inside the 17 segments can be arranged as a polar plot as in Figure 1.7). Although there is a great variability in the coronary artery blood supply (especially in the apex), for the analysis of myocardial perfusion, the AHA assigned each of the 17 segments to one of the three major coronary artery: segments 1, 2, 7, 8, 13, 14 and 17 (blue in Figure 1.7) are assigned to LAD; segments 3, 4, 9, 10 and 15 (green in Figure 1.7) to RCA; and segments 5, 6, 11, 12 and 16 (yellow in Figure 1.7) to LCX [19].



- | | | |
|------------------------|-----------------------|---------------------|
| 1. basal anterior | 7. mid anterior | 13. apical anterior |
| 2. basal anteroseptal | 8. mid anteroseptal | 14. apical septal |
| 3. basal inferoseptal | 9. mid inferoseptal | 15. apical inferior |
| 4. basal inferior | 10. mid inferior | 16. apical lateral |
| 5. basal inferolateral | 11. mid inferolateral | |
| 6. basal anterolateral | 12. mid anterolateral | 17. apex |

Figure 1.7: Polar plot of perfusion regions [25].

The coronary blood flow (CBF) is influenced by the interaction between the cardiac muscle and the coronary vessels. In early systole, isovolumic contraction of the left ventricle causes the compression of the intramural vessels; therefore, CBF in LCA is almost null or even reversed. Then, during the ejection phase, CBF in LCA increases, reaching the peak only at the early diastole, when the left ventricle relaxation reduces the compression of the intramural vessels. The 80% of the total left CBF occurs during diastole.

Concerning the right heart, since it works with lower pressures, the compression on RCA downstream vessels is less effective, and the systole only partially influences CBF in RCA.

The blood flow in coronary veins has the opposite trend of the arterial CBF: the contraction of the ventricles moves venous blood from endocardial layers to epicardial ones [120].

Coronary blood flow regulation

The cardiac muscle works almost exclusively aerobically. It exhibits the highest per gram oxygen consumption ($\sim 50 \div 100 \text{ } \mu\text{L min}^{-1} \text{ g}^{-1}$) and the highest extraction of delivered oxygen among all the organs ($\sim 70 \div 80\%$ vs $\sim 30 \div 40\%$) [8, 14, 34]. For these reasons, when the metabolic demand rises (e.g., during exercise), the myocardium cannot extract much more oxygen, and it needs to increase the amount of CBF reaching the tissue.

Thus, to maintain a proper heart function, the resistance of the coronary circulation is continuously regulated to respond to the energetic needs of the heart with an adequate myocardial perfusion [14, 34]. Two mechanisms are responsible for maintaining the balance between the myocardial demand and CBF: autoregulation, which guarantees a constant CBF independent of changes in perfusion pressure, and metabolic adaptation, which adapts the CBF to meet the energetic myocardial requirements. Both work through vasodilation and vasoconstriction of the coronary arteries, thus modifying the resistances of the vessels [43].

Vasodilation is the only way to adjust CBF during exercise or under stress conditions, and several local regulatory mechanisms can induce it [43, 85, 120].

- *Myogenic control.* Smooth muscle cells contract and change the vessel diameter to keep constant the stress in the circumferential direction of the vessel wall (determined by the transmural blood pressure).
- *Metabolic control.* The cardiac muscle releases metabolic mediators, such as adenosine and carbon dioxide.
- *Endothelium-based control.* The endothelial cells of the vessels induce the release of nitric oxide to increase the vessels' diameter and keep constant the shear stress acting on the vessel walls.

The CBF can also be affected by a nervous regulation: vasoconstrictor sympathetic fibers innervate the entire heart and the coronary circulation. During exercise, such nervous fibers are activated, and the metabolic vasodilation is enhanced by the increase of the HR and the contraction force to inhibit the vasoconstrictor effect on the vessels [8, 14].

Myocardial oxygen delivery

The amount of O_2 delivered from the coronaries can be computed as the product between CBF and the oxygen concentration of arterial blood. Since the former is about 80 mL min^{-1} per 100 g of tissue and the latter is about 20 mL of O_2 per 100 mL of blood,

we get that the amount of O_2 delivered from the coronaries is about 16 mL of O_2 per min per 100 g of tissue.

Conditions that alter the concentration of RBC will alter the oxygen concentration and the oxygen supply to tissues. Furthermore, the amount of hemoglobin within the RBC also determines the amount of oxygen the blood carries. For example, anemia, which can result from either a reduced concentration of RBC or a reduced hemoglobin concentration within RBC, decreases oxygen delivery to tissues. Ordinarily, the oxygen content of arterial blood changes relatively little. Therefore, the primary determinant of oxygen delivery in the absence of hypoxemia (reduced O_2 concentration) is the CBF.

In coronary artery disease, several factors can reduce CBF. Stenotic lesions cause a narrowing of vessels, particularly the large epicardial coronaries (e.g., left anterior descending or circumflex arteries). The stenosis may be at a specific site or diffuse along the vessel's length. In either case, the stenosis can limit maximal coronary flow. Furthermore, diseased coronary vessels are more susceptible to vasospasm, which can temporarily restrict coronary flow at rest: this fact can occur during stressful conditions or exercise in susceptible individuals. Finally, thrombus formation, particularly at the site of a ruptured atherosclerotic plaque, can partially or entirely occlude a coronary vessel causing unstable angina or myocardial infarction [56].

1.3. State of the art of mathematical models

Numerical simulations can be a valuable tool for obtaining quantitative information about biomedical processes in physiological and pathological conditions. To this end, in last decades several authors have developed different mathematical and numerical models to understand these phenomena better [25, 62, 63, 109].

In this section, we briefly review the modeling approaches for CBF, myocardial perfusion, and, in particular, oxygen transport and exchange. In particular, we find mathematical models for

- blood dynamics in epicardial coronary arteries in Section 1.3.1;
- blood dynamics in intramural coronary vessels in Section 1.3.2;
- oxygen exchange in microvasculature in Section 1.3.3.

We mainly focus on the work of Goldman [32] for the latter and the work of Di Gregorio et al. [25] for the others.

1.3.1. Models for blood dynamics in epicardial coronary arteries

Since the length scales of the coronary arterial network are very different, we can find in the literature several modeling approaches. In particular, a geometric multiscale strategy approach can combine two or more models to account for the scale separation in the coronary arterial network and to obtain a detailed and comprehensive representation of the overall myocardial perfusion processes.

Poiseuille's law

Poiseuille's law is a physical law describing the fluid dynamics inside rigid cylindrical conduits. It is derived by the 3D Navier-Stokes equations in cylindrical coordinates, making several assumptions on the flow and pressure drop [2]. Poiseuille's law is a simple model for blood flow inside the coronary vascular network, but it presents some limitations in representing the CBF, i. e., it can not describe the CBF's time-dependent evolution.

Lumped parameter models

Lumped parameter models assume that a given distributed property of a physical system can be concentrated in a single element that appropriately approximates its features. These models simplify the complexity of infinite-dimensional problems to a zero-dimensional one, passing from PDEs to ODEs. Moreover, in blood dynamics, the unknowns depends only on time, and their values are the average-in-space of the corresponding physical distributed variable [92]. Thus, lumped parameter models reduce computational complexity, but they are not suitable for describing the flow rate and pressure wave distribution through the vascular system or the spatial distribution of the CBF inside the myocardium.

Lumped parameter models are generally used to describe the entire coronary arterial tree [67, 123] or single vessel tracts, coupled to model the entire vessel network [27, 84]. In the former case, the lumped parameter models are used mainly as boundary conditions. In contrast, in the latter case, a distinct lumped parameter model is used to represent a segment of the vascular network, and it can be used to consider either only the main epicardial branches [27, 84] or even each segment of the coronary arterial tree [49, 75].

The waterfall model proposed by Downey et al. [26] was explicitly developed for the coronary vessels. Its name refers to the analogy between coronary arteries and waterfalls: the flow over a fall is determined by the elevation between the highest upstream point (arterial pressure) and the origin of the fall (tissue pressure), and it is not affected by

the overall height of the waterfall (arteriovenous pressure difference) [34]. However, this surrogate model can not model reverse arterial flow or the increase of venous outflow during systole. Thus, the waterfall model can reproduce the measured arterial inflow, but it can not provide a comprehensive description of CBF [6, 7, 15, 62, 120].

To overcome the waterfall model's limitation, Spaan et al. [107] proposed the intramyocardial pump model, which assumes an analogy between the pumping actions of the ventricle and the cardiac muscle. This model can reproduce both the storage of an intravascular blood volume during diastole and the pumping of such a volume towards the venous system and back into arterial vessels during systole [31, 34, 120, 124].

In order to account for the vessel walls' large deformations and the nonlinear behavior, the intramyocardial pump model was extended in [49] using a nonlinear three-element Windkessel model for the representation of each single vessel segment. The same approach was also used by Algranati et al. [3] showing that the myocardial-vessel interaction is caused by a combination of cavity-induced extracellular pressure and shortening-induced intramyocyte pressure.

1D blood dynamics

One-dimensional blood flow models are the most used approach for modeling blood dynamics inside coronary arterial networks composed of many vessels [71, 72, 106, 116], thanks to the advantage over the lumped parameter models of including wave propagation analysis in a spatially distributed vascular network while reducing the computational costs with respect to a whole 3D approach. The 1D equations of mass and momentum conservation are usually derived from an averaging of the 3D formulation of Navier-Stokes equations in a compliant domain over the cross-sections of the vessels under specific assumptions [81, 89].

The reduction from the 3D problem leads to a system of two PDEs with three unknowns: the area, the flow rate, and the mean pressure over a cross-section of the vessel. In order to close the system, a third equation is required: it is usually a pressure-area relation derived by a membrane law.

One of the first applications of 1D models of the coronary network was provided by Smith et al. [106] to study the spatial and temporal behaviour of CBF.

Despite being computationally cheaper than the 3D fluid dynamics model, 1D approaches are limited because they do not allow the regional wall shear stress computation, and they can simulate the viscous losses due to stenosis only by using empirical models [105].

3D blood dynamics

Three-dimensional fluid dynamics models are based on the 3D Navier-Stokes formulation, allowing a deeper analysis of flow patterns involved in the pathophysiology of coronary circulation, although they are more computationally expensive than the previous simplified models. This main drawback makes 3D models of coronary blood dynamics not usually applied to the entire coronary arterial tree but only to the main epicardial coronary arteries with few bifurcating vessels or too small tracts of the epicardial branches. Hence, 3D models applied to the CBF context mainly aim to study the phenomena involved with the coronary blood dynamics rather than the perfusion process itself.

1.3.2. Models for blood dynamics in intramural coronary vessels

An explicit description of the intramural vasculature with one of the previous detailed models would be unfeasible for the high computational cost and complexity of defining proper boundary conditions for every single vessel. Moreover, clinical in-vivo images do not allow the visualization and reconstruction of intramural coronary vessels. For these reasons, porous media approaches have been proposed as an alternative strategy to describe the flow patterns in space and time characterizing the intramural vascular network.

The intramural vascular network inside the myocardium is described as a set of interconnected pores (filled with blood) inside a solid material (i.e., the cardiac tissue) using a homogenization procedure. The porous medium comprises two phases, the solid matrix and the fluid phase, which occupy a fraction of the total volume. The fraction of fluid volume over the total volume represents the porosity of the medium.

In cardiac perfusion modeling, the most common porous media flow model is Darcy law, which was also used in a multi-compartment formulation to account for the different length scales of the intramural vascular network, or it was also complemented with a poroelastic formulation to model the fluid-structure interaction between the fluid in the vessels, and myocardium contraction [10].

Multi-compartment formulation

The intramural vascular network is composed of vascular structures with different length scales, properties, and functions (e.g., small arteries, arterioles, and capillaries). A global homogenization of the intramural vessels could lead to average quantities, e.g., flow rate and pressure, which are not representative of each specific vascular level. For this rea-

son, Huyghe et al. [44, 46] proposed a "hierarchical" subdivision of the vessels to define different vascular compartments that correspond to different length scales of the intramural vessels. Each vascular compartment is modeled employing a porous medium, which co-exists with the other compartments in the same domain. The porous compartments are characterized by their physical properties, such as porosity and permeability, substituting the effect of the corresponding intramural vessels, and are coupled through inter-compartment flows, which depend on the inter-compartment pressure gradients. The multi-compartment porous approach allows the local and regional quantification of myocardial perfusion and considers the different hierachic vessel characteristics [47].

Michler et al. [68] analyzed the multi-compartment Darcy model from a computational standpoint, carrying on a comparison between the mixed and the primal formulation of the problem. They proved that the latter would be more suitable for clinical application due to the resulting substantial computational and memory saving with respect to the former. The multi-compartment approach was also applied by Cookson et al. [21] together with a poroelastic framework.

The multi-compartment Darcy model requires proper physical continuum model parameters to obtain accurate perfusion results and a suitable homogenization from an explicit vascular network to the corresponding porous medium.

Vankan et al. [115] proposed the first analysis of the parametrization of the model, comparing the solution of the multi-compartment Darcy model with the solution computed with the application of the Poiseuille's law to the explicit vascular network.

Recently, Hyde et al. [47] analyzed the parametrization of the multi-compartment Darcy model applied to a porcine intramural coronary network.

Poromechanics

Poromechanics modeling approaches account for the interaction between myocardial contraction and coronary vessels (i.e., pores in the porous media) [21, 45, 61, 119]. Poromechanics approaches originate from Biot's consolidation model [13], and in the last years, they have been applied to model myocardial deformation and its effect on perfusion. Huyghe et al. [45] proposed a porous media model on a left pulsatile ventricle. The cardiac tissue was modeled as incompressible, anisotropic, and viscoelastic material, and the contraction of muscular fibers also influenced the blood flow in the pores. Chapelle and co-workers [17, 20] developed a thermodynamically consistent poroelastic model for incompressible media, which is valid for finite strains. They coupled their model with an active contraction of the left ventricle and considered the fiber orientation and a dis-

tributed volumetric coronary inflow. The model captured physiological phenomena of the interaction between the myocardium and coronary vessels, such as the systolic flow impediment. However, it was applied only to an idealized left ventricle geometry, not accounting for a coronary artery network. Moreover, their model is very challenging from a mathematical point of view because of its nonlinearity. Thus, a linearized formulation of the model was proposed by [17] and also analyzed in [9].

Transport of contrast agent

In the last few years, another modeling approach was developed to represent the transport of a contrast agent inside the myocardium during perfusion imaging acquisition. This approach aims to provide indirect insight into perfusion by employing quantitative information about contrast agent transport. For instance, it could be possible to detect perfusion defects by identifying the perfusion regions where limited transport of contrast agent occurs.

Cookson et al. [22] used a single-compartment porous medium model coupled with advection-reaction-diffusion equations to model the contrast agent transport between the intravascular (blood) and the extravascular spaces. The authors conducted a parameter space study to analyze healthy and diseased myocardial tissue in a two-dimensional rectangular domain. In one following study, the same research group used the transport model in a multi-compartment framework, and they applied it to a porcine left ventricle to detect a perfusion defect related to the lack of contrast agent transport in specific regions [77].

Geometric multiscale models

Multiscale models seem attractive and suitable for a comprehensive mathematical description of myocardial perfusion. Indeed, they allow capturing heterogeneous length scales phenomena by coupling different dimensional models, adequately chosen for each of the considered length scales, keeping low computational costs. However, despite the great potential, multiscale models are complex from a mathematical standpoint because they require proper assumptions for the coupling of the models, adequate coupling conditions, and a proper well-posedness analysis [92]. They are also very challenging from a computational point of view, requiring, for instance, proper numerical solution strategies. In the myocardial perfusion modeling, the coupling between vessels of different length scales was performed using, for example:

- 1D blood dynamics for large coronary arteries and 3D porous medium model for the intramural vessels [21, 47, 61];
- 1D blood dynamics for large coronary arteries and 0D approach for the intramural vessels [73, 106, 114];
- 3D blood dynamics for epicardial coronary arteries and 0D approach for the intramural vessels [53, 70, 102].

Lee et al. [61] aimed their work at the analysis of the myocardial perfusion and the non-invasive quantification of the wave intensity analysis, which helps predict heart recovery after myocardial infarction and the detection of perfusion defects. The authors proposed a multiscale computational model consisting of a 1D coronary flow model from Smith et al. [106] and a poroelastic model for deep intramural vessels from Cookson et al. [21].

1.3.3. Models for oxygen exchange in microvasculature

Theoretical modeling has been pursued for years to understand the microvascular O₂ transport better. However, several complexities make microvascular O₂ transport challenging to study, particularly when quantitative results are desired. The microvasculature has a very complicated 3D spatial structure and a small scale: its structural complexity leads to heterogeneity in microvascular perfusion, and unique hemodynamic effects not seen in larger vessels occur since many vessel sizes are on the order of the RBC size. RBC perfusion heterogeneity, in turn, leads to heterogeneities in O₂ supply, tissue oxygenation, and O₂ consumption. These heterogeneities can have significant physiological consequences but are challenging to characterize experimentally: then, theoretical modeling can be used to study their effects.

Leveraging on the work of Goldman [32], to which we refer to all the details, this section gives an overview of the most known oxygenation models. We start with a brief discussion of the intraerythrocyte, and intravascular O₂ transport [41, 87], including factors that determine intravascular resistance to blood-tissue O₂ transport. Then, we present the original Krogh model [58] of O₂ delivery by a single capillary. Its central assumptions are discussed first in the context of single-vessel models (in both time-dependent and multi-species cases) and then in models that use multi-vessel arrays or networks and require sophisticated analytical or numerical analytical solution techniques.

Intravascular transport models

Since most O₂ is carried in the blood bound to Hb inside RBC, realistic microvascular O₂ transport modeling requires a Hb–O₂ binding model. This binding occurs in four steps since the Hb molecule has four O₂ binding sites (heme groups) that work cooperatively. Four experimental constants fully describe the equilibrium binding. It is given by the Adair equation, which can not be inverted analytically, so the easily invertible Hill equation has been used in most theoretical models to describe fractional Hb–O₂ saturation [87]. Although the Hill equation is only highly accurate in the SO₂ range of 20 ÷ 80%, this is enough for most O₂ transport models, given the other approximations used. Notice that the exact form of the dissociation curve varies with blood pH, CO₂ concentration, 2,3-diphosphoglycerate concentration, and temperature, as described in [23].

In addition to describing Hb–O₂ binding and blood O₂ concentration, to model O₂ transport from capillary blood to tissue, it is necessary to consider the properties of O₂ transport inside capillaries. Many models, including Krogh-Erlang that have focused on O₂ transport in the tissue surrounding capillaries, have failed to account for intracapillary O₂ gradients, which lead to effective resistance to blood-tissue O₂ transport [41]. In order to quantify intravascular capillary resistance (IVR), theoretical studies have been performed to determine the magnitude of this resistance and how it depends on various parameters such as capillary diameter and RBC velocity [32].

Since arterioles are also involved in blood-tissue diffusive O₂ transport, it is essential to understand how they carry O₂ and release (or take up) O₂ to the surrounding tissue before including them in models of tissue O₂ delivery. As pointed out by Hellums et al. [41], two distinct size regimes of non-capillary microvessels must be considered. In larger microvessels (20 ÷ 100 μm diameter), intravascular O₂ transport can be modeled using a continuum RBC distribution in the vessel core surrounded by a plasma layer. However, in smaller microvessels (8 ÷ 15 μm), it is believed that the actual distribution of RBC in the lumen needs to be considered to predict O₂ transport properties accurately. No theoretical work has yet been done on this latter case due to the geometric and computational complexities involved, and therefore only extrapolations from results for smaller and larger vessels are available.

For 20 ÷ 100 μm vessels, Nair et al. [74] developed a theoretical model of intravascular O₂ transport, and they validated it against some experimental data. They use the FEM to calculate steady-state O₂ transport in the RBC-rich core and plasma sleeve regions, which were coupled by assuming continuity of PO₂. This model included Hb–O₂ kinetics and transport between the RBC and plasma in the core. The results of the model agreed well

with O_2 saturation measurements in a 27 μm artificial capillary and are used to calculate MTCs for diameters in the range 15 \div 100 μm . While MTCs generally depend only weakly on SO_2 in capillaries, they increase approximately linearly with SO_2 in arterioles, and the slope of this relationship increases with increasing vessel diameter.

Page et al. [80] extended the model [74] to the case in which a Hb solution is present in plasma, and they included a new treatment of shear augmentation, which was more critical than for the case without plasma Hb, in particular for O_2 uptake. This model agreed well with experimental data on O_2 release and uptake in an artificial capillary of 25 μm . Another interesting result was that blood containing RBC and 30% Hb solution had the same O_2 transport capability as a Hb solution without RBC, having the same total Hb content.

Single-vessel Krogh model

A natural way to study blood-tissue O_2 transport is to consider a single blood vessel and its release of O_2 into the surrounding tissue. Krogh [58] proposed to represent the O_2 transport in an entire microvascular bed by a single capillary that supplies O_2 to the surrounding cylinder of tissue, inspired by the structure of the skeletal muscle, with its parallel muscle fibers and capillaries. This axisymmetric (tissue cylinder) geometry, with several additional assumptions, is known as the Krogh model, and Krogh obtained its prediction for tissue PO_2 with the assistance of the mathematician Erlang; hence the result is known as the Krogh-Erlang solution.

The additional assumptions of this model, some of which were not explicit at the time it was proposed, are the following.

1. Tissue O_2 consumption is constant and uniform.
2. Tissue PO_2 at the capillary wall equals average capillary PO_2 (no IVR).
3. Tissue O_2 solubility and diffusivity are uniform.
4. Axial (or longitudinal) diffusion of O_2 is not significant.
5. All important microvascular O_2 transport phenomena are steady-state.
6. All capillaries are parallel, unbranched, and equally spaced.
7. All capillaries receive equal convective O_2 supply.
8. Capillaries are the only microvessels that play a role in O_2 transport to tissue.

Let r be the radial coordinate, $P(r)$ be the steady-state PO_2 in the tissue cylinder and P_{cap} be the given capillary PO_2 , then the above assumptions lead to the following reaction-diffusion problem for $P(r)$:

$$\left\{ \begin{array}{l} D\alpha \frac{1}{r} \frac{\partial}{\partial r} \left(r \frac{\partial P(r)}{\partial r} \right) = M_0, \\ P = P_{\text{cap}} \text{ at } r = R_{\text{cap}}, \\ \frac{\partial P(r)}{\partial r} = 0 \text{ at } r = R_t, \end{array} \right. \quad (1.1a)$$

$$(1.1b)$$

$$(1.1c)$$

where D is the tissue O_2 diffusivity, α is the tissue O_2 solubility, M_0 is the tissue O_2 consumption rate, R_{cap} is the capillary radius, and R_t is the tissue radius. The Krogh diffusion coefficient is defined as $K = D\alpha$.

The solution to the above equation is

$$P(r) = P_{\text{cap}} + \frac{M_0}{4D\alpha} (r^2 - R_c^2) - \frac{M_0 R_t^2}{2D\alpha} \ln \left(\frac{r}{R_{\text{cap}}} \right) \quad (1.2)$$

Thus, given a small number of geometric and biophysical parameters and P_{cap} at a given location, the Krogh model is able to predict the radial variation in tissue PO_2 , including the minimum PO_2 , which occurs at the outer edge of the tissue cylinder, namely $r = R_t$ [32].

Many variants have been incorporated into the Krogh model to improve its physiological accuracy and better match the experiments. The most relevant ones are made while maintaining the Krogh geometry settings, namely assumptions 1 ÷ 5.

- *PO_2 -dependent O_2 consumption.* The local tissue O_2 consumption rate is found experimentally to be nearly constant for tissue PO_2 above a certain critical value. Below this value, O_2 consumption drops sharply to zero, possibly due to diffusion limitation of O_2 flux into mitochondria. Then a mathematical model of PO_2 -dependent consumption is required to study situations in which hypoxia is expected. The most common model is the Michaelis-Menten model, which uses first-order kinetics [32, 60] and, although it does not keep O_2 strictly constant above the threshold, it gives a reasonable approximation, being more computationally convenient.

- *Intravascular O₂ transport resistance.* The existence of intravascular PO₂ gradients implies a finite IVR to blood-tissue O₂ transport. In many models of O₂ transport to tissue, intravascular O₂ transport is directly included. However, when this approach is not desirable (e.g., for network problems where the computational cost would be too high), MTCs computed separately can be included in the vessel-tissue transport problem. This fact is typically done by using a flux boundary condition on tissue PO₂ at the outer edge of the microvessel wall instead of the continuous PO₂ condition of the Krogh model, as shown in [32].
- *Mb facilitation of O₂ diffusion.* The Mb molecule found in the heart and striated muscle can bind and release O₂ similarly to Mb and its movement can enhance O₂ diffusion. Since Mb has only one heme group, there is no cooperativity of binding. Using Fick's law, obtaining a steady-state equation for tissue O₂ diffusion and consumption is possible, in which Mb gives tissue some resistance to localized hypoxia by increasing diffusion to low-PO₂ regions [32].
- *Axial O₂ diffusion in the tissue.* This feature has also been found to be important in modeling microvascular O₂ transport because each slice of the tissue cylinder is not independent but can exchange O₂ with its neighbors. Axial diffusion in flowing microvessels becomes less relevant due to the greater effect of axial convection. The latter can be quantified with the Péclet number $\text{Pe} = \frac{vL}{D}$, which represents the importance of transport by convection (proportional to blood or RBC velocity v) relative to transport by diffusion (proportional to $\frac{D}{L}$ for diffusion coefficient D and length scale L). For a typical capillary RBC velocity of 200 μm/s and length of 500 μm, and a typical diffusivity of $4 \cdot 10^{-5}$ cm² s⁻¹, we have Pe = 25. This number will be larger in arterioles and venules, and axial diffusion can be neglected inside most flowing microvessels [32].
- *Time-dependent O₂ transport.* The convective O₂ supply to individual capillaries can vary considerably over time (e.g., due to upstream arteriolar vasomotion), and there are many exciting problems in which time-dependent O₂ transport is relevant (e.g., the onset of ischemia or exercise). Therefore, several studies have used time-dependent Krogh-type models. The necessary mathematical description involves time-dependent equations with appropriate initial and external boundary conditions and a capillary-tissue interface condition [32].

Schumacker and Samsel [100] used a Krogh model with PO₂-dependent consumption to analyze O₂ delivery and tissue uptake. The results of this model confirmed the limitations of the Krogh model in situations in which transport heterogeneity is essential.

Lagerlund and Low [60] used a Krogh-type model with axial diffusion, Michaelis-Menten consumption, and no IVR to study steady-state O₂ transport in rat peripheral nerve tissue. They solved the steady-state equations using the FDM and found better agreement with the experiments for reduced O₂ supply than in a model with constant O₂ consumption and no axial diffusion. They solved the steady-state equations using the FEM and found better agreement with the experiments for reduced O₂ supply than in a model with constant O₂ consumption and no axial diffusion.

Single-vessel multi-species models

Krogh-type can also be used to study the blood-tissue transport of other substances beyond O₂, where the latter is coupled to the former. Indeed, transport of other species can be equally crucial in studying O₂ transport. In the same cases, O₂ transport affects the other species (e.g., O₂-dependent production and consumption of NO) [32], while in other cases, the species can affect O₂ transport itself, i.e., by competing with O₂ for binding to Hb (as does CO) or by shifting the Hb–O₂ saturation curve.

Li et al. [64] used a Krogh-type model with four concentric layers (RBC, plasma, interstitial fluid, and parenchymal cells) to study the tracer kinetics of O–O₂ and O–H₂O. This model considered axial but not radial gradients within each layer (or compartment) and exchanges between the layers. The steady-state O₂ distribution was first calculated and then used to model coupled dynamics of labeled O₂ and water. By fitting model solutions to experimental tracer curves, this model can be used to estimate myocardial O₂ consumption.

Schacterle et al. [99] developed a simple steady-state model of O₂/CO₂ transport in arterioles surrounded by tissue containing a continuous distribution of capillaries. The results showed that PCO₂ goes closer to equilibrium with surrounding tissue than PO₂.

Kirkpatrick et al. [55] used a Krogh-type model to study O₂ and glucose transport in tumors. They showed that glycolysis has only a minor effect on tumor hypoxia but that hypoxia is very sensitive to the O₂ consumption rate. Moreover, their work showed that using a distribution of tissue cylinder sizes the hypoxic fraction increases more than using a single cylinder.

Parallel capillary models

The above variants to the standard Krogh model do not consider O_2 diffusion between microvessels, which is considered to be very important in many physiological situations. Studying O_2 transport by realistic microvascular networks, and in particular, to address Krogh model assumptions 6 ÷ 8, the first step is to consider parallel arrays of capillaries.

Gleitzman et al. [57] developed a model of steady-state O_2 transport that neglects IVR but includes dissolved and Hb-bound O_2 in the blood and diffusion between capillaries (with concurrent blood flow) and tissue in planes perpendicular to the capillary axis. This model presented a grid of 16 equally spaced capillaries and was solved using the FDM to study the effect of heterogeneities in O_2 delivery on tissue PO_2 distributions. Using probability distributions to set the RBC supply rate, capillary inlet SO_2 , and Michaelis-Menten consumption, it was shown that both mean and minimum tissue PO_2 decreased as the dispersion of these supply parameters increased [32].

Groebe and Thews [38] considered 3D O_2 transport in a single working muscle fiber surrounded by parallel capillaries with increased axial Mb diffusivity. Using an approximate analytical solution including discrete RBC inside the capillaries, they showed that a variant of the Krogh model including IVR gave good agreement with their 3D model when the capillary-to-fiber ratio was close to 1, but that the former and Hill models disagreed considerably with their model when the capillary-to-fiber ratio was close to 2.

Salathe [98] presented a method for calculating the steady-state O_2 distribution due to an array of capillaries in the absence of IVR and variable O_2 consumption. The model performs matching of average O_2 fluxes and concentrations between neighboring rectangular tissue domains surrounding each capillary to derive a system of ODEs for capillary O_2 coupled to a system of AEs for average tissue domain boundary O_2 .

Capillary network models

Hsu and Secomb [101] introduced a steady-state model of O_2 transport in capillary networks and surrounding tissue based on Green's function method [113]. The solution method was computationally efficient because it reduced the 3D problem for tissue PO_2 to a 1D problem of finding appropriate source terms for each capillary segment.

Groebe [37] extended a previous parallel capillary model [38] to the case of 3D O_2 transport from capillary networks. Some applications of this model aim at heavily working muscle fiber supplied by four capillaries: the result, in this case, is following the single-fiber one.

Goldman and Popel [33] showed a model based on the FDM, which allowed the study of O₂ transport by branching networks of microvessels. This model includes 3D diffusion, IVR, Mb facilitation, dissolved and Hb–bound O₂ in the blood; moreover, it can be possible to calculate steady-state or time-dependent solutions. The model was used to study the effect of capillary network geometry on steady-state O₂ transport in the hamster cheek pouch retractor muscle.

Wieringa et al. [121] presented a 3D network model of steady-state O₂ transport in the heart that assumed constant O₂ consumption and was solved in 2D layers by the FEM. The model presented some simplifications but showed the importance of intercapillary diffusion, mainly when flow direction and path length are heterogeneous. The results showed that venous PO₂ is a poor indicator of actual tissue oxygenation.

Beard and Bassingthwaigte [12] introduced a network model of the heart using 16 parallel capillaries on a hexagonal grid with 160 random cross-connections and included 3D diffusion, Mb facilitation, and Michaelis-Menten consumption. Using the FDM, they showed that steady-state O₂ distributions were much more heterogeneous than a Krogh-type model would predict and that Mb could reduce tissue hypoxia, but only for a modest range of consumption rates.

2 | Mathematical models

In this chapter, we provide the mathematical models employed for

- blood dynamics in epicardial coronary arteries in Section 2.1;
- blood dynamics in intramural coronary vessels in Section 2.2;
- exchange in microvasculature in Section 2.3.

We mainly focus on the latter, the object of this work, while regarding the others, we refer to the work of Di Gregorio et al. [25], in which more details about model derivations, coupling, and numerical approximation are provided.

Following [25], we adopt a multi-physics model for the blood dynamics in the epicardial coronary arteries, whereas a multi-compartment Darcy model is used to model blood dynamics in the intramural coronary vessels. This model is well suited to be coupled with the 3D description of the coronary flow because they share the same geometric dimension and mathematical structure. The coupling occurs, as we explain in Section 2.4.1 at multiple levels: directly, through interface conditions based on the continuity of mass and momentum, and indirectly, through the virtual network of intramural vessels.

In Section 2.3, we provide the derivation of the oxygenation model presented by Regazzoni in [95]. Then, this model is one-way coupled with the third compartment of the three-compartments Darcy model in Section 2.4.2.

Finally, in Section 2.4.3 the whole multi-physics model is built up.

2.1. Blood dynamics in epicardial coronary arteries

As shown in Figure 2.1, the blood dynamics in the epicardial coronary artery domain Ω_C is modeled through the Navier-Stokes equations for an incompressible, homogeneous, and Newtonian fluid under the assumption of rigid walls. Although far more computationally expensive than 1D flow models, 3D models ensure better accuracy and fit of coronary shapes.

The equations Navier-Stokes equations read

$$\left\{ \begin{array}{ll} \rho \left(\frac{\partial \mathbf{u}_C}{\partial t} + (\mathbf{u}_C \cdot \nabla) \mathbf{u}_C \right) - \mu_C \nabla \cdot (\nabla \mathbf{u}_C + (\nabla \mathbf{u}_C)^T) + \nabla p_C = \mathbf{0} & \text{in } \Omega_C, \quad (2.1a) \\ \nabla \cdot \mathbf{u}_C = 0 & \text{in } \Omega_C, \quad (2.1b) \\ \mathbf{u}_C = \mathbf{0} & \text{on } \Gamma_w, \quad (2.1c) \\ \mathbf{u}_C = \mathbf{u}_{in} & \text{on } \Gamma_{in}, \quad (2.1d) \end{array} \right.$$

where \mathbf{u}_C [m s^{-1}] and p_C [mmHg] are the blood velocity and pressure, respectively, in the epicardial coronary arteries, ρ [kg m^{-3}] the blood density (assumed to be constant), μ_C [mmHg s] the blood viscosity; Γ_w is the lateral physical vessel wall, where a no-slip condition is prescribed. The surface Γ_w also includes the outlet sections feeding the right ventricle, if only the left myocardium is considered, and the atria, where we assume that the flow rate is negligible with respect to the ventricular outlets; Γ_{in} is the inlet section representing the coronary left and right ostia located at the aortic root, where a physiological velocity profile \mathbf{u}_{in} is imposed.

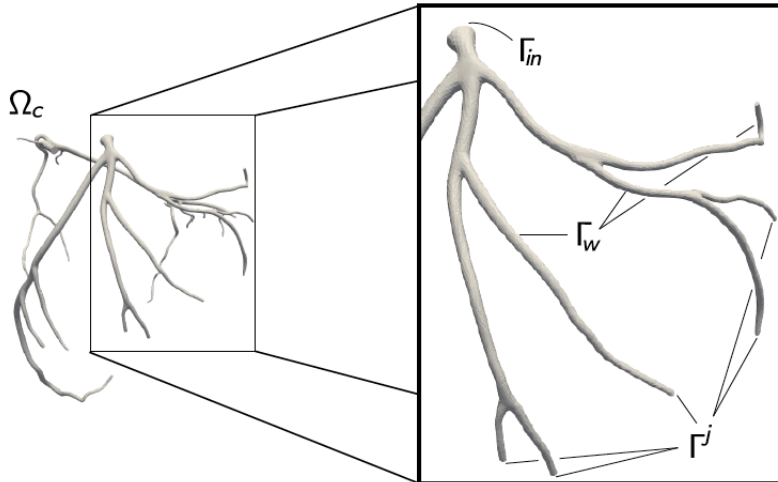


Figure 2.1: Sketch of the computational domain for the epicardial coronary arteries [25].

As we can notice from Figure 2.1, the computational domain is also composed of the distal outflow sections $\Gamma^j, j = 1, \dots, J$. Here, the coupling with the intramural vasculature is considered. The corresponding coupling interface conditions will be discussed in Section 2.4.1.

Some reasonable physiological values for the involved parameters are provided in [25] and listed in Table 2.1. Finally, the input velocity profile \mathbf{u}_{in} will be provided and discussed in Section 4.2.3.

Variable	Measure unit	Value
ρ	kg m^{-3}	$1.06 \cdot 10^{-3}$
μ_C	mmHg s	$2.63 \cdot 10^{-5}$

Table 2.1: List of fluid dynamics parameters.

2.2. Blood dynamics in intramural coronary vessels

The multi-compartment Darcy model describes the blood dynamics in the intramural vascular network, accounting for the different length scales in small arteries, arterioles, and capillaries. This approach subdivides the intramural coronary vessels into distinct compartments, each modeled as a porous medium but solved in the same computational domain, i.e., the whole myocardium [21, 47, 68, 115].

Using the Darcy equation in each compartment, the multi-compartment Darcy model provides an effective scale separation of blood flow in the intramural vessels. The compartments coexist in the same domain Ω_M , representing the myocardium, as illustrated in Figure 2.2.

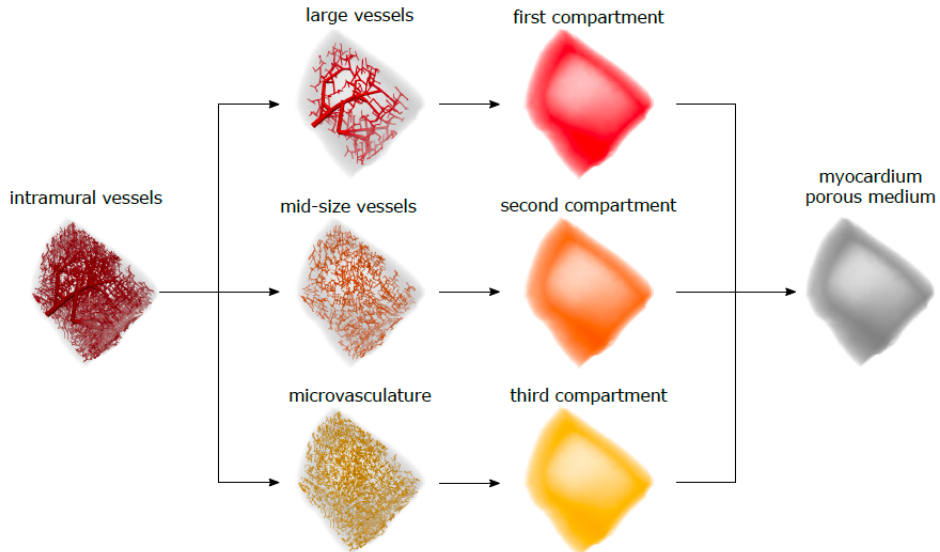


Figure 2.2: Schematic overview of the multi-compartment porous medium in a piece of myocardium in case of three compartments: the intramural vessels are subdivided into three groups, each group will characterize a different compartment. The three compartments coexist in the myocardium [25].

Being N the number of compartments, the equations Darcy flow for compartment $i = 1, \dots, N$ are

$$\left\{ \begin{array}{ll} \mathbf{K}_i^{-1} \mathbf{u}_i + \nabla p_i = \mathbf{0} & \text{in } \Omega_M, \\ \nabla \cdot \mathbf{u}_i = g_i - \sum_{k=1}^N \beta_{i,k} (p_i - p_k) & \text{in } \Omega_M, \\ \mathbf{u}_i \cdot \mathbf{n} = 0 & \text{on } \partial\Omega_M, \end{array} \right. \quad (2.2a)$$

$$(2.2b)$$

$$(2.2c)$$

where in compartment i for $i = 1 \dots N$, \mathbf{u}_i denotes the blood velocity, p_i is the pore pressure, \mathbf{K}_i [$\text{m}^2 \text{s}^{-1} \text{mmHg}^{-1}$] the permeability tensor, g_i [s^{-1}] a volumetric source or sink term and $\beta_{i,k}$ [$\text{s}^{-1} \text{mmHg}^{-1}$] for $i, k = 1 \dots N$, represent the (non-negative) inter-compartment pressure coupling coefficients. Due to mass conservation, we assume that the divergence of the Darcy velocity is compensated by a source or sink external term and by mass exchanges between different compartments, which depend on the pressure jumps between the latter. To enforce mass conservation among compartments, we have that $\beta_{i,k} = \beta_{k,i}$, $\forall i, k = 1, \dots, N$. Moreover, $\beta_{i,k} \neq 0$ whenever $k = i \pm 1$ for $2 \leq i \leq N-1$, $k = 2$ for $i = 1$, $k = N-1$ for $i = N$, since the compartment i exchanges mass only with adjacent compartments. We refer again to [25] for estimating such and other parameters.

The first compartment, i.e., $i = 1$, is the most proximal one and the corresponding g_1 depends on the blood dynamics in epicardial coronary arteries. Instead, we have $g_j = 0$, $j = 2, \dots, N-1$, since the intermediate compartments do not exchange mass with the external environment. Finally, the volumetric term of the small scale compartment g_N (i.e., the one corresponding to the microvasculature) is a sink term that accounts for coronary venous return, namely

$$g_N = -\gamma (p_N - p_{\text{veins}}),$$

where p_{veins} [Pa] denotes the venous pressure and γ [$\text{s}^{-1} \text{mmHg}^{-1}$] is a drain coefficient.

For our purposes, we represent intramural vessels employing $N = 3$ compartments [47] in which the intramural coronary vessels have a diameter in the range of

- $\sim 200 \text{ }\mu\text{m} \div 1 \text{ mm}$ for large intramural vessel ($i = 1$);
- $\sim 60 \div 200 \text{ mm}$ for mid-size intramural vessels ($i = 2$);
- $\sim 5 \div 60 \text{ }\mu\text{m}$ for microvasculature ($i = 3$).

The three-compartments Darcy model is the following.

$$\left\{ \begin{array}{ll} \mathbf{u}_1 + \mathbf{K}_1 \nabla p_1 = \mathbf{0} & \text{in } \Omega_M, \\ \nabla \cdot \mathbf{u}_1 = g_1 - \beta_{1,2} (p_1 - p_2) & \text{in } \Omega_M, \\ \mathbf{u}_1 \cdot \mathbf{n} = 0 & \text{on } \partial\Omega_M, \\ \mathbf{u}_2 + \mathbf{K}_2 \nabla p_2 = \mathbf{0} & \text{in } \Omega_M, \\ \nabla \cdot \mathbf{u}_2 = -\beta_{2,1} (p_2 - p_1) - \beta_{2,3} (p_2 - p_3) & \text{in } \Omega_M, \\ \mathbf{u}_2 \cdot \mathbf{n} = 0 & \text{on } \partial\Omega_M, \\ \mathbf{u}_3 + \mathbf{K}_3 \nabla p_3 = \mathbf{0} & \text{in } \Omega_M, \\ \nabla \cdot \mathbf{u}_3 = -\gamma (p_3 - p_{\text{veins}}) - \beta_{3,2} (p_3 - p_2) & \text{in } \Omega_M, \\ \mathbf{u}_3 \cdot \mathbf{n} = 0 & \text{on } \partial\Omega_M. \end{array} \right. \quad \begin{array}{l} (2.3a) \\ (2.3b) \\ (2.3c) \\ (2.3d) \\ (2.3e) \\ (2.3f) \\ (2.3g) \\ (2.3h) \\ (2.3i) \end{array}$$

If we substitute the equation (2.2a) in (2.2b), the velocity is eliminated, and we obtain the primal Darcy formulation, which is written in terms of only pressure variables p_i , namely for the general N compartments, and it is

$$\left\{ \begin{array}{ll} -\nabla \cdot (\mathbf{K}_i \cdot \nabla p_i) = g_i - \sum_{k=1}^N \beta_{i,k} (p_i - p_k) & \text{in } \Omega_M, \\ (-\mathbf{K}_i \cdot \nabla p_i) \cdot \mathbf{n} = 0 & \text{on } \partial\Omega_M. \end{array} \right. \quad \begin{array}{l} (2.4a) \\ (2.4b) \end{array}$$

The velocities \mathbf{u}_i can be obtained after post-processing of computed pressures in (2.4) as

$$\mathbf{u}_i = -\mathbf{K}_i \cdot \nabla p_i \text{ in } \Omega_M. \quad (2.5)$$

Accordingly, the three-compartments Darcy problem in primal formulation, reads as follows.

$$\left\{ \begin{array}{ll} -\nabla \cdot (\mathbf{K}_1 \cdot \nabla p_1) = g_1 - \beta_{1,2} (p_1 - p_2) & \text{in } \Omega_M, \\ \mathbf{u}_1 \cdot \mathbf{n} = 0 & \text{on } \partial\Omega_M, \\ -\nabla \cdot (\mathbf{K}_2 \cdot \nabla p_2) = -\beta_{2,1} (p_2 - p_1) - \beta_{2,3} (p_2 - p_3) & \text{in } \Omega_M, \\ \mathbf{u}_2 \cdot \mathbf{n} = 0 & \text{on } \partial\Omega_M, \\ -\nabla \cdot (\mathbf{K}_3 \cdot \nabla p_3) = -\gamma (p_3 - p_{\text{veins}}) - \beta_{3,2} (p_3 - p_2) & \text{in } \Omega_M, \\ \mathbf{u}_3 \cdot \mathbf{n} = 0 & \text{on } \partial\Omega_M. \end{array} \right. \quad \begin{array}{l} (2.6a) \\ (2.6b) \\ (2.6c) \\ (2.6d) \\ (2.6e) \\ (2.6f) \end{array}$$

Variable	Measure unit	Value
γ	$s^{-1} \text{ mmHg}^{-1}$	0.0133
p_{veins}	mmHg	22.5
$\beta_{1,2}$	$s^{-1} \text{ mmHg}^{-1}$	$3.5 \cdot 10^{-4}$
$\beta_{2,3}$	$s^{-1} \text{ mmHg}^{-1}$	$4.8 \cdot 10^{-4}$
$\beta_{1,3}$	$s^{-1} \text{ mmHg}^{-1}$	0
K_1	$\text{m}^2 \text{ s}^{-1} \text{ mmHg}^{-1}$	$7.8 \cdot 10^{-3} \cdot \mathbb{I}$
K_2	$\text{m}^2 \text{ s}^{-1} \text{ mmHg}^{-1}$	$1.1 \cdot 10^{-8} \cdot \mathbb{I}$
K_3	$\text{m}^2 \text{ s}^{-1} \text{ mmHg}^{-1}$	$0.133 \cdot \mathbb{I}$

Table 2.2: List of Darcy problem parameters.

The algebraic problems related to the primal formulation are characterized by a lower number of degrees of freedom. For this reason, they are easier and faster to solve than those related to the standard formulation, and the computational cost of numerical simulations could be reduced. However, the post-processing of the pressure needed to recover the velocity field entails a loss of accuracy in the computation of the latter.

Some reasonable physiological values for the involved parameters are provided in [25, 69] and listed in Table 2.2. The sink term g_1 is responsible for the coupling with the fluid problem and will be provided and discussed in Section 2.4.1.

2.3. Oxygen exchange in microvasculature

In this section, we derive the multi-physics oxygenation model concerning the dynamics of oxygen saturation SO_2 [–], oxygen concentration $[\text{O}_2*]$ [mol m^{-3}] and oxygen partial pressure PO_2 [mmHg] in the capillaries blood, and of oxygen partial pressure in the muscle PO_2^m [mmHg]. Finally, we discuss the parameters involved in the equations and we recover a reduced model, computationally more affordable as shown in Section 4.2.1.

In this section, we adopt splitting strategy of Section 2.2 into three compartments (large, medium, and minor diameter), respectively denoted by $i = 1, 2, 3$. Moreover, we consider existing an initial compartment $i = a$ upstream from these, representing the arterial blood, and another one $i = m$ downstream from these, representing the cardiac muscle.

In addition to the already defined variables, we also define for $i, j = 1, 2, 3, m$:

- ψ_i [–] the volume fraction of compartment i , so that $\psi_1 + \psi_2 + \psi_3 + \psi_m = 1$;
- $\rho_i = \psi_i \rho$ [kg m^{-3}] the effective density of the blood in the compartment i ;
- $\Phi_{i,j}$ [$\text{kg m}^{-3} \text{s}^{-1}$] the mass flux per unit volume between compartment i and j ;
- $\hat{\phi}_{i,j} = \rho^{-1} \Phi_{i,j}$ [s^{-1}] the volume flux per unit volume between compartments.

2.3.1. Oxygen-hemoglobin association/dissociation

Let us consider the oxygen-hemoglobin association/dissociation chemical reaction



where k_+ , k_- [s^{-1}] are the association/dissociation rate constant while n [–] is the hemoglobin's number sites for oxygen. Each hemoglobin has $n = 4$ binding sites for oxygen. However, experimental curves find better fits for $n \simeq 3$ (possibly fractional). Hence, n could be considered an effective (averaged) value. The law of mass action entails that in an isolated domain

$$\left\{ \begin{array}{l} \frac{d}{dt}[\text{O}_2] = n(k_-[\text{Hb-O}_2] - k_+[\text{Hb}][\text{O}_2]^n), \\ \frac{d}{dt}[\text{Hb}] = k_-[\text{Hb-O}_2] - k_+[\text{Hb}][\text{O}_2]^n, \end{array} \right. \quad (2.8a)$$

$$\left\{ \begin{array}{l} \frac{d}{dt}[\text{Hb-O}_2] = -k_-[\text{Hb-O}_2] + k_+[\text{Hb}][\text{O}_2]^n, \end{array} \right. \quad (2.8b)$$

$$\left\{ \begin{array}{l} \frac{d}{dt}[\text{Hb-O}_2] = -k_-[\text{Hb-O}_2] + k_+[\text{Hb}][\text{O}_2]^n, \end{array} \right. \quad (2.8c)$$

where $[X]$ [mol m^{-3}] denotes the concentration of X in the blood.

2.3.2. Mass conservation

Let us consider the volume flux per unit volume $\hat{\phi}_{i,j}$ between two compartments. Through the mass conservation, we have

$$\frac{\partial}{\partial t}\psi_i + \nabla \cdot (\rho_i \mathbf{u}_i) = \hat{\phi}_{i-1,i} - \hat{\phi}_{i,i+1}. \quad (2.9)$$

We assume that the volume of the compartments does not vary in time, namely that

$$\frac{\partial}{\partial t}\psi_i = 0 \quad \forall i = 1, 2, 3,$$

thus we get

$$\nabla \cdot (\rho_i \mathbf{u}_i) = \hat{\phi}_{i-1,i} - \hat{\phi}_{i,i+1}. \quad (2.10)$$

The average CBF $\bar{\Psi}_{\text{CBF}}$ [$\text{mL min}^{-1} \text{g}^{-1}$] from the compartment $i-1$ to i , inside the myocardium volume Ω_M , and during a heart cycle $[0, T]$, is nearly $0.8 \text{ mL min}^{-1} \text{g}^{-1}$ [51] and it can be computed as

$$\bar{\Psi}_{\text{CBF}} := \frac{1}{T|\Omega_M|} \int_0^T \int_{\Omega_M} \rho^{-1} \Phi_{i-1,1} \, d\mathbf{x} \, dt = \frac{1}{T|\Omega_M|} \int_0^T \int_{\Omega_M} \hat{\phi}_{i-1,1} \, d\mathbf{x} \, dt. \quad (2.11)$$

Starting from the oxygen-hemoglobin association/dissociation chemical reaction, we can derive the equations describing the mass conservation of the quantity of oxygen, hemoglobin, and oxyhemoglobin, that depend on several contributions, such as chemical reactions (2.8), advection, flux from neighboring compartments, and outgoing the considered one.

Moreover, we also want to consider the vascular membrane's permeability to be permeable to oxygen but not hemoglobin. Hence, only for the mass conservation of the quantity of oxygen, we need to take into account also the oxygen exchanged with the muscle, as in the sixth row of its mass conservation equation. Then, we define $\frac{A_v^i}{V_t} [\text{m}^{-1}]$ to be the area of vascular surface per unit volume of tissue and $P [\text{m s}^{-1}$ corresponding to $\text{m}^3 \text{s}^{-1} \text{m}^{-2}$] to be the membrane permeability. We assume that

$$\frac{A_v^3}{V_t} \gg \frac{A_v^2}{V_t} \gg \frac{A_v^1}{V_t},$$

namely that oxygen is exchanged only by the third compartment.

With this aim, let us consider a volume of tissue V , so that the amount of oxygen, hemoglobin and oxyhemoglobin stored within the compartment i inside V is given by

$$\int_V [\text{O}_2]^i \psi_i \, d\mathbf{x}, \quad \int_V [\text{Hb}]^i \psi_i \, d\mathbf{x}, \quad \int_V [\text{Hb-O}_2]^i \psi_i \, d\mathbf{x}$$

respectively.

Taking into account the contributions above and denoting by $(x)_+ = \max(x, 0)$ the positive part of the field x , we obtain that the variation of these quantities is

$$\left\{ \begin{array}{l} \frac{d}{dt} \int_V [\text{O}_2]^i \psi_i \, d\mathbf{x} = \int_V \psi_i n (k_- [\text{Hb-O}_2]^i - k_+ [\text{Hb}]^i ([\text{O}_2]^i)^n) \, d\mathbf{x} \\ \quad - \int_{\partial V} [\text{O}_2]^i \psi_i^{-1} \mathbf{u}_i \cdot \mathbf{n} \, d\gamma \\ \quad + \int_V \mu \Delta [\text{O}_2]^i \, d\mathbf{x} \\ \quad + \int_V \rho^{-1} (\Phi_{i-1,i})_+ [\text{O}_2]^{i-1} \, d\mathbf{x} + \int_V \rho^{-1} (\Phi_{i+1,i})_+ [\text{O}_2]^{i+1} \, d\mathbf{x} \\ \quad - \int_V \rho^{-1} ((\Phi_{i,i-1})_+ + (\Phi_{i,i+1})_+) [\text{O}_2]^i \, d\mathbf{x} \\ \quad - \int_V \frac{A_v^i}{V_t} P([\text{O}_2]^i - [\text{O}_2]^m) \delta_{i3} \, d\mathbf{x}, \\ \frac{d}{dt} \int_V [\text{Hb}]^i \psi_i \, d\mathbf{x} = \int_V \psi_i (k_- [\text{Hb-O}_2]^i - k_+ [\text{Hb}]^i ([\text{Hb}]^i)^n) \, d\mathbf{x} \\ \quad - \int_{\partial V} [\text{Hb}]^i \psi_i^{-1} \mathbf{u}_i \cdot \mathbf{n} \, d\gamma \\ \quad + \int_V \mu \Delta [\text{Hb}]^i \, d\mathbf{x} \\ \quad + \int_V \rho^{-1} (\Phi_{i-1,i})_+ [\text{Hb}]^{i-1} \, d\mathbf{x} + \int_V \rho^{-1} (\Phi_{i+1,i})_+ [\text{Hb}]^{i+1} \, d\mathbf{x} \\ \quad - \int_V \rho^{-1} ((\Phi_{i,i-1})_+ + (\Phi_{i,i+1})_+) [\text{Hb}]^i \, d\mathbf{x}, \\ \frac{d}{dt} \int_V [\text{Hb-O}_2]^i \psi_i \, d\mathbf{x} = \int_V \psi_i (- (k_- [\text{Hb-O}_2]^i - k_+ [\text{Hb}]^i ([\text{Hb-O}_2]^i)^n)) \, d\mathbf{x} \\ \quad - \int_{\partial V} [\text{Hb-O}_2]^i \psi_i^{-1} \mathbf{u}_i \cdot \mathbf{n} \, d\gamma \\ \quad + \int_V \mu \Delta [\text{Hb-O}_2]^i \, d\mathbf{x} \\ \quad + \int_V \rho^{-1} (\Phi_{i-1,i})_+ [\text{Hb-O}_2]^{i-1} \, d\mathbf{x} + \int_V \rho^{-1} (\Phi_{i+1,i})_+ [\text{Hb-O}_2]^{i+1} \, d\mathbf{x} \\ \quad - \int_V \rho^{-1} ((\Phi_{i,i-1})_+ + (\Phi_{i,i+1})_+) [\text{Hb-O}_2]^i \, d\mathbf{x}, \end{array} \right.$$

where in each equation

- the first row is the variation due to chemical reactions;
- the second row is related to advection;
- the third row is related to diffusion;
- the fourth row is the flux from the neighboring compartments;
- the fifth row is the flux outgoing from the considered compartment.

We recall that $\Phi_{i,j}$ is the flux of blood mass per unit volume of tissue, so that $\rho^{-1}\Phi_{i,j}$ is the flux of blood volume per unit volume of tissue. Hence, applying the divergence theorem to the boundary term and, since V is arbitrary, we get

$$\left\{ \begin{array}{l} \frac{\partial}{\partial t}[\text{O}_2]^i = n(k_-[\text{Hb-O}_2]^i - k_+[\text{Hb}]^i([\text{O}_2]^i)^n) \\ \quad - \psi_i^{-1} \nabla \cdot ([\text{O}_2]^i \mathbf{u}_i) + \mu \Delta [\text{O}_2]^i \\ \quad + \psi_i^{-1} (\widehat{\phi}_{i-1,i})_+ [\text{O}_2]^{i-1} + \psi_i^{-1} (\widehat{\phi}_{i+1,i})_+ [\text{O}_2]^{i+1} \\ \quad - \psi_i^{-1} \left((\widehat{\phi}_{i,i-1})_+ + (\widehat{\phi}_{i,i+1})_+ \right) [\text{O}_2]^i \\ \quad - \psi_i^{-1} \frac{A_v^i}{V_t} P([\text{O}_2]^i - [\text{O}_2]^m) \delta_{i3}, \\ \frac{\partial}{\partial t}[\text{Hb}]^i = (k_-[\text{Hb-O}_2]^i - k_+[\text{Hb}]^i([\text{Hb}]^i)^n) \\ \quad - \psi_i^{-1} \nabla \cdot ([\text{Hb}]^i \mathbf{u}_i) + \mu \Delta [\text{Hb}]^i \\ \quad + \psi_i^{-1} (\widehat{\phi}_{i-1,i})_+ [\text{Hb}]^{i-1} + \psi_i^{-1} (\widehat{\phi}_{i+1,i})_+ [\text{Hb}]^{i+1} \\ \quad - \psi_i^{-1} \left((\widehat{\phi}_{i,i-1})_+ + (\widehat{\phi}_{i,i+1})_+ \right) [\text{Hb}]^i, \\ \frac{\partial}{\partial t}[\text{Hb-O}_2]^i = - (k_-[\text{Hb-O}_2]^i - k_+[\text{Hb}]^i([\text{Hb-O}_2]^i)^n) \\ \quad - \psi_i^{-1} \nabla \cdot ([\text{Hb-O}_2]^i \mathbf{u}_i) + \mu \Delta [\text{Hb-O}_2]^i \\ \quad + \psi_i^{-1} (\widehat{\phi}_{i-1,i})_+ [\text{Hb-O}_2]^{i-1} + \psi_i^{-1} (\widehat{\phi}_{i+1,i})_+ [\text{Hb-O}_2]^{i+1} \\ \quad - \psi_i^{-1} \left((\widehat{\phi}_{i,i-1})_+ + (\widehat{\phi}_{i,i+1})_+ \right) [\text{Hb-O}_2]^i. \end{array} \right. \quad \begin{array}{l} (2.13a) \\ (2.13b) \\ (2.13c) \end{array}$$

From now on, we assume that blood always flows downstream, i.e. $\widehat{\phi}_{i,j} \geq 0 \forall i > j$ and $\widehat{\phi}_{i,j} = 0 \forall i \leq j$. This fact entails

$$\left\{ \begin{array}{l} \frac{\partial}{\partial t} [\text{O}_2]^i = n \left(k_- [\text{Hb-O}_2]^i - k_+ [\text{Hb}]^i ([\text{O}_2]^i)^n \right) \\ \quad - \psi_i^{-1} \nabla \cdot ([\text{O}_2]^i \mathbf{u}_i) + \mu \Delta [\text{Hb}] \\ \quad + \psi_i^{-1} \widehat{\phi}_{i-1,i} [\text{O}_2]^{i-1} - \psi_i^{-1} \widehat{\phi}_{i,i+1} [\text{O}_2]^i \\ \quad - \psi_i^{-1} \frac{A_v^i}{V_t} P([\text{O}_2]^i - [\text{O}_2]^m) \delta_{i3}, \\ \frac{\partial}{\partial t} [\text{O}_2]^i = (k_- [\text{Hb-O}_2]^i - k_+ [\text{Hb}]^i ([\text{O}_2]^i)^n) \\ \quad - \psi_i^{-1} \nabla \cdot ([\text{Hb}]^i \mathbf{u}_i) + \mu \Delta [\text{Hb}] \\ \quad + \psi_i^{-1} \widehat{\phi}_{i-1,i} [\text{Hb}]^{i-1} - \psi_i^{-1} \widehat{\phi}_{i,i+1} [\text{Hb}]^i, \\ \frac{\partial}{\partial t} [\text{Hb-O}_2]^i = - (k_- [\text{Hb-O}_2]^i - k_+ [\text{Hb}]^i ([\text{O}_2]^i)^n) \\ \quad - \psi_i^{-1} \nabla \cdot ([\text{Hb-O}_2]^i \mathbf{u}_i) + \mu \Delta [\text{Hb-O}_2] \\ \quad + \psi_i^{-1} \widehat{\phi}_{i-1,i} [\text{Hb-O}_2]^{i-1} - \psi_i^{-1} \widehat{\phi}_{i,i+1} [\text{Hb-O}_2]^i. \end{array} \right. \begin{array}{l} (2.14a) \\ (2.14b) \\ (2.14c) \end{array}$$

Finally, we define the average amount of oxygen delivered from capillaries to the muscle $\lambda_{\text{O}_2}^{\text{del}}(t)$ [mol m⁻³], which can be computed as

$$\lambda_{\text{O}_2}^{\text{del}}(t) = \frac{1}{|\Omega_M|} \int_{\Omega_M} \frac{A_v^3}{V_t} P([\text{O}_2]^3 - [\text{O}_2]^m) d\mathbf{x}, \quad (2.15)$$

and the total amount of oxygen delivered from capillaries to the muscle $\Lambda_{\text{O}_2}^{\text{del}}(t)$ [mol m⁻³ s⁻¹] computable integrating the latter in the time interval [0, t], namely

$$\Lambda_{\text{O}_2}^{\text{del}}(t) = \int_0^t \lambda_{\text{O}_2}^{\text{del}}(u) du. \quad (2.16)$$

These are quantities of interest that we compute after solving the oxygenation problem.

2.3.3. Equations in terms of SO₂ and PO₂

We define, for each compartment, the total hemoglobin concentration

$$[\text{Hb}*]^i := [\text{Hb}]^i + [\text{Hb-O}_2]^i,$$

namely the sum of concentrations of hemoglobin and oxyhemoglobin inside the considered compartment.

By summing the first two lines of (2.14), we get

$$\frac{\partial}{\partial t}[\text{Hb*}]^i + \psi_i^{-1}\nabla \cdot ([\text{Hb*}]^i \mathbf{u}_i) + \mu\Delta[\text{Hb*}] = \psi_i^{-1}\widehat{\phi}_{i-1,i}[\text{Hb*}]^{i-1} - \psi_i^{-1}\widehat{\phi}_{i,i+1}[\text{Hb*}]^i. \quad (2.17)$$

Since we assumed that hemoglobin is never exchanged through the vascular membrane or the surrounding environment, we expect $[\text{Hb*}]^i$ to be constant in space and time and the same for each compartment. Therefore, we consider $[\text{Hb*}]$ as a constant.

We the oxygen saturation as the proportion of oxygenated hemoglobin concentration over the total one, namely

$$\text{SO}_2^i = \frac{[\text{Hb-O}_2]^i}{[\text{Hb*}]},$$

we get

$$[\text{Hb-O}_2]^i = \text{SO}_2^i[\text{Hb*}], \quad (2.18)$$

and thus, using the definition of total hemoglobin concentration, we obtain

$$[\text{Hb}]^i = (1 - \text{SO}_2^i)[\text{Hb*}]. \quad (2.19)$$

Then, we can drop one line from (2.14) and write an equation for SO_2^i only. Moreover, by the Henry law [66], the partial pressure of Oxygen is given by

$$\text{PO}_2^i = \alpha[\text{O}_2]^i, \quad (2.20)$$

where α [$\text{mmHg m}^3 \text{ mol}^{-1}$] is the Henry law's constant. Hence we get $[\text{O}_2]^i = \alpha^{-1} \text{PO}_2^i$, and by (2.18)–(2.19) considering $[\text{Hb*}]$ constant, we can write the equations for $i = 1, 2, 3$ and the total amount of oxygen delivered to the muscle using SO_2^i and PO_2^i as primary variables. The equations read

$$\left\{ \begin{array}{l} \frac{\partial}{\partial t} \text{PO}_2^i + \psi_i^{-1} \nabla \cdot (\text{PO}_2^i \mathbf{u}_i) + \mu\Delta \text{PO}_2^i = n\alpha[\text{Hb*}] (k_- \text{SO}_2^i - k_+ \alpha^{-n} (1 - \text{SO}_2^i) (\text{PO}_2^i)^n) \\ \qquad \qquad \qquad + \psi_i^{-1} \widehat{\phi}_{i-1,i} \text{PO}_2^{i-1} - \psi_i^{-1} \widehat{\phi}_{i,i+1} \text{PO}_2^i \\ \qquad \qquad \qquad - \psi_i^{-1} \frac{A_v^i}{V_t} P (\text{PO}_2^i - \text{PO}_2^m) \delta_{i3}, \end{array} \right. \quad (2.21a)$$

$$\left. \begin{array}{l} \frac{\partial}{\partial t} \text{SO}_2^i + \psi_i^{-1} \nabla \cdot (\text{SO}_2^i \mathbf{u}_i) + \mu\Delta \text{SO}_2^i = - (k_- \text{SO}_2^i - k_+ \alpha^{-n} (1 - \text{SO}_2^i) (\text{PO}_2^i)^n) \\ \qquad \qquad \qquad + \psi_i^{-1} \widehat{\phi}_{i-1,i} \text{SO}_2^{i-1} - \psi_i^{-1} \widehat{\phi}_{i,i+1} \text{SO}_2^i, \end{array} \right. \quad (2.21b)$$

$$\lambda_{\text{O}_2}^{\text{del}}(t) = \frac{1}{|\Omega_M|} \int_{\Omega_M} \alpha^{-1} \frac{A_v^3}{V_t} P (\text{PO}_2^3 - \text{PO}_2^m) d\mathbf{x}, \quad \Lambda_{\text{O}_2}^{\text{del}}(t) = \int_0^t \lambda_{\text{O}_2}^{\text{del}}(u) du. \quad (2.22)$$

2.3.4. Oxygen dynamics inside the muscle

So far, we have considered the oxygen concentration in the muscle $[O_2]^m$ and the corresponding partial pressure $PO_2^m = \alpha [O_2]^m$ as a datum. In this section, we derive an equation to model its dynamics. Similarly to (2.14), we have

$$\frac{d}{dt} \int_V [O_2]^m \psi_m \, d\mathbf{x} = \int_V \frac{A_v^3}{V_t} P([O_2]^3 - [O_2]^m) \, d\mathbf{x} - \int_V \psi_m \xi \, d\mathbf{x}, \quad (2.23)$$

where ξ [$\text{mol m}^{-3} \text{s}^{-1}$] is the oxygen consumption rate per unit volume of muscle of the metabolic activity. For the latter term, we adopt the Michaelis-Menten dynamics [60]

$$\xi = \xi_0 \left(1 + \frac{PO_2^{m,50}}{PO_2^m} \right)^{-1}, \quad (2.24)$$

where ξ_0 [$\text{mol m}^{-3} \text{s}^{-1}$] is the maximum oxygen consumption rate and $PO_2^{m,50}$ [mmHg] is the half maximal effective partial pressure.

We multiply (2.23) by $\alpha \psi_m^{-1}$ and, since V is arbitrary, we get

$$\frac{\partial}{\partial t} PO_2^m = \psi_m^{-1} \frac{A_v^3}{V_t} P(PO_2^3 - PO_2^m) - \alpha \xi_0 \left(1 + \frac{PO_2^{m,50}}{PO_2^m} \right)^{-1}. \quad (2.25)$$

As previously, we are also interested in the average amount of oxygen consumed by the muscle defined by $\lambda_{O_2}^{\text{cons}}$ [mol m^{-3}], which is computable as

$$\lambda_{O_2}^{\text{cons}}(t) = \frac{1}{|\Omega_M|} \int_{\Omega_M} \psi_m \xi_0 \left(1 + \frac{PO_2^{m,50}}{PO_2^m} \right)^{-1} \, d\mathbf{x}, \quad (2.26)$$

and on total amount of oxygen consumed by the muscle defined by $\Lambda_{O_2}^{\text{cons}}$ [$\text{mol m}^{-3} \text{s}^{-1}$], which is computable integrating the latter in the time interval $[0, t]$, namely

$$\Lambda_{O_2}^{\text{cons}}(t) = \int_0^t \lambda_{O_2}^{\text{cons}}(u) \, du. \quad (2.27)$$

Hence, the model up to now is

$$\left\{ \begin{array}{l} \frac{\partial}{\partial t} \text{PO}_2^i + \psi_i^{-1} \nabla \cdot (\text{PO}_2^i \mathbf{u}_i) + \mu \Delta \text{PO}_2^i = n\alpha[\text{Hb}*] (k_- \text{SO}_2^i - k_+ \alpha^{-n} (1 - \text{SO}_2^i) (\text{PO}_2^i)^n) \\ \quad + \psi_i^{-1} \hat{\phi}_{i-1,i} \text{PO}_2^{i-1} - \psi_i^{-1} \hat{\phi}_{i,i+1} \text{PO}_2^i \\ \quad - \psi_i^{-1} \frac{A_v^i}{V_t} P (\text{PO}_2^i - \text{PO}_2^m) \delta_{i3}, \end{array} \right. \quad (2.28a)$$

$$\left\{ \begin{array}{l} \frac{\partial}{\partial t} \text{SO}_2^i + \psi_i^{-1} \nabla \cdot (\text{SO}_2^i \mathbf{u}_i) + \mu \Delta \text{SO}_2^i = -(k_- \text{SO}_2^i - k_+ \alpha^{-n} (1 - \text{SO}_2^i) (\text{PO}_2^i)^n) \\ \quad + \psi_i^{-1} \hat{\phi}_{i-1,i} \text{SO}_2^{i-1} - \psi_i^{-1} \hat{\phi}_{i,i+1} \text{SO}_2^i \end{array} \right. \quad (2.28b)$$

$$\left. \frac{\partial}{\partial t} \text{PO}_2^m = \psi_m^{-1} \frac{A_v^3}{V_t} P (\text{PO}_2^3 - \text{PO}_2^m) - \alpha \xi_0 \left(1 + \frac{\text{PO}_2^{m,50}}{\text{PO}_2^m} \right)^{-1}, \quad (2.28c) \right.$$

$$\lambda_{\text{O}_2}^{\text{del}}(t) = \frac{1}{|\Omega_M|} \int_{\Omega_M} \alpha^{-1} \frac{A_v^3}{V_t} P (\text{PO}_2^3 - \text{PO}_2^m) \, d\mathbf{x}, \quad \Lambda_{\text{O}_2}^{\text{del}}(t) = \int_0^t \lambda_{\text{O}_2}^{\text{del}}(u) \, du, \quad (2.29a)$$

$$\lambda_{\text{O}_2}^{\text{cons}}(t) = \frac{1}{|\Omega_M|} \int_{\Omega_M} \psi_m \xi_0 \left(1 + \frac{\text{PO}_2^{m,50}}{\text{PO}_2^m} \right)^{-1} \, d\mathbf{x}, \quad \Lambda_{\text{O}_2}^{\text{cons}}(t) = \int_0^t \lambda_{\text{O}_2}^{\text{cons}}(u) \, du. \quad (2.29b)$$

2.3.5. Parameters calibration

In the model (2.21)–(2.29), PO_2^m should be regarded as a datum, as it is associated with the level of physical activity of the patient which is $\text{PO}_2^m \simeq 40$ mmHg at rest and $\text{PO}_2^m \simeq 20$ mmHg during exercise [51].

We assume the chemical reactions to be in equilibrium in compartment $i = a$, that is

$$k_- \text{SO}_2^i - k_+ \alpha^{-n} (1 - \text{SO}_2^i) (\text{PO}_2^i)^n = 0,$$

which corresponds to the Hill equation [35]

$$\text{SO}_2^i = \frac{(\text{PO}_2^i)^n}{(\text{PO}_2^i)^n + (\text{PO}_2^{50})^n} = \left(1 + \left(\frac{\text{PO}_2^{50}}{\text{PO}_2^i} \right)^n \right)^{-1}, \quad (2.30)$$

where $\text{PO}_2^{50} = \alpha (k_- / k_+)^{1/n}$ [mmHg] is the half-maximal effective oxygen partial pressure, namely the partial oxygen pressure in the capillaries we have when oxygen saturation is 50%. The value of PO_2^{50} is an indicator of the affinity between oxygen and hemoglobin: the higher is PO_2^{50} , the higher is the capacity of hemoglobin to bind oxygen.

In the following, we will assume that the oxygen partial pressure PO_2^a is a given datum (constant in time) and that the oxygen saturation SO_2^a is given by (2.30).

It is possible to prove that, in the compartments $i = 1, 2$, saturation and partial oxygen pressure do not change with respect to arterial blood: indeed, by setting $\text{SO}_2^2 = \text{SO}_2^1 = \text{SO}_2^a$ and $\text{PO}_2^2 = \text{PO}_2^1 = \text{PO}_2^a$ into (2.28), the equations are satisfied thanks to (2.10). Therefore, we can focus on the third compartment only, and from now on, we will write the model for $i = 3$ explicitly.

The Hill equation (2.30) allows us to calibrate from the experimentally measured oxygen-hemoglobin dissociation curve the exponent n and PO_2^{50} . Hence, for the dynamics of SO_2 , the only parameter left to be calibrated is k_- . Since the association-dissociation reaction between hemoglobin and oxygen is swift (it could be considered quasistatic), this could be very large without significantly affecting the solution.

Concerning the dynamics of PO_2 , we need to calibrate the following terms.

- α , which is available in the literature;
- $[\text{Hb}*]$, which is available in the literature;
- the product $\frac{A_v^i}{V_t} P$ for $i = 1, 2, 3$, which can be found in the literature or, alternatively, it can be phenomenologically calibrated;
- the terms ψ_i for $i = 1, 2, 3, m$;
- the terms $\alpha\xi_0$ and $\text{PO}_2^{m,50}$, ruling oxygen consumption by the muscle.

Hence, to reduce the number of parameters to be calibrated, we denote the product $\tilde{P} := \frac{A_v^i}{V_t} P$ as the effective permeability [s^{-1}], and the product $\tilde{\xi}_0 = \alpha\xi_0$ as the effective oxygen consumption rate [mmHg s^{-1}].

Variable	Measure unit	Value
n	—	3.2
PO_2^m	mmHg	40
PO_2^{50}	mmHg	26.7
α	$\text{mmHg m}^3 \text{ mol}^{-1}$	722.6
$[\text{Hb}*]$	mol m^{-3}	10
k_-	s^{-1}	100
\tilde{P}	s^{-1}	1
$\tilde{\xi}_0$	mmHg s^{-1}	50
$\text{PO}_2^{m,50}$	mmHg	40
ψ_1, ψ_2, ψ_3	—	$3 \cdot 10^{-3}$
μ	$\text{m}^2 \text{s}^{-1}$	0.1

Table 2.3: List of oxygenation model parameters.

In this manner, model (2.28)–(2.25) can be rewritten as

$$\left\{ \begin{array}{l} \frac{\partial}{\partial t} \text{PO}_2^3 + \psi_3^{-1} \nabla \cdot (\text{PO}_2^3 \mathbf{u}_3) + \mu \Delta \text{PO}_2^3 = n \alpha [\text{Hb}*] k_- \left(\text{SO}_2^3 - (1 - \text{SO}_2^3) \left(\frac{\text{PO}_2^3}{\text{PO}_2^{50}} \right)^n \right) \\ \quad + \psi_3^{-1} \hat{\phi}_{2,3} \text{PO}_2^a - \psi_3^{-1} \hat{\phi}_{3,\text{veins}} \text{PO}_2^3 \\ \quad - \psi_3^{-1} \tilde{P} (\text{PO}_2^3 - \text{PO}_2^m) \end{array} \right. \quad (2.31a)$$

$$\left\{ \begin{array}{l} \frac{\partial}{\partial t} \text{SO}_2^3 + \psi_3^{-1} \nabla \cdot (\text{SO}_2^3 \mathbf{u}_3) + \mu \Delta \text{SO}_2^3 = -k_- \left(\text{SO}_2^3 - (1 - \text{SO}_2^3) \left(\frac{\text{PO}_2^3}{\text{PO}_2^{50}} \right)^n \right) \\ \quad + \psi_3^{-1} \hat{\phi}_{2,3} \text{SO}_2^a - \psi_3^{-1} \hat{\phi}_{3,\text{veins}} \text{SO}_2^3 \end{array} \right. \quad (2.31b)$$

$$\left. \frac{\partial}{\partial t} \text{PO}_2^m = \psi_m^{-1} \tilde{P} (\text{PO}_2^3 - \text{PO}_2^m) - \tilde{\xi}_0 \left(1 + \frac{\text{PO}_2^{m,50}}{\text{PO}_2^m} \right)^{-1} \right. \quad (2.31c)$$

$$\lambda_{\text{O}_2}^{\text{del}}(t) = \frac{1}{|\Omega_M|} \int_{\Omega_M} \tilde{P} \alpha^{-1} (\text{PO}_2^3 - \text{PO}_2^m) \, d\mathbf{x}, \quad \Lambda_{\text{O}_2}^{\text{del}}(t) = \int_0^t \lambda_{\text{O}_2}^{\text{del}}(u) \, du, \quad (2.32a)$$

$$\lambda_{\text{O}_2}^{\text{cons}}(t) = \frac{1}{|\Omega_M|} \int_{\Omega_M} \psi_m \tilde{\xi}_0 \alpha^{-1} \left(1 + \frac{\text{PO}_2^{m,50}}{\text{PO}_2^m} \right)^{-1} \, d\mathbf{x}, \quad \Lambda_{\text{O}_2}^{\text{cons}}(t) = \int_0^t \lambda_{\text{O}_2}^{\text{cons}}(u) \, du. \quad (2.32b)$$

The values of the parameters characterizing the equations in a physiological scenario are provided in [51] or calibrated by experimental measures, except for μ , which is arbitrarily set to $0.1 \text{ m}^2 \text{s}^{-1}$. All the values of the parameters are listed in Table 2.3.

The vector field \mathbf{u}_3 and the scalar fields $\hat{\phi}_{2,3}$ and $\hat{\phi}_{3,\text{veins}}$ are responsible for the coupling with fluid and perfusion problems as we discuss their values in Section 2.4.2. However, as shown in the final part of this work, it can be useful to simulate only the oxygenation model without the fluid and perfusion ones in the same cases. In these cases, suitable

Variable	Measure unit	Value
Φ_M	s^{-1}	0.021
T_{HB}	s	0.8

Table 2.4: List of oxygenation model parameters for the uncoupled case.

values of these fields must be provided to describe the blood velocity and inward/outward flux. For these scenarios, we adopt $\mathbf{u}_3 = \mathbf{0}$, namely we neglect the effect of advection. On the other hand, regarding the blood fluxes, we use the spatially homogeneous scalar fields fields

$$\hat{\phi}_{2,3}(\mathbf{x}, t) \equiv \hat{\phi}_{3,\text{veins}}(\mathbf{x}, t) = \frac{\Phi_M}{2} \left(1 - \cos \left(\frac{2\pi}{T_{HB}} t \right) \right), \quad (2.33)$$

where Φ_M [s^{-1}] is the flux magnitude and T_{HB} [s] is the heartbeat period. With this choice, we simulate a sinusoidal blood flux similar to the real one. Suitable physiological values for these parameters are in Table 2.4.

By choosing this parameters, we obtain $\bar{\Psi}_{CBF} = 0.63 \text{ mL min}^{-1} \text{ g}^{-1}$ which is in good accordance with the value found in literature we discussed in Section 2.3.2.

2.3.6. Quasistatic-chemistry approximation

As each attached hemoglobin stores n molecules of oxygen, the concentration of oxygen stored in red blood cells inside the third compartment is given by $n[\text{HbO}_2] = n[\text{Hb}*] \text{ SO}_2^3$. Conversely, the concentration of free oxygen is given by $[\text{O}_2*] = \alpha^{-1} \text{ PO}_2^3$. Hence, we define the total oxygen concentration as

$$[\text{O}_2]^3 = n[\text{Hb}*] \text{ SO}_2^3 + \alpha^{-1} \text{ PO}_2^3. \quad (2.34)$$

An approximation of model (2.21)–(2.25) can be obtained by assuming that the chemical reaction between oxygen and hemoglobin is much faster than the other phenomena, so that it can be considered at equilibrium. In this case, by the Hill equation, the total oxygen concentration in the third compartment is given by

$$[\text{O}_2]^3 = n[\text{Hb}*] \left(1 + \left(\frac{\text{PO}_2^{50}}{\text{PO}_2^3} \right)^n \right)^{-1} + \alpha^{-1} \text{ PO}_2^3 =: g(\text{PO}_2^3). \quad (2.35)$$

Hence, the model (we will refer to as to the reduced model in the following) can be reduced to a couple of equations as

$$\left\{ \begin{array}{l} \frac{\partial}{\partial t} [\text{O}_2*]^3 + \psi_3^{-1} \nabla \cdot ([\text{O}_2*]^3 \mathbf{u}_3) + \mu \Delta [\text{O}_2*]^3 = \psi_3^{-1} \hat{\phi}_{2,3} [\text{O}_2*]^2 - \psi_3^{-1} \hat{\phi}_{3,\text{veins}} [\text{O}_2*]^3 \\ \quad - \psi_3^{-1} \tilde{P} \alpha^{-1} (g^{-1}([\text{O}_2*]^3) - \text{PO}_2^m), \end{array} \right. \quad (2.36a)$$

$$\left\{ \begin{array}{l} \frac{\partial}{\partial t} \text{PO}_2^m = \psi_m^{-1} \tilde{P} (g^{-1}([\text{O}_2*]^3) - \text{PO}_2^m) \\ \quad - \tilde{\xi}_0 \left(1 + \frac{\text{PO}_2^{m,50}}{\text{PO}_2^m} \right)^{-1}, \end{array} \right. \quad (2.36b)$$

$$\lambda_{\text{O}_2}^{\text{del}}(t) = \frac{1}{|\Omega_M|} \int_{\Omega_M} \tilde{P} \alpha^{-1} (g^{-1}([\text{O}_2*]^3) - \text{PO}_2^m) \, d\mathbf{x}, \quad \Lambda_{\text{O}_2}^{\text{del}}(t) = \int_0^t \lambda_{\text{O}_2}^{\text{del}}(u) \, du, \quad (2.37a)$$

$$\lambda_{\text{O}_2}^{\text{cons}}(t) = \frac{1}{|\Omega_M|} \int_{\Omega_M} \psi_m \tilde{\xi}_0 \alpha^{-1} \left(1 + \frac{\text{PO}_2^{m,50}}{\text{PO}_2^m} \right)^{-1} \, d\mathbf{x}, \quad \Lambda_{\text{O}_2}^{\text{cons}}(t) = \int_0^t \lambda_{\text{O}_2}^{\text{cons}}(u) \, du. \quad (2.37b)$$

We will see in Section 4.2.1 that the quasistatic-chemistry approximation is appropriate and computationally cheaper to use. Hence, from now on, we will only consider this formulation of the model.

Notice that also with this reduced model is possible to reconstruct a-posteriori the scalar fields SO_2 , PO_2 thanks to (2.35) and to (2.30). On the other hand, using the complete model is possible to reconstruct a-posteriori the scalar field $[\text{O}_2*]$ to (2.35). Hence, in each case study, we will focus on all the scalar fields PO_2 , PO_2^m , SO_2 and $[\text{O}_2*]$, both with the oxygen fluxes $\lambda_{\text{O}_2}^{\text{del}}$, $\lambda_{\text{O}_2}^{\text{cons}}$ and $\Lambda_{\text{O}_2}^{\text{del}}$, $\Lambda_{\text{O}_2}^{\text{cons}}$.

2.4. Coupling conditions

In this section, we close the mathematical problems for blood dynamics introduced in Section 2.1 for epicardial coronary arteries and Section 2.2 for intramural vessels by providing the coupling conditions between the epicardial and the intramural hemodynamics. Finally, we present the conditions to couple with the oxygenation model and we show the complete mathematical formulation of the multi-physics problem.

The coupling between the three models is summarized in Figure 2.3: we simulate the blood fluid dynamics in the coronaries coupled with the blood perfusion in the myocardium as a porous medium to simulate the capillary network, and finally we use the perfusion output as input of the oxygenation model to compute the desired quantities.

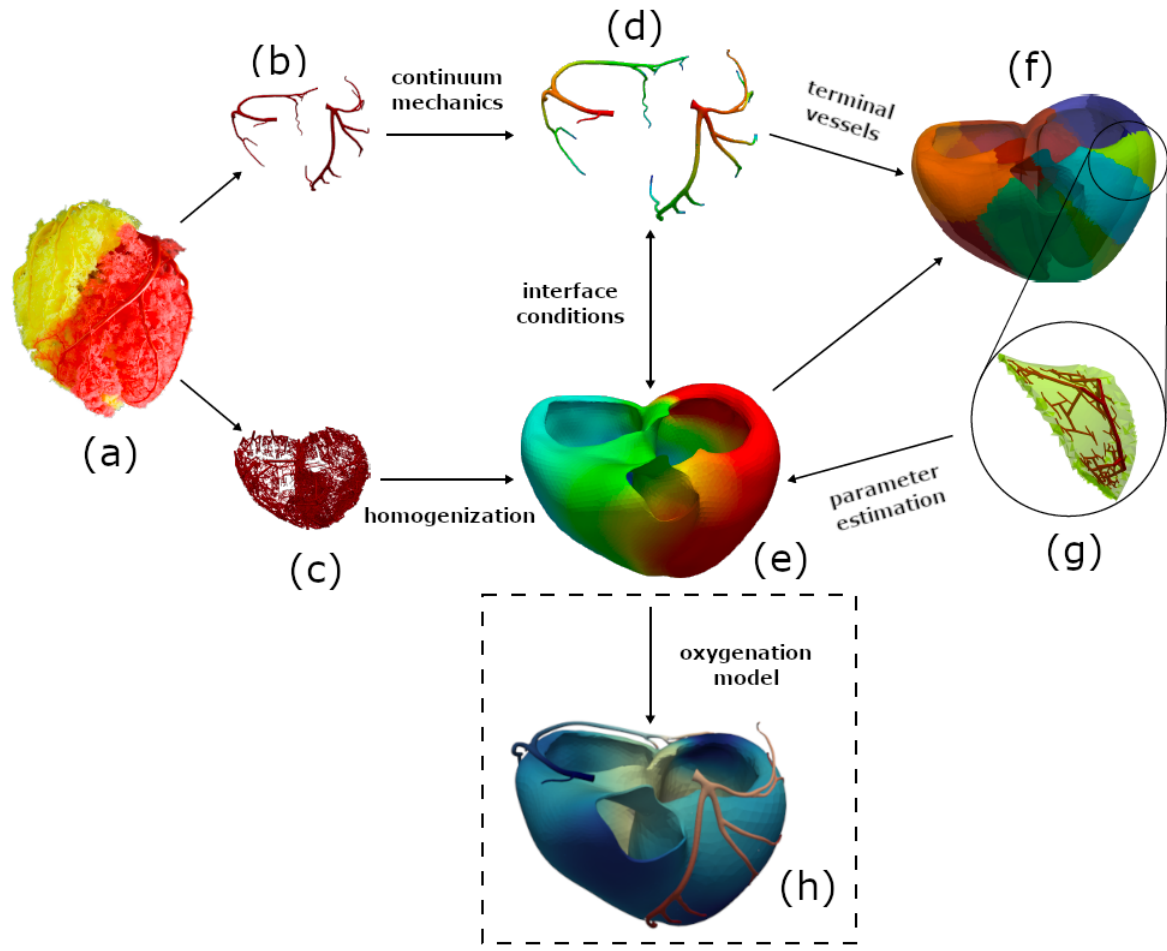


Figure 2.3: (a) Cast of Coronary Arteries, source Wikipedia; (b) epicardial coronary arteries; (c) intramural coronary vessels; (d) 3D blood flow dynamics model inside coronary domain (pressure depicted); (e) porous media flow model inside myocardial domain (pressure depicted); (f) myocardium partitioned into different perfusion regions; (g) example of generated intramural vascular network inside a perfusion region; (h) oxygenation model in capillaries (capillaries $[O_2^*]$ depicted).

2.4.1. Fluid dynamics and perfusion

In order to couple the problem related to the blood dynamics in epicardial coronary arteries and the problem for the intramural vessels description, we need two coupling conditions, one ensuring the conservation of mass and another for the balance of interface forces (third Newton law).

We assume that there is a one-to-one correspondence between outlets of epicardial coronary arteries and perfusion regions $\Omega_M^j, j = 1, \dots, J$, where the exchange of information between epicardial coronary arteries and intramural vessels occurs.

The coupling conditions between Navier-Stokes equations and the multi-compartment Darcy model are the following.

- *Conservation of mass.* The first compartment in the multi-compartment Darcy model (the most upstream one) exchanges mass with the epicardial coronary outflows Γ^j . Thus, the volumetric source g_1 should be provided by the outgoing coronary flow rate

$$g_1(\mathbf{x}) = \sum_{j=1}^J \frac{\chi_{\Omega_M^j}(\mathbf{x})}{|\Omega_M^j|} \int_{\Gamma^j} \mathbf{u}_C \cdot \mathbf{n} \, d\gamma, \quad (2.38)$$

where the notation χ_V stands for the characteristic function of the domain V .

- *Balance of interface forces.* Due to the heterogeneity of the two models and the distributed nature of the Darcy model, we expect to have a pressure jump at the interface Γ^j , which induces the following epicardial coronary flow rate [118]

$$\int_{\Gamma^j} \mathbf{u}_C \cdot \mathbf{n} \, d\gamma = \alpha^j \left(\frac{1}{|\Gamma^j|} \int_{\Gamma^j} p_C(\mathbf{x}) \, d\gamma - \frac{1}{|\Omega_M^j|} \int_{\Omega_M^j} p_1(\mathbf{x}) \, d\mathbf{x} \right), \quad (2.39)$$

for $j = 1, \dots, J$, where \mathbf{n} is the unit outer normal vector and α^j [$\text{m}^3 \text{s}^{-1} \text{mmHg}^{-1}$] is the conductance parameters between epicardial coronary arteries and the porous medium, supposed to be dependent on the perfusion region. Physiological values of α^j are listed in Table 2.5. Notice that only the first compartment is involved in the coupling condition.

The previous condition is defective since it involves average quantities [29, 88, 117]. We, therefore, reformulate it into the following mixed pointwise/defective Robin condition, which guarantees enough boundary information for the normal component

$$\begin{aligned} -p_C + \mu \left(\nabla \mathbf{u}_C + (\nabla \mathbf{u}_C)^T \right) \mathbf{n} \cdot \mathbf{n} + \frac{1}{\alpha^j} \int_{\Gamma^j} \mathbf{u}_C \cdot \mathbf{n} \, d\gamma = \\ -\frac{1}{|\Omega_M^j|} \int_{\Omega_M^j} p_1(\mathbf{x}) \, d\mathbf{x} \quad \text{on } \Gamma^j, \end{aligned} \quad (2.40)$$

where we have assumed a constant coronary normal traction over the section Γ^j .

As a second-order PDE, the epicardial problem also needs a condition for the tangential components. Here, we assume that tangential tractions are null, namely that

$$\mu \left(\nabla \mathbf{u}_C + (\nabla \mathbf{u}_C)^T \right) \mathbf{n} \cdot \boldsymbol{\tau}_i = 0, \quad i = 1, 2 \quad \text{on } \Gamma^j, \quad (2.41)$$

where $\boldsymbol{\tau}_i$ are the two tangential unit vectors.

Variable	Measure unit	Value
α^1	$\text{m}^3 \text{s}^{-1} \text{mmHg}^{-1}$	$3.50 \cdot 10^{-13}$
α^2	$\text{m}^3 \text{s}^{-1} \text{mmHg}^{-1}$	$8.08 \cdot 10^{-13}$
α^3	$\text{m}^3 \text{s}^{-1} \text{mmHg}^{-1}$	$2.37 \cdot 10^{-12}$
α^4	$\text{m}^3 \text{s}^{-1} \text{mmHg}^{-1}$	$9.59 \cdot 10^{-13}$
α^5	$\text{m}^3 \text{s}^{-1} \text{mmHg}^{-1}$	$1.23 \cdot 10^{-12}$
α^6	$\text{m}^3 \text{s}^{-1} \text{mmHg}^{-1}$	$3.36 \cdot 10^{-12}$
α^7	$\text{m}^3 \text{s}^{-1} \text{mmHg}^{-1}$	$1.67 \cdot 10^{-12}$
α^8	$\text{m}^3 \text{s}^{-1} \text{mmHg}^{-1}$	$1.92 \cdot 10^{-12}$
α^9	$\text{m}^3 \text{s}^{-1} \text{mmHg}^{-1}$	$3.69 \cdot 10^{-13}$
α^{10}	$\text{m}^3 \text{s}^{-1} \text{mmHg}^{-1}$	$9.32 \cdot 10^{-13}$
α^{11}	$\text{m}^3 \text{s}^{-1} \text{mmHg}^{-1}$	$5.43 \cdot 10^{-13}$
α^{12}	$\text{m}^3 \text{s}^{-1} \text{mmHg}^{-1}$	$1.57 \cdot 10^{-13}$
α^{13}	$\text{m}^3 \text{s}^{-1} \text{mmHg}^{-1}$	$6.18 \cdot 10^{-13}$
α^{14}	$\text{m}^3 \text{s}^{-1} \text{mmHg}^{-1}$	$6.64 \cdot 10^{-13}$
α^{15}	$\text{m}^3 \text{s}^{-1} \text{mmHg}^{-1}$	$4.14 \cdot 10^{-13}$
α^{16}	$\text{m}^3 \text{s}^{-1} \text{mmHg}^{-1}$	$1.77 \cdot 10^{-12}$
α^{17}	$\text{m}^3 \text{s}^{-1} \text{mmHg}^{-1}$	$8.42 \cdot 10^{-13}$

Table 2.5: List of α^j parameters for each perfusion region j .

2.4.2. Oxygenation and perfusion

To couple the oxygenation model with the three-compartments Darcy model, we need to leverage on the Darcy law to set the fields \mathbf{u}_3 , $\hat{\phi}_{2,3}$, and $\hat{\phi}_{3,\text{veins}}$ properly. As already described, the velocity field \mathbf{u}_3 can be reconstructed as

$$\mathbf{u}_3 = -\mathbf{K}_3 \nabla p_3. \quad (2.42)$$

Moreover, the inward flux $\hat{\phi}_{2,3}$ between the second and third compartment and the outward flux $\hat{\phi}_{3,\text{veins}}$ from the the third compartment to the venous system can be computed as

$$\hat{\phi}_{2,3} = \beta_{2,3}(p_3 - p_2), \quad (2.43)$$

and

$$\hat{\phi}_{3,\text{veins}} = \gamma(p_3 - p_{\text{veins}}), \quad (2.44)$$

respectively.

The details about the parameters involved were discussed in Section 2.2.

2.4.3. Multi-physics oxygenation problem

By means of (2.42)–(2.43)–(2.44), the oxygenation problem is the following.

Problem 2.1. Three-compartments multi-physics oxygenation problem.

Given $\rho, \mu_C, \mu, \alpha^j, \beta_{1,2}, \beta_{2,3}, \mathbf{K}_{i,j}, \gamma, p_{\text{veins}}, \alpha, \psi_3, \text{PO}_2^{m,50}, \tilde{P}$ and $\tilde{\xi}_0$,

find $\mathbf{u}_i, p_i, \mathbf{u}_C, p_C, i = 1, 2, 3$ and $[\text{O}_2*]^3, \text{PO}_2^m$ such that

$$\left. \begin{aligned} & \rho \left(\frac{\partial \mathbf{u}_C}{\partial t} + (\mathbf{u}_C \cdot \nabla) \mathbf{u}_C \right) - \mu_C \nabla \cdot (\nabla \mathbf{u}_C + (\nabla \mathbf{u}_C)^T) + \nabla p_C = \mathbf{0} \text{ in } \Omega_C, \\ & \nabla \cdot \mathbf{u}_C = 0 \text{ in } \Omega_C, \end{aligned} \right\} \quad (2.45a)$$

$$\left. \begin{aligned} & p_C - \mu_C (\nabla \mathbf{u}_C + (\nabla \mathbf{u}_C)^T) \mathbf{n} \cdot \mathbf{n} - \frac{1}{\alpha^j} \int_{\Gamma^j} \mathbf{u}_C \cdot \mathbf{n} \, d\gamma = \frac{1}{|\Omega_M^j|} \int_{\Omega_M^j} p_1 \, d\mathbf{x} \text{ on } \Gamma^j, \\ & \mu_C (\nabla \mathbf{u}_C + (\nabla \mathbf{u}_C)^T) \mathbf{n} \cdot \boldsymbol{\tau}_i = 0, \quad i = 1, 2 \text{ on } \Gamma^j, \end{aligned} \right\} \quad (2.45c)$$

$$\left. \begin{aligned} & \mathbf{u}_1 + \mathbf{K}_1 \nabla p_1 = \mathbf{0} \text{ in } \Omega_M, \\ & \nabla \cdot \mathbf{u}_1 = \sum_{j=1}^J \frac{\chi_{\Omega_M^j}}{|\Omega_M^j|} \int_{\Gamma^j} \mathbf{u}_C \cdot \mathbf{n} \, d\gamma - \beta_{1,2} (p_1 - p_2) \text{ in } \Omega_M, \end{aligned} \right\} \quad (2.45e)$$

$$\left. \begin{aligned} & \mathbf{u}_2 + \mathbf{K}_2 \nabla p_2 = \mathbf{0} \text{ in } \Omega_M, \\ & \nabla \cdot \mathbf{u}_2 = -\beta_{2,1} (p_2 - p_1) - \beta_{2,3} (p_2 - p_3) \text{ in } \Omega_M, \end{aligned} \right\} \quad (2.45g)$$

$$\left. \begin{aligned} & \mathbf{u}_3 + \mathbf{K}_3 \nabla p_3 = \mathbf{0} \text{ in } \Omega_M, \\ & \nabla \cdot \mathbf{u}_3 = -\gamma (p_3 - p_{\text{veins}}) - \beta_{3,2} (p_3 - p_2) \text{ in } \Omega_M, \end{aligned} \right\} \quad (2.45i)$$

$$\left. \begin{aligned} & \mathbf{u}_i \cdot \mathbf{n} = 0, \quad i = 1, 2, 3 \text{ on } \partial \Omega_M, \\ & \frac{\partial}{\partial t} [\text{O}_2*]^3 + \psi_3^{-1} \nabla \cdot (-\mathbf{K}_3 [\text{O}_2*]^3 \nabla p_3) + \mu \Delta [\text{O}_2*]^3 = \end{aligned} \right\} \quad (2.45l)$$

$$\left. \begin{aligned} & \psi_3^{-1} \beta_{2,3} (p_3 - p_2) [\text{O}_2*]^2 - \psi_3^{-1} \gamma (p_3 - p_{\text{veins}}) [\text{O}_2*]^3 \\ & - \psi_3^{-1} \tilde{P} \alpha^{-1} (g^{-1}([\text{O}_2*]^3) - \text{PO}_2^m) \text{ in } \Omega_M, \end{aligned} \right\} \quad (2.45m)$$

$$\left. \begin{aligned} & \frac{\partial}{\partial t} \text{PO}_2^m = \psi_m^{-1} \tilde{P} (g^{-1}([\text{O}_2*]^3) - \text{PO}_2^m) - \tilde{\xi}_0 \left(1 + \frac{\text{PO}_2^{m,50}}{\text{PO}_2^m} \right)^{-1} \text{ in } \Omega_M, \end{aligned} \right\} \quad (2.45o)$$

reconstruct PO_2^3 and SO_2^3 by

$$[\text{O}_2*]^3 = n[\text{Hb}*] \left(1 + \left(\frac{\text{PO}_2^{50}}{\text{PO}_2^3} \right)^n \right)^{-1} + \alpha^{-1} \text{PO}_2^3 =: g(\text{PO}_2^3), \quad \text{SO}_2^i = \left(1 + \left(\frac{\text{PO}_2^{50}}{\text{PO}_2^i} \right)^n \right)^{-1},$$

and compute

$$\lambda_{\text{O}_2}^{\text{del}}(t) = \frac{1}{|\Omega_M|} \int_{\Omega_M} \tilde{P} \alpha^{-1} (g^{-1}([\text{O}_2*]^3) - \text{PO}_2^m) \, d\mathbf{x}, \quad \Lambda_{\text{O}_2}^{\text{del}}(t) = \int_0^t \lambda_{\text{O}_2}^{\text{del}}(u) \, du,$$

$$\lambda_{\text{O}_2}^{\text{cons}}(t) = \frac{1}{|\Omega_M|} \int_{\Omega_M} \psi_m \tilde{\xi}_0 \alpha^{-1} \left(1 + \frac{\text{PO}_2^{m,50}}{\text{PO}_2^m} \right)^{-1} \, d\mathbf{x}, \quad \Lambda_{\text{O}_2}^{\text{cons}}(t) = \int_0^t \lambda_{\text{O}_2}^{\text{cons}}(u) \, du.$$

3 | Numerical schemes

In this chapter, we describe the numerical schemes employed to solve the Problem 2.1. The implementation of the multi-physics model was made inside the `lifex` [1, 125], a C++ high-performance finite element library (based on `deal.II` framework [5]) focused on mathematical models and numerical methods for cardiac applications. We leveraged to already provided implementation of the fluid dynamics and perfusion models, implementing the oxygenation one and the coupling conditions.

For the subproblems regarding fluid dynamics and perfusion, we use the FEM for spatial discretization and the FDM for time discretization. In particular, for the fluid problem, we used a backward differentiation formula of the first order, and we treated the convective term in a semi-implicit way [90]. We have available and employ meshes with tetrahedral or hexahedral elements for the fluid and hexahedral ones for the Darcy model, as for spatial discretization, we consider P_1/P_1 finite elements in test with tetrahedral meshes (or Q_1/Q_1 finite elements in hexahedral meshes) with a SUPG-SUPG stabilization [28, 30, 111, 112]. Regarding the multi-compartment Darcy model, we used hexahedral meshes and P_1 finite elements. Finally, for an effective numerical solution of the coupled problem, we adopted and show in Section 2.4.1 an iterative splitting strategy [25].

Regarding the oxygenation model, we can find in this chapter

- the weak formulation of the problem in Section 3.1;
- the Galerkin formulation for space discretization in Section 3.2;
- the fully discretized problem in Section 3.3;
- the algebraic formulation for the FEM in Section 3.4.

In Section 3.5 and 3.6, we can find the treatment of the 0D model and averaged quantities: in particular, in the former is proposed a Runge-Kutta method to solve the 0D model, and in the latter, a trapezoidal formula to compute the integral in time of the oxygen fluxes. Finally, in Section 3.7.2, we explained the strategy used to couple the oxygenation model with the others.

3.1. Weak formulation

We define the spaces

$$V, W = L_2([0, T], H^1(\Omega_M)),$$

so that, since $[O_2*]$ and PO_2^m are sufficiently regular in space and time, we can assume they belong to $[O_2*] \in V$ and $PO_2^m \in W$.

To obtain the weak formulation, we multiply the equations by a generic test functions $v \in V$ and $w \in W$, and we integrate over the whole domain Ω_M , providing

$$\left\{ \begin{array}{l} \int_{\Omega_M} \frac{\partial}{\partial t} [O_2*]^3 v \, d\mathbf{x} + \\ + \int_{\Omega_M} \psi_3^{-1} \nabla \cdot ([O_2*]^3 \mathbf{u}_3) v \, d\mathbf{x} + \int_{\Omega_M} \mu \Delta [O_2*]^3 v \, d\mathbf{x} = \int_{\Omega_M} \psi_3^{-1} \hat{\phi}_{2,3} [O_2*]^2 v \, d\mathbf{x} \\ - \int_{\Omega_M} \psi_3^{-1} \hat{\phi}_{3,\text{veins}} [O_2*]^3 v \, d\mathbf{x} \\ - \int_{\Omega_M} \psi_3^{-1} \tilde{P} \alpha^{-1} (g^{-1}([O_2*]^3) - PO_2^m) v \, d\mathbf{x}, \\ \int_{\Omega_M} \frac{\partial}{\partial t} PO_2^m w \, d\mathbf{x} = \int_{\Omega_M} \psi_m^{-1} \tilde{P} (g^{-1}([O_2*]^3) - PO_2^m) w \, d\mathbf{x} \\ - \int_{\Omega_M} \tilde{\xi}_0 \left(1 + \frac{PO_2^{m,50}}{PO_2^m} \right)^{-1} w \, d\mathbf{x}. \end{array} \right.$$

Integrating by parts the terms $\int_{\Omega_M} \psi_3^{-1} \nabla \cdot ([O_2*]^3 \mathbf{u}_3) v \, d\mathbf{x}$ and $\int_{\Omega_M} \mu \Delta [O_2*]^3 v \, d\mathbf{x}$, we get

$$\begin{aligned} \int_{\Omega_M} \psi_3^{-1} \nabla \cdot ([O_2*]^3 \mathbf{u}_3) v \, d\mathbf{x} &= - \int_{\Omega_M} \psi_3^{-1} [O_2*]^3 \mathbf{u}_3 \cdot \nabla v \, d\mathbf{x} + \underbrace{\int_{\partial\Omega_M} [O_2*]^3 \psi_3^{-1} \mathbf{u}_3 \cdot \mathbf{n} v \, d\gamma}_{=0} = \\ &= - \int_{\Omega_M} \psi_3^{-1} [O_2*]^3 \mathbf{u}_3 \cdot \nabla v \, d\mathbf{x}, \\ \int_{\Omega_M} \mu \Delta [O_2*]^3 v \, d\mathbf{x} &= - \int_{\Omega_M} \mu \nabla [O_2*]^3 \nabla v \, d\mathbf{x} + \underbrace{\int_{\partial\Omega_M} \mu \nabla [O_2*]^3 v \cdot \mathbf{n} \, d\gamma}_{=0} = \\ &= - \int_{\Omega_M} \mu \nabla [O_2*]^3 \nabla v \, d\mathbf{x}, \end{aligned}$$

since blood and oxygen cannot flow outside the epicardium domain Ω_M , i.e., $\mathbf{u}_3 \cdot \mathbf{n} = 0$ and $\nabla [O_2*]^3 \cdot \mathbf{n} = 0$ on $\partial\Omega_M$.

Hence, the weak formulation is the following.

Problem 3.1. Oxygenation weak problem.

Find $[O_2*]^3 \in V$ and $PO_2^m \in W$ such that

$$\left\{ \begin{array}{l} \int_{\Omega_M} \frac{\partial}{\partial t} [O_2*]^3 v \, d\mathbf{x} + \\ - \int_{\Omega_M} \psi_3^{-1} [O_2*]^3 \mathbf{u}_3 \cdot \nabla v \, d\mathbf{x} - \int_{\Omega_M} \mu \nabla [O_2*]^3 \nabla v \, d\mathbf{x} = \int_{\Omega_M} \psi_3^{-1} \hat{\phi}_{2,3} [O_2*]^2 v \, d\mathbf{x} \\ - \int_{\Omega_M} \psi_3^{-1} \hat{\phi}_{3,\text{veins}} [O_2*]^3 v \, d\mathbf{x} \\ - \int_{\Omega_M} \psi_3^{-1} \tilde{P} \alpha^{-1} (g^{-1}([O_2*]^3) - PO_2^m) v \, d\mathbf{x}, \\ \int_{\Omega_M} \frac{\partial}{\partial t} PO_2^m w \, d\mathbf{x} = \int_{\Omega_M} \psi_m^{-1} \tilde{P} (g^{-1}([O_2*]^3) - PO_2^m) w \, d\mathbf{x} \\ - \int_{\Omega_M} \tilde{\xi}_0 \left(1 + \frac{PO_2^{m,50}}{PO_2^m} \right)^{-1} w \, d\mathbf{x}, \end{array} \right.$$

for every test functions $v \in V$ and $w \in W$.

3.2. Space discretization

We introduce a standard Galerkin approximation of the Problem 3.1, and we define a finite-dimensional subspaces of V and W

$$V^h \subset V, \quad W^h \subset W \quad \dim(V^h) = N_V^h, \quad \dim(W^h) = N_W^h, \quad h > 0.$$

which depend on the discretization parameter h . In practice, for the sake of simplicity, we choose $V_h = W_h$, so that $\dim(V^h) = \dim(W^h)$. To construct these subspaces, we use the FEM: we denote by \mathcal{T}_h a regular partition of the domain Ω_M into a set of tetrahedra (or hexahedra) $\{K\}$, and we define the discretized domain

$$\Omega_M^h = \bigcup_{K \in \mathcal{T}_h} K,$$

where h define the characteristic mesh size, i.e. $h = \max_{K \in \mathcal{T}_h} h_K$, being h_K the diameter of the element K . Solutions of Problem 3.1 are approximated using finite polynomial elements, namely they are in the spaces

$$V_k^h = W_k^h = \{v_h \in L^2(\Omega_M) : v_h|_K \in P_k(K) \ \forall K \in \mathcal{T}_h\},$$

for any $k \geq 0$, where P_k indicates the space of polynomials of global degree non-greater than k in the spatial coordinate $\mathbf{x} = (x, y, z)$.

In the case of hexahedral triangulation, we substitute the space P_k with Q_k , which indicates the space of tensor-product of one-dimensional polynomials of global degree non-greater than k .

We define the number of degrees of freedom of our discrete space as

$$N^h = \dim(V_k^h) = \dim(W_k^h).$$

Hence, the semi-discrete Galerkin formulation of the problem is the following.

Problem 3.2. Oxygenation semi-discrete Galerkin problem.

Find $[\text{O}_2*]_h^3 \in V_h$ and $\text{PO}_2^m h \in V_h$ such that

$$\left\{ \begin{array}{l} \int_{\Omega_M} \frac{\partial}{\partial t} [\text{O}_2*]_h^3 v_h \, d\mathbf{x} + \\ - \int_{\Omega_M} [\text{O}_2*]_h^3 \psi_3^{-1} \mathbf{u}_3 \cdot \nabla v_h \, d\mathbf{x} - \int_{\Omega_M} \mu \nabla [\text{O}_2*]_h^3 \nabla v_h \, d\mathbf{x} = \int_{\Omega_M} \psi_3^{-1} \widehat{\phi}_{2,3} [\text{O}_2*]_h^2 v_h \, d\mathbf{x} \\ - \int_{\Omega_M} \psi_3^{-1} \widehat{\phi}_{3,\text{veins}} [\text{O}_2*]_h^3 v_h \, d\mathbf{x} \\ - \int_{\Omega_M} \psi_3^{-1} \widetilde{P} \alpha^{-1} (g^{-1}([\text{O}_2*]_h^3) - \text{PO}_2^m h) v_h \, d\mathbf{x}, \\ \int_{\Omega_M} \frac{\partial}{\partial t} \text{PO}_2^m h w_h \, d\mathbf{x} = \int_{\Omega_M} \psi_m^{-1} \widetilde{P} (g^{-1}([\text{O}_2*]_h^3) - \text{PO}_2^m h) w_h \, d\mathbf{x} \\ - \int_{\Omega_M} \tilde{\xi}_0 \left(1 + \frac{\text{PO}_2^{m,50}}{\text{PO}_2^m h} \right)^{-1} w_h \, d\mathbf{x}, \end{array} \right.$$

for every test functions $v_h \in V_h$ and $w_h \in V_h$.

3.3. Time discretization

For the time discretization, we subdivide the time interval $[0, T]$ into $N_{\Delta t}$ subintervals of size $\Delta t = \frac{T}{N_{\Delta t}}$, so that the time steps are defined as $t_k = k\Delta t$ for $k = 0, \dots, N_{\Delta t}$. We decided to use a semi-implicit method for the time discretization scheme. In particular, we use an

- implicit treatment for the linear terms;
- explicit treatment for the nonlinear terms (i.e., g function) and to decouple the two problems.

Using the notation

$$\begin{aligned} [\mathrm{O}_2*]^{3,k} &\simeq [\mathrm{O}_2*]^3(\boldsymbol{x}, t_k), \quad \mathrm{PO}_2^{m,k} \simeq \mathrm{PO}_2^m(\boldsymbol{x}, t_k), \\ \boldsymbol{u}_3^k &\simeq \boldsymbol{u}_3(\boldsymbol{x}, t_k), \quad \widehat{\phi}_{i,j}^k \simeq \widehat{\phi}_{i,j}(\boldsymbol{x}, t_k), \end{aligned} \quad (3.6)$$

we get the following problem.

Problem 3.3. Oxygenation discrete Galerkin problem.

For each $k = 0, \dots, N_{\Delta t} - 1$, find $[\mathrm{O}_2*]^{3,k+1} \in V^h$ and $\mathrm{PO}_2^{m,k+1} \in V^h$ such that

$$\left\{ \begin{array}{l} \int_{\Omega_M} \frac{[\mathrm{O}_2*]_h^{3,k+1}}{\Delta t} v_h \, d\boldsymbol{x} - \int_{\Omega_M} [\mathrm{O}_2*]_h^{3,k+1} \psi_3^{-1} \boldsymbol{u}_3^k \cdot \nabla v_h \, d\boldsymbol{x} \\ \quad - \int_{\Omega_M} \mu \nabla [\mathrm{O}_2*]_h^{3,k+1} \nabla v_h \, d\boldsymbol{x} + \int_{\Omega_M} \psi_3^{-1} \widehat{\phi}_{3,\text{veins}}^k [\mathrm{O}_2*]_h^{3,k+1} v_h \, d\boldsymbol{x} \\ \quad = \int_{\Omega_M} \frac{[\mathrm{O}_2*]_h^{3,k}}{\Delta t} v_h \, d\boldsymbol{x} + \int_{\Omega_M} \psi_3^{-1} \widehat{\phi}_{2,3}^k [\mathrm{O}_2*]_h^{2,k+1} v_h \, d\boldsymbol{x} \\ \quad - \int_{\Omega_M} \psi_3^{-1} \widetilde{P} \alpha^{-1} \left(g^{-1}([\mathrm{O}_2*]_h^{3,k}) - \mathrm{PO}_2^{m,k} \right) v_h \, d\boldsymbol{x}, \\ \int_{\Omega_M} \frac{\mathrm{PO}_2^{m,k+1}}{\Delta t} w_h \, d\boldsymbol{x} = \int_{\Omega_M} \frac{\mathrm{PO}_2^{m,k}}{\Delta t} w_h \, d\boldsymbol{x} + \int_{\Omega_M} \psi_m^{-1} \widetilde{P} (g^{-1}([\mathrm{O}_2*]_h^{3,k}) - \mathrm{PO}_2^{m,k}) w_h \, d\boldsymbol{x} \\ \quad - \int_{\Omega_M} \widetilde{\xi}_0 \left(1 + \frac{\mathrm{PO}_2^{m,50}}{\mathrm{PO}_2^{m,k}} \right)^{-1} w_h \, d\boldsymbol{x}, \end{array} \right.$$

for every test functions $v_h \in V_h$ and $w_h \in W_h$.

3.4. Algebraic formulation

To derive the algebraic formulation of the discrete problem, we define the two set of basis functions $\{\varphi_j\}_{j=1}^{N_h}$ for V^h and $\{\eta_j\}_{j=1}^{N_h}$ for W^h , which we recall being two basis of two vectorial spaces. We can write all the functions and the unknowns of the Galerkin problem belonging to the subspaces as a linear combination of the basis functions, namely $\forall \boldsymbol{x} \in \Omega_M, \forall k = 0, \dots, N_{\Delta t}$ we write

$$[\mathrm{O}_2*]^{3,k}(\boldsymbol{x}) = \sum_{j=1}^{N_h} [\mathrm{O}_2*]_j^{3,k} \varphi_j(\boldsymbol{x}), \quad \mathrm{PO}_2^{m,k}(\boldsymbol{x}) = \sum_{j=1}^{N_h} \mathrm{PO}_2^{m,k}{}_j \eta_j(\boldsymbol{x}), \quad (3.8)$$

where $[\mathrm{O}_2*]_j^{3,k}$ and $\mathrm{PO}_2^{m,k}{}_j, j = 1, \dots, N_h$, are the coefficients of such linear combinations.

By collecting them in vectors, we get

$$[\mathrm{O}_2*]^{3,k} = \left\{ [\mathrm{O}_2*]_j^{3,k} \right\}_{j=1}^{N_h}, \quad \mathrm{PO}_2^{m,k} = \left\{ \mathrm{PO}_2^{m,k}{}_j \right\}_{j=1}^{N_h}, \quad \forall k = 0, \dots, N_{\Delta t}. \quad (3.9)$$

Using (3.6) in Problem 3.3 and choosing $v_h = \varphi_i$ and $w_h = \eta_i \forall i = 1, \dots, N_h$, we get the algebraic system related to the problem to be solved for each $k = 0, \dots, N_{\Delta t} - 1$, which is

$$\begin{bmatrix} \mathbb{A}^k & \mathbb{O} \\ \mathbb{O} & \mathbb{B} \end{bmatrix} \begin{bmatrix} [\text{O}_2*]^{3,k+1} \\ \text{PO}_2^{m,k+1} \end{bmatrix} = \begin{bmatrix} \mathbf{F}^k \\ \mathbf{G}^k \end{bmatrix}, \quad (3.10)$$

where the submatrices and subvectors are defined as

$$\begin{aligned} [\mathbb{A}]_{i,j}^k &= \int_{\Omega_M} \frac{1}{\Delta t} \varphi_j \varphi_i \, d\mathbf{x} - \int_{\Omega_M} \mu \nabla \varphi_j \nabla \varphi_i \, d\mathbf{x} \\ &\quad - \int_{\Omega_M} \varphi_j \psi_3^{-1} \mathbf{u}_3^k \cdot \nabla \varphi_i \, d\mathbf{x} + \int_{\Omega_M} \psi_3^{-1} \widehat{\phi}_{3,\text{veins}}^k \varphi_j \varphi_i \, d\mathbf{x}, \\ [\mathbb{B}]_{i,j} &= \delta_{ij}, \\ [\mathbf{F}]_i^k &= \int_{\Omega_M} \frac{[\text{O}_2*]^{3,k}}{\Delta t} \varphi_i \, d\mathbf{x} + \int_{\Omega_M} \psi_3^{-1} \widehat{\phi}_{2,3}^k [\text{O}_2*]^{2,k+1} \varphi_i \, d\mathbf{x} \\ &\quad - \int_{\Omega_M} \psi_3^{-1} \widetilde{P} \alpha^{-1} \left(g^{-1} ([\text{O}_2*]^{3,k}) - \text{PO}_2^{m,k} \right) \varphi_i \, d\mathbf{x}, \\ [\mathbf{G}]_i^k &= \int_{\Omega_M} \text{PO}_2^{m,k} \eta_i \, d\mathbf{x} + \int_{\Omega_M} \Delta t \psi_m^{-1} \widetilde{P} (g^{-1} ([\text{O}_2*]^{3,k}) - \text{PO}_2^{m,k}) \eta_i \, d\mathbf{x} \\ &\quad - \int_{\Omega_M} \Delta t \tilde{\xi}_0 \left(1 + \frac{\text{PO}_2^{m,50}}{\text{PO}_2^{m,k}} \right)^{-1} \eta_i \, d\mathbf{x}, \end{aligned}$$

and where, for each $k = 0, \dots, N_{\Delta t} - 1$, we have $\mathbb{A}^k, \mathbb{B} \in \mathbb{R}^{N_h \times N_h}$ and $\mathbf{F}^k, \mathbf{G}^k \in \mathbb{R}^{N_h}$.

3.5. Runge-Kutta method for the 0D model

In some cases, we can be interested in solving the 0D model, i.e., neglecting the diffusive and transport terms. The system associated with the complete model becomes

$$\left\{ \begin{array}{l} \frac{\partial}{\partial t} \text{PO}_2^3 = n\alpha[\text{Hb}*]k_- \left(\text{SO}_2^3 - (1 - \text{SO}_2^3) \left(\frac{\text{PO}_2^3}{\text{PO}_2^{50}} \right)^n \right) \\ \quad + \psi_3^{-1} \widehat{\phi}_{2,3} \text{PO}_2^a - \psi_3^{-1} \widehat{\phi}_{3,\text{veins}} \text{PO}_2^3 \\ \quad - \psi_3^{-1} \widetilde{P} (\text{PO}_2^3 - \text{PO}_2^m), \end{array} \right. \quad (3.11a)$$

$$\left\{ \begin{array}{l} \frac{\partial}{\partial t} \text{SO}_2^3 = -k_- \left(\text{SO}_2^3 - (1 - \text{SO}_2^3) \left(\frac{\text{PO}_2^3}{\text{PO}_2^{50}} \right)^n \right) \\ \quad + \psi_3^{-1} \widehat{\phi}_{2,3} \text{SO}_2^a - \psi_3^{-1} \widehat{\phi}_{3,\text{veins}} \text{SO}_2^3, \end{array} \right. \quad (3.11b)$$

$$\left\{ \begin{array}{l} \frac{\partial}{\partial t} \text{PO}_2^m = \psi_m^{-1} \widetilde{P} (\text{PO}_2^3 - \text{PO}_2^m) - \tilde{\xi}_0 \left(1 + \frac{\text{PO}_2^{m,50}}{\text{PO}_2^m} \right)^{-1}, \end{array} \right. \quad (3.11c)$$

and the one associated with the reduced model becomes

$$\left\{ \begin{array}{l} \frac{\partial}{\partial t} [\text{O}_2*]^3 = \psi_3^{-1} \hat{\phi}_{2,3} [\text{O}_2*]^2 - \psi_3^{-1} \hat{\phi}_{3,\text{veins}} [\text{O}_2*]^3 \\ \quad - \psi_3^{-1} \tilde{P} \alpha^{-1} (g^{-1}([\text{O}_2*]^3) - \text{PO}_2^m), \\ \frac{\partial}{\partial t} \text{PO}_2^m = \psi_m^{-1} \tilde{P} (g^{-1}([\text{O}_2*]^3) - \text{PO}_2^m) \\ \quad - \tilde{\xi}_0 \left(1 + \frac{\text{PO}_2^{m,50}}{\text{PO}_2^m} \right)^{-1}. \end{array} \right. \quad (3.12a)$$

$$(3.12b)$$

In order to simplify the notation, we define

$$y_1(t) := \text{PO}_2^3(t),$$

$$y_2(t) := \text{SO}_2^3(t),$$

$$y_3(t) := \text{PO}_2^m(t),$$

$$f_1(t, y_1(t), y_2(t), y_3(t)) := n\alpha[\text{Hb}*]k_- \left(y_2(t) - (1 - y_2(t)) \left(\frac{y_1(t)}{\text{PO}_2^{50}} \right)^n \right)$$

$$+ \psi_3^{-1} \hat{\phi}_{2,3} \text{PO}_2^a - \psi_3^{-1} \hat{\phi}_{3,\text{veins}} y_1(t)$$

$$- \psi_3^{-1} \tilde{P} (y_1(t) - y_3(t)),$$

$$f_2(t, y_1(t), y_2(t), y_3(t)) := -k_- \left(y_2(t) - (1 - y_2(t)) \left(\frac{y_1(t)}{\text{PO}_2^{50}} \right)^n \right)$$

$$+ \psi_3^{-1} \hat{\phi}_{2,3} \text{SO}_2^a - \psi_3^{-1} \hat{\phi}_{3,\text{veins}} y_2(t),$$

$$f_3(t, y_1(t), y_2(t), y_3(t)) := \psi_m^{-1} \tilde{P} (y_1(t) - y_3(t)) - \tilde{\xi}_0 \left(1 + \frac{\text{PO}_2^{m,50}}{y_3(t)} \right)^{-1},$$

$$\mathbf{y}(t) := [y_1(t), y_2(t), y_3(t)]^T, \quad \mathbf{f}(t, \mathbf{y}(t)) := [f_1(t, \mathbf{y}(t)), f_2(t, \mathbf{y}(t)), f_3(t, \mathbf{y}(t))]^T, \quad \mathbf{y}_0 := [\text{PO}_2^a, \text{SO}_2^a, \text{PO}_2^m]^T$$

for the complete model, and

$$y_1(t) := [\text{O}_2*]^3(t),$$

$$y_2(t) := \text{PO}_2^m(t),$$

$$f_1(t, y_1(t), y_2(t)) := \psi_3^{-1} \hat{\phi}_{2,3} y_1(t) - \psi_3^{-1} \hat{\phi}_{3,\text{veins}} y_2(t) - \psi_3^{-1} \tilde{P} \alpha^{-1} ((g^{-1} y_1(t)) - y_2(t)),$$

$$f_2(t, y_1(t), y_2(t)) := \psi_m^{-1} \tilde{P} (g^{-1}(y_1(t)) - y_2(t)) - \tilde{\xi}_0 \left(1 + \frac{\text{PO}_2^{50}}{y_2(t)} \right)^{-1},$$

$$\mathbf{y}(t) := [y_1(t), y_2(t)]^T, \quad \mathbf{f}(t, \mathbf{y}(t)) := [f_1(t, \mathbf{y}(t)), f_2(t, \mathbf{y}(t))]^T, \quad \mathbf{y}_0 := [g(\text{PO}_2^a), \text{PO}_2^m]^T$$

for the reduced model.

Hence, in both cases, the problem can be summarized to the ODEs system

$$\begin{cases} \dot{\mathbf{y}}(t) = \mathbf{f}(t, \mathbf{y}(t)), & t \in [0, T] \\ \mathbf{y}(0) = \mathbf{y}_0. \end{cases} \quad (3.15a)$$

$$(3.15b)$$

For the time discretization, as before, we subdivide the time interval $[0, T]$ into $N_{\Delta t}$ subintervals of dimension $\Delta t = \frac{T}{N_{\Delta t}}$, so that the time steps are defined as $t_k = k\Delta t$ for $k = 0, \dots, N_{\Delta t}$. We denote as \mathbf{y}_k the approximation of \mathbf{y} evaluated at t_k , namely $\mathbf{y}_k \approx \mathbf{y}(t_k)$, with $\{t_k\}_{k=0}^{N_{\Delta t}}$. The Runge-Kutta explicit scheme of the fourth order to solve the ODEs system is the following.

Algorithm 3.1 Fourth-order Runge-Kutta method

1: **for** $k = 0, \dots, N_{\Delta t} - 1$ **do**

2: Compute at timestep k :

$$\begin{aligned} \mathbf{RK}_1 &:= \mathbf{f}(t_k, \mathbf{y}_k) \\ \mathbf{RK}_2 &:= \mathbf{f}\left(t_k + \frac{\Delta t}{2}, \mathbf{y}_k + \frac{\Delta t}{2} \mathbf{RK}_1\right) \\ \mathbf{RK}_3 &:= \mathbf{f}\left(t_k + \frac{\Delta t}{2}, \mathbf{y}_k + \frac{\Delta t}{2} \mathbf{RK}_2\right) \\ \mathbf{RK}_4 &:= \mathbf{f}(t_{k+1}, \mathbf{y}_k + \Delta t \mathbf{RK}_3) \end{aligned}$$

3: Compute at timestep k :

$$\mathbf{y}_{k+1} = \mathbf{y}_k + \frac{\Delta t}{6} (\mathbf{RK}_1 + 2\mathbf{RK}_2 + 2\mathbf{RK}_3 + \mathbf{RK}_4)$$

4: **end for**

3.6. Oxygen fluxes approximation

After solving the problem, we want to compute the average oxygen flux delivered and consumed (2.37). We denote as \bar{a} the spatial average of the field a (of course, we consider $\bar{a} \equiv a$ in case of 0D model) so we get, for the timestep k , that

$$\lambda_{\text{O}_2}^{\text{del}}(t_k) \approx \tilde{P}\alpha^{-1}(g^{-1}(\overline{[\text{O}_2^*]^3(t_k)} - \overline{\text{PO}_2^m(t_k)}), \quad \lambda_{\text{O}_2}^{\text{cons}}(t_k) \approx \psi_m \tilde{\xi}_0 \alpha^{-1} \left(1 + \frac{\overline{\text{PO}_2^{m,50}}}{\overline{\text{PO}_2^m(t_k)}}\right)^{-1}.$$

Finally, to compute the total flux, we integrate the average ones using trapezoidal rule [91], hence we get, for the timestep k , that

$$\Lambda_{O_2}^{\text{del}}(t_k) \approx \frac{\Delta t}{2} \sum_{i=1}^k (\lambda_{O_2}^{\text{del}}(t_{i-1}) + \lambda_{O_2}^{\text{del}}(t_i)), \quad \Lambda_{O_2}^{\text{cons}}(t_k) \approx \frac{\Delta t}{2} \sum_{i=1}^k (\lambda_{O_2}^{\text{cons}}(t_{i-1}) + \lambda_{O_2}^{\text{cons}}(t_i)).$$

3.7. Coupling schemes

In this section, we provide the numerical scheme associated to the coupling conditions of Section 2.4. In particular

- in Section 3.7.1 we adopted an iterative splitting strategy [25] for the two-way coupling between the fluid dynamics and the perfusion model;
- in Section 3.7.2 we leveraged the fact that the oxygenation model depends only one-way from the perfusion one, allowing to simply providing the coupling variables to the oxygenation model, after having computed it from the Darcy one.

3.7.1. Iterative splitting for fluid dynamics and perfusion

A monolithic (one shot) approach for the numerical solution of the coupled problem would be very demanding regarding the implementation complexity. Hence, as proposed and detailed in [25], we use an iterative strategy based on splitting the problem into two sub-problems solved sequentially, thus exploiting the available fluid and multi-compartment Darcy solvers.

In particular, the idea is to equip the fluid problem with a Neumann boundary condition coming from the Robin interface condition (2.45c) and to provide to the first (most upstream) Darcy problem a mass term coming from (2.45f).

The iterative procedure is summarized in Algorithm 3.2, omitting the current temporal index $k + 1$ to simplify the notation. We denote by s the current iteration and by ε_{tol} a given tolerance. Moreover, we define the residual of the field a as

$$\text{diff}(a) = \frac{\|a^{(s)} - a^{(s-1)}\|}{\|a^{(s)}\|},$$

where the norms are intended to be in $[H^1]^3$ for the velocities and L^2 for the pressures. Finally, we introduce in each iteration a relaxation of the solutions of p_1 and \mathbf{u}_C through the relaxation coefficients ω_M and ω_C , respectively.

Algorithm 3.2 Iterative splitting strategy for coronaries and perfusion

1: **for** $k = 1, \dots, N_{\Delta t}$ **do**
 2: **while** $\max(\text{diff}(\mathbf{u}_C), \text{diff}(p_C), \text{diff}(\mathbf{u}_1), \text{diff}(p_1)) > \varepsilon_{\text{tol}}$ **do**
 3: Solve the fluid problem at iteration s :

$$\left\{ \begin{array}{l} \rho \left(\frac{\tilde{\mathbf{u}}_C^{(s)} - \mathbf{u}_C^k}{\Delta t} + (\mathbf{u}_C^k \cdot \nabla) \tilde{\mathbf{u}}_C^{(s)} \right) + \\ -\mu_C \nabla \cdot \left(\nabla \tilde{\mathbf{u}}_C^{(s)} + (\nabla \tilde{\mathbf{u}}_C^{(s)})^T \right) + \nabla p_C^{(s)} = \mathbf{0} \text{ in } \Omega_C, \\ \nabla \cdot \tilde{\mathbf{u}}_C^{(s)} = 0 \text{ in } \Omega_C, \\ -p_C^{(s)} + \mu_C \left(\nabla \tilde{\mathbf{u}}_C^{(s)} + (\nabla \tilde{\mathbf{u}}_C^{(s)})^T \right) \mathbf{n} \cdot \mathbf{n} = -\frac{1}{\alpha^j} \int_{\Gamma^j} \mathbf{u}_C^{(s-1)} \cdot \mathbf{n} \, d\gamma + \\ -\frac{1}{|\Omega_M^j|} \int_{\Omega_M^j} p_1^{(s-1)} \, d\mathbf{x} \text{ on } \Gamma^j, \\ \mu_C \left(\nabla \tilde{\mathbf{u}}_C^{(s)} + (\nabla \tilde{\mathbf{u}}_C^{(s)})^T \right) \mathbf{n} \cdot \boldsymbol{\tau}_i = 0, \quad i = 1, 2 \text{ on } \Gamma^j. \end{array} \right.$$

4: Solve the three-compartment Darcy problem at iteration s :

$$\left\{ \begin{array}{l} \mathbf{u}_1^{(s)} + \mathbf{K}_1 \nabla \tilde{p}_1^{(s)} = \mathbf{0} \text{ in } \Omega_M, \\ \nabla \cdot \mathbf{u}_1^{(s)} = \sum_{j=1}^J \frac{\chi_{\Omega_M^j}}{|\Omega_M^j|} \int_{\Gamma^j} \tilde{\mathbf{u}}_C^{(s)} \cdot \mathbf{n} \, d\gamma - \beta_{1,2} (\tilde{p}_1^{(s)} - p_2^{(s)}) \text{ in } \Omega_M, \\ \mathbf{u}_2^{(s)} + \mathbf{K}_2 \nabla p_2^{(s)} = \mathbf{0} \text{ in } \Omega_M, \\ \nabla \cdot \mathbf{u}_2^{(s)} = -\beta_{2,1} (p_2^{(s)} - \tilde{p}_1^{(s)}) - \beta_{2,3} (p_2^{(s)} - p_3^{(s)}) \text{ in } \Omega_M, \\ \mathbf{u}_3^{(s)} + \mathbf{K}_3 \nabla p_3^{(s)} = \mathbf{0} \text{ in } \Omega_M, \\ \nabla \cdot \mathbf{u}_3^{(s)} = -\gamma (p_3^{(s)} - p_{\text{veins}}) - \beta_{3,2} (p_3^{(s)} - p_2^{(s)}) \text{ in } \Omega_M, \\ \mathbf{u}_i \cdot \mathbf{n} = 0, \quad i = 1, 2, 3 \text{ on } \partial\Omega_M \end{array} \right.$$

5: $p_1^{(s)} = \omega_M \tilde{p}_1^{(s)} + (1 - \omega_M) p_1^{(s-1)}$
 6: $\mathbf{u}_C^s = \omega_C \tilde{\mathbf{u}}_C^{(s)} + (1 - \omega_C) \mathbf{u}_C^{(s-1)}$
 7: $s \leftarrow s + 1$
 8: **end while**
 9: **end for**

The linear algebraic system associated with the fluid problem (3.19) is solved using the preconditioned GMRES [97]. In particular, we consider the SIMPLE preconditioner in its approximated formulation (aSIMPLE) [4, 65, 94, 96]. Regarding the multi-compartment Darcy problem (3.20), as detailed in [25], we use a preconditioned conjugate gradient (CG) method [42, 91, 94].

3.7.2. One-way coupling between oxygenation and perfusion

As described in Section 2.4.2, to couple the oxygenation model with the Darcy model, for each time step $k = 0, \dots, N_{\Delta t} - 1$, we solve the fluid and perfusion problems and then we compute

$$\mathbf{u}_3^k = -\mathbf{K}_3 \nabla p_3^k, \quad (3.21a)$$

$$\widehat{\phi}_{2,3}^k = \beta_{2,3}(p_3^k - p_2^k), \quad (3.21b)$$

$$\widehat{\phi}_{3,\text{veins}}^k = \gamma(p_3^k - p_{\text{veins}}), \quad (3.21c)$$

where p_i^k , $i = 1, 2, 3$ denotes the Darcy pressures at timestep k . The coupling procedure is summarized in the following Algorithm 3.3.

Algorithm 3.3 One-way coupling between three-compartments Darcy and oxygenation model

1: **for** $k = 0, \dots, N_{\Delta t} - 1$ **do**

2: Perform the iterative splitting strategy of Algorithm 3.2 at timestep k .

3: Compute the coupling variables at timestep k :

$$\begin{aligned} \mathbf{u}_3^k &= -\mathbf{K}_3 \nabla p_3^k, \\ \widehat{\phi}_{2,3}^k &= \beta_{2,3}(p_3^k - p_2^k), \\ \widehat{\phi}_{3,\text{veins}}^k &= \gamma(p_3^k - p_{\text{veins}}) \end{aligned}$$

4: Assemble submatrices \mathbb{A}^k, \mathbb{B} and subvectors $\mathbf{F}^k, \mathbf{G}^k$ at timestep k .

5: Solve the corresponding algebraic linear system:

$$\begin{bmatrix} \mathbb{A}^k & \mathbb{O} \\ \mathbb{O} & \mathbb{B} \end{bmatrix} \begin{bmatrix} [\text{O}_2*]^{3,k+1} \\ \text{PO}_2^{m,k+1} \end{bmatrix} = \begin{bmatrix} \mathbf{F}^k \\ \mathbf{G}^k \end{bmatrix}$$

6: Reconstruct PO_2^3 and SO_2^3 at the timestep k .

7: Compute the approximated oxygen fluxes:

$$\begin{aligned} \lambda_{\text{O}_2}^{\text{del}}(t_{k+1}) &\approx \tilde{P}\alpha^{-1}(g^{-1}(\overline{[\text{O}_2*]^3(t_{k+1})}) - \overline{\text{PO}_2^m(t_{k+1})}), & \Lambda_{\text{O}_2}^{\text{del}}(t_{k+1}) &\approx \frac{\Delta t}{2} \sum_{i=1}^{k+1} (\lambda_{\text{O}_2}^{\text{del}}(t_{i-1}) + \lambda_{\text{O}_2}^{\text{del}}(t_i)), \\ \lambda_{\text{O}_2}^{\text{cons}}(t_{k+1}) &\approx \psi_m \tilde{\xi}_0 \alpha^{-1} \left(1 + \frac{\text{PO}_2^{m,50}}{\overline{\text{PO}_2^m(t_{k+1})}} \right)^{-1}, & \Lambda_{\text{O}_2}^{\text{cons}}(t_{k+1}) &\approx \frac{\Delta t}{2} \sum_{i=1}^{k+1} (\lambda_{\text{O}_2}^{\text{cons}}(t_{i-1}) + \lambda_{\text{O}_2}^{\text{cons}}(t_i)). \end{aligned}$$

8: **end for**

The linear algebraic system is solved using the Jacobi-preconditioned GMRES [91, 94].

4 | Tests and results

In this chapter, we present and discuss the main results of this work. We will focus on the main object of interest in all the simulations performed: the scalar fields PO_2^3 , PO_2^m , SO_2^3 and $[\text{O}_2*]^3$, and the oxygen fluxes $\lambda_{\text{O}_2}^{\text{del}}$, $\lambda_{\text{O}_2}^{\text{cons}}$ and $\Lambda_{\text{O}_2}^{\text{del}}$, $\Lambda_{\text{O}_2}^{\text{cons}}$.

Firstly, in Section 4.2, we show the results of the 0D model in a physiological case discussing the main output fields. In Section 4.2, we show some tests we performed to assess the oxygenation model's validity and verify its implementation in life^x.

Finally, in Section 4.3, we study some real case scenarios performing simulations on real geometries of coronaries and myocardium to discuss the differences intercurring in some physiological and pathological conditions.

The simulations we show in this chapter were executed on 56 cores running Intel Xeon Gold 6238@2.10 GHz, using the computational resources available at MOX, Dipartimento di Matematica, Politecnico di Milano.

4.1. Output of 0D model

As a first step in providing the results of this work, we performed a simulation of 2.8 s duration and $\Delta t = 10^{-5}$ s using the complete 0D model, uncoupled by the other physics, in order to discuss the meaning of its output. The parameters are chosen as listed in Section 2.3, both with the inward/outward flux (2.33), to simulate a physiological case. The latter provides, as described in Section 2.3.5, a value of $\bar{\Psi}_{\text{CBF}}$ near the physiological one. The initial values of PO_2^3 and PO_2^m are tuned quickly reach a limit cycle and, in physiological conditions, they are 33 mmHg and 16 mmHg respectively, while the initial values of other fields can be reconstruct from these by means of (2.35) and (2.30).

In Figure 4.1 we show the scalar fields PO_2^3 , PO_2^m , SO_2^3 and $[\text{O}_2*]^3$ which are, of course, only time-dependent function in 0D case, both with the averaged and total oxygen fluxes, namely $\lambda_{\text{O}_2}^{\text{del}}$, $\lambda_{\text{O}_2}^{\text{cons}}$ and $\Lambda_{\text{O}_2}^{\text{del}}$, $\Lambda_{\text{O}_2}^{\text{cons}}$. In 3D cases, we will plot the spatial averages of the scalar fields.

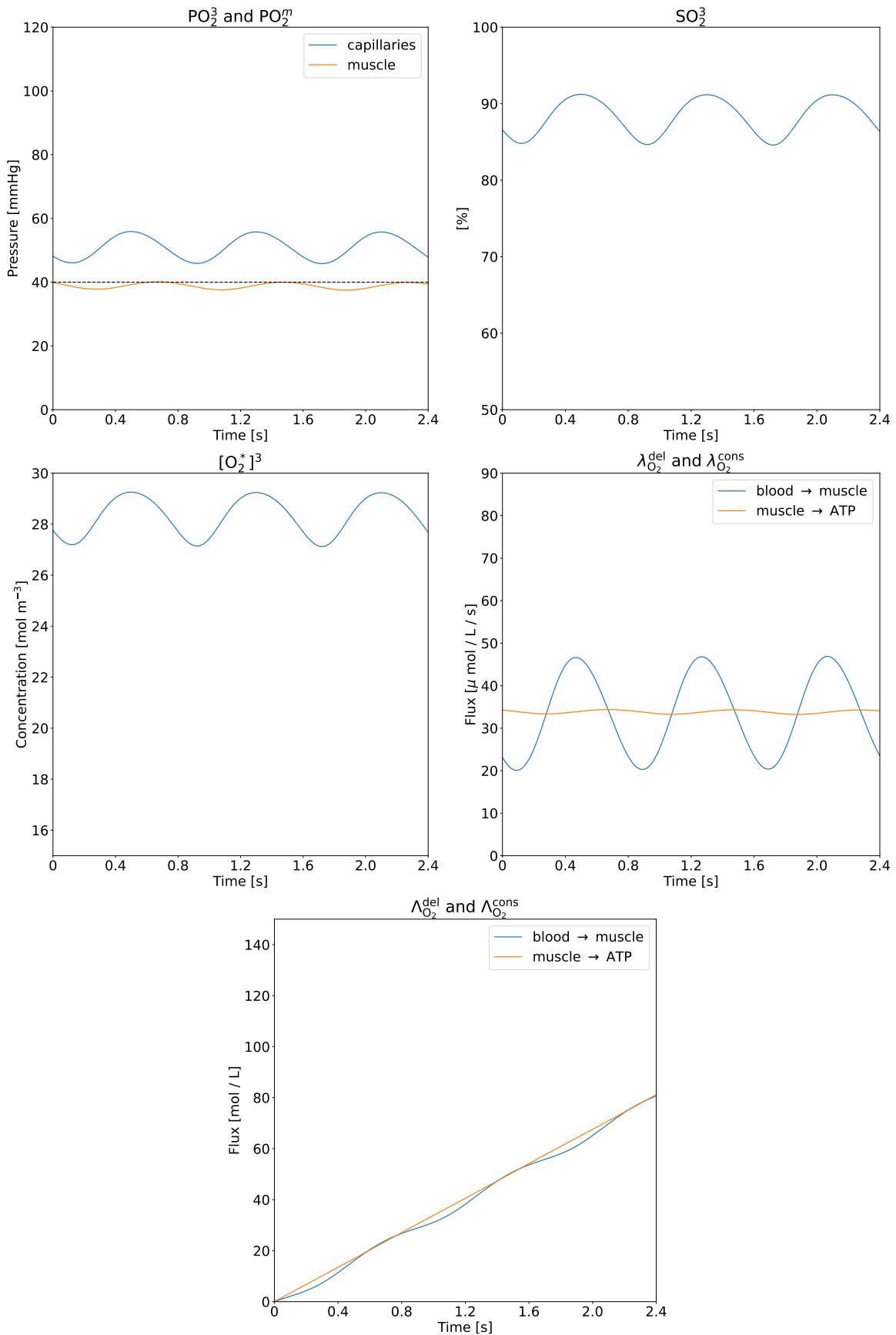


Figure 4.1: Results of the 0D model in physiological scenario.

We recall that PO_2^3 is the partial oxygen pressure in capillaries, while PO_2^m is the partial oxygen pressure in the muscle. In physiological conditions, as in this case, the former must be higher than the latter due to the pressure gradient, which allows oxygen to perfuse only from capillaries to tissue.

Regarding the oxygen saturation SO_2^3 in capillaries, we can see values oscillating between a minimum value of 84.5%, corresponding to the blood in venous capillaries, and a maximum value of 91.3%, corresponding to the blood in arterial capillaries, with an average value of 88.2%. The values of SO_2^3 and PO_2^3 indicates that the hemoglobin is well oxygenated, as we can see also from the values of $[\text{O}_2*]^3$, namely the concentration of oxygen both bound to hemoglobin or unrestricted in the plasma.

The curves $\lambda_{\text{O}_2}^{\text{del}}$ and $\lambda_{\text{O}_2}^{\text{cons}}$ correspond to the oxygen fluxes delivered from capillaries to the muscle and consumed by the muscle to produce ATP. The latter oscillates with lower magnitude exhibiting a buffer pattern: an increase in the oxygen flux in the muscle is correlated with an increase of the flux into the capillaries. On the other hand, a lower concentration of oxygen in the capillaries causes a lower quantity of oxygen in the muscle. Finally, the total oxygen fluxes $\Lambda_{\text{O}_2}^{\text{del}}$ and $\Lambda_{\text{O}_2}^{\text{cons}}$ are the time integral of the previous ones. The magnitude of $\Lambda_{\text{O}_2}^{\text{cons}}$ is lower (as the one of $\lambda_{\text{O}_2}^{\text{cons}}$), and the curves have the same linear increasing trend. This output seems in good accordance with literature [24, 51], confirming the physical accordance of the model.

4.2. Tests on idealized geometry

In this section, we provide the results of comparisons between different simulations to check the model validity and its implementation in life^x. In particular

- in Section 4.2.1 we compare the complete and reduced model to check the validity of the quasistatic-chemistry assumption;
- in Section 4.2.2 we compare the 3D and 0D models to check if, in proper conditions, the 0D model is a good approximation of the 3D one;
- in Section 4.2.3 we finally introduce the coupled model, both in case of simulation of only perfusion or including also the coronaries, and we compare it with the uncoupled one.

4.2.1. Comparison between complete and reduced 0D model

In this and the following section, we focus on the uncoupled model as described in the last part of Section 2.3.5. Since the reduced model is built up under the quasistatic-chemistry assumption, namely that the chemical reaction of hemoglobin oxygenation is much faster than diffusion and transport, the first test we performed regarded the similarity of the complete and reduced model. If this assumption is correct, we expect the two different models to provide almost identical results, and we expect the complete model to need a smaller time step with respect to the reduced one for stability reasons since it has to capture the swift chemical reaction adequately.

To this end, we performed two simulations of 2.8 s duration with the same parameters, using the complete model in one case and the reduced one in the other.

First of all, we noticed that using a timestep significantly larger than that $\Delta t = 10^{-5}$ s, the complete model provides results which are very different with respect to ones of the reduced model, but using $\Delta t = 10^{-5}$ s the results are almost identical as shown in Figure 4.2. This fact confirms the consistency of our implementation of both the models and the validity of the quasistatic-chemistry assumption. Since the complete model needs a very fine timestep, which could be unfeasible in 3D simulations, we will consider only the reduced model from now on.

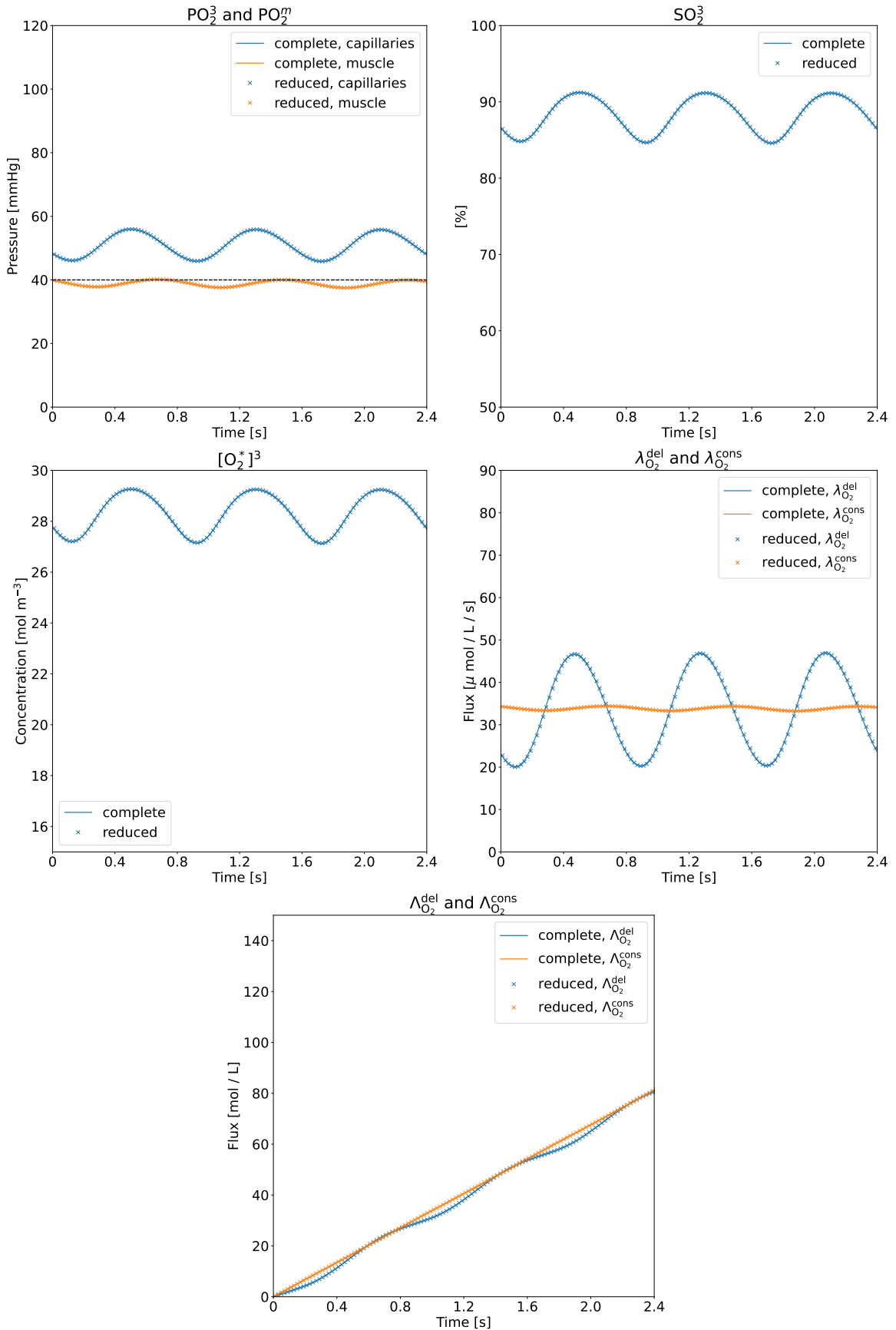


Figure 4.2: Comparison between reduced and complete model.

4.2.2. Comparison between 3D and 0D model

Before passing to the coupled model, we also compare the uncoupled 3D and 0D models. This comparison has multiple goals: to validate the solver's implementation, to check if the diffusion term makes a great difference, and to assess if the 0D model is a good approximation for the most computationally expensive 3D one. In this simulations on idealized geometry, the myocardium is idealized by a cube of length $l_M = 1$ cm as in Figure 4.3.

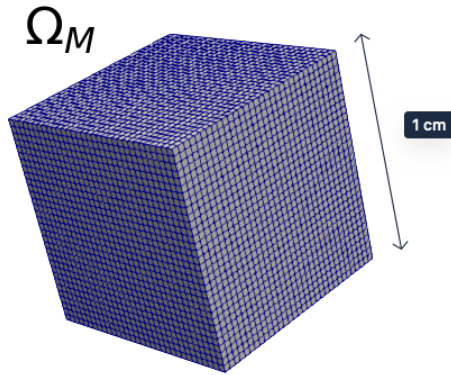


Figure 4.3: Idealized geometry of myocardium Ω_M .

We perform the same simulation of 2.8 s duration with $\Delta t = 10^{-2}$ s and, as described in the last part of Section 2.3.5, we impose null blood velocity an inward/outward flux having expression (2.33), namely spatially homogenous. Thus, also the model output are spatially homogeneous and so only plotted spatially averaged in Figure 4.4, both with the output of the 0D model. As expected, there are no differences in the curves.

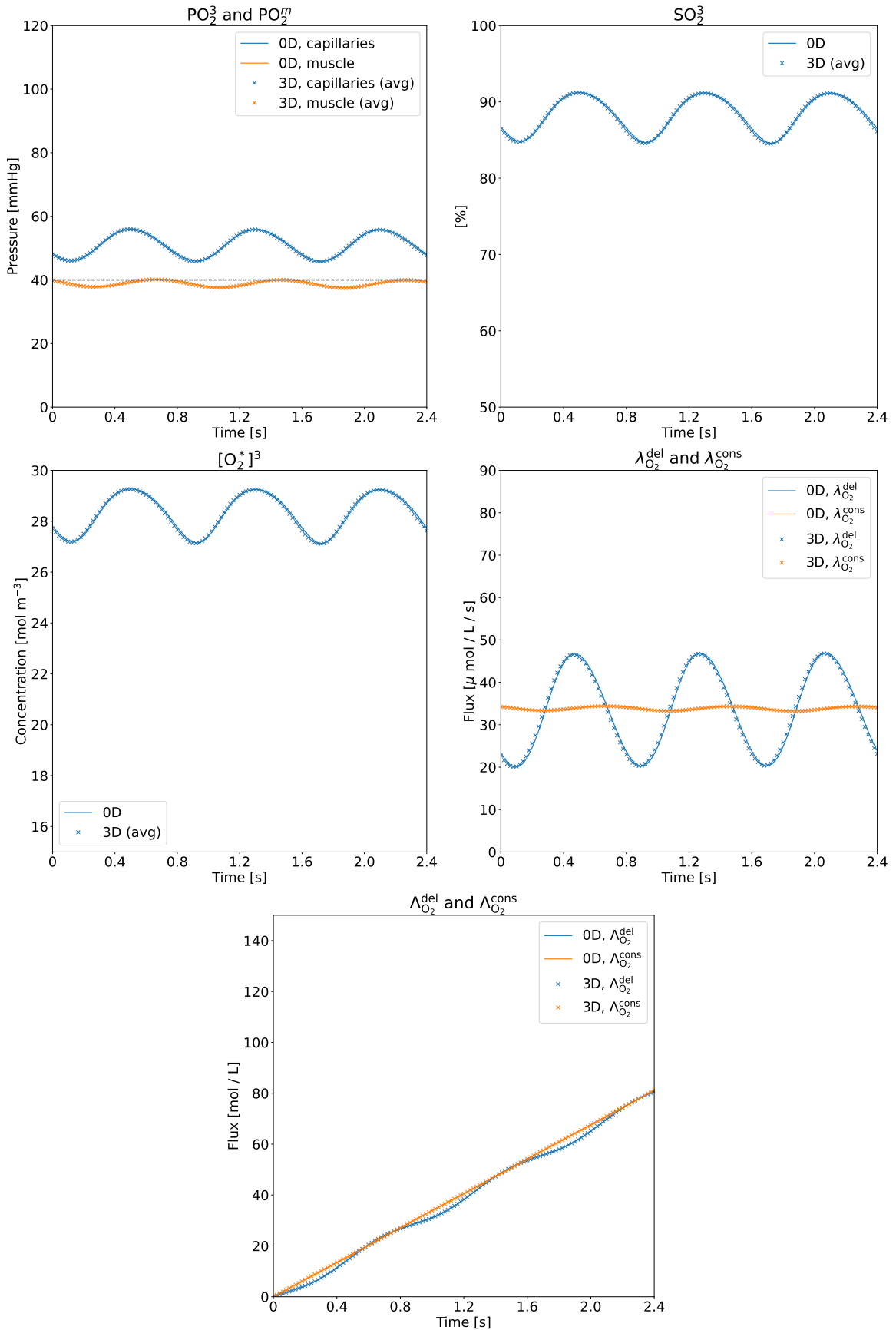


Figure 4.4: Comparison between 3D and 0D model.

4.2.3. Comparison between coupled and uncoupled model

This section shows some tests we implemented and run to validate the coupling between the OE model and the perfusion problem. Firstly, we only coupled the oxygenation model with the perfusion one, in which the coronaries blood dynamics term is directly imposed as a source of the Darcy problem. Finally, we complete the model coupling also with the blood dynamics inside the coronaries.

Comparison without coronaries blood flow

In order to simulate the oxygenation model coupled only with the perfusion model, we need to substitute the outgoing coronary flow rate (2.38), with null blood velocity and the same inward/outward flux (2.33). In this way, we ensure, since the pressure is spatially homogeneous in each compartment, to obtain the same inward and outward fluxes $\hat{\phi}_{2,3}$ and $\hat{\phi}_{3,\text{veins}}$ of the uncoupled model.

As you can see in Figure 4.5, the two simulations of 2.8 s duration with $\Delta t = 10^{-2}$ s and the usual physiological parameters provide almost identical results, meaning that the coupling with the only perfusion model is correct.

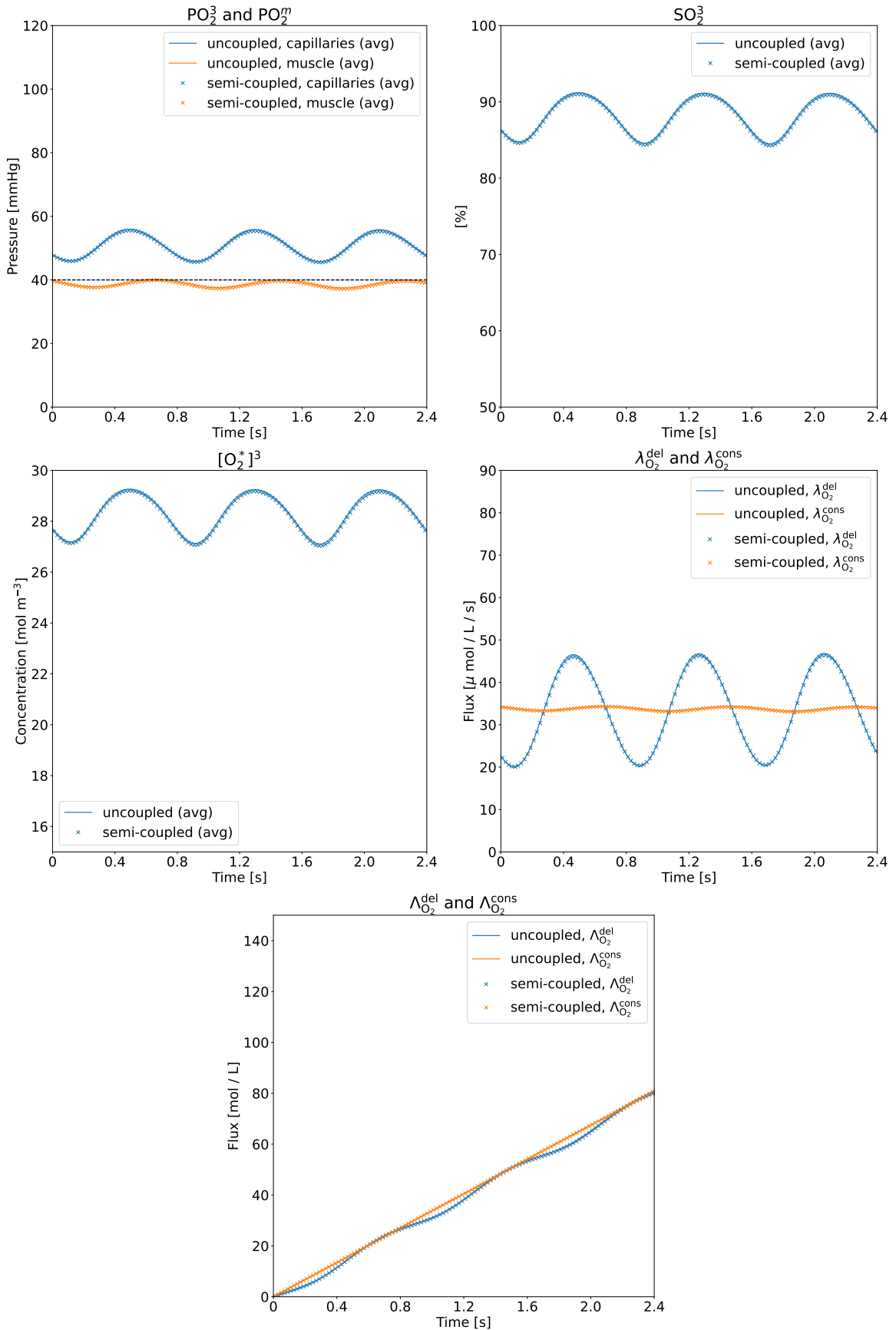


Figure 4.5: Comparison between semi-coupled and uncoupled model.

Comparison with coronaries blood flow

Finally, in this comparison, we also add the coupling conditions with the coronaries, which are idealized by a cylinder of length $l_C = 4 \text{ cm}$ and radius $r_C = 0.25 \text{ cm}$, as in Figure 4.6.

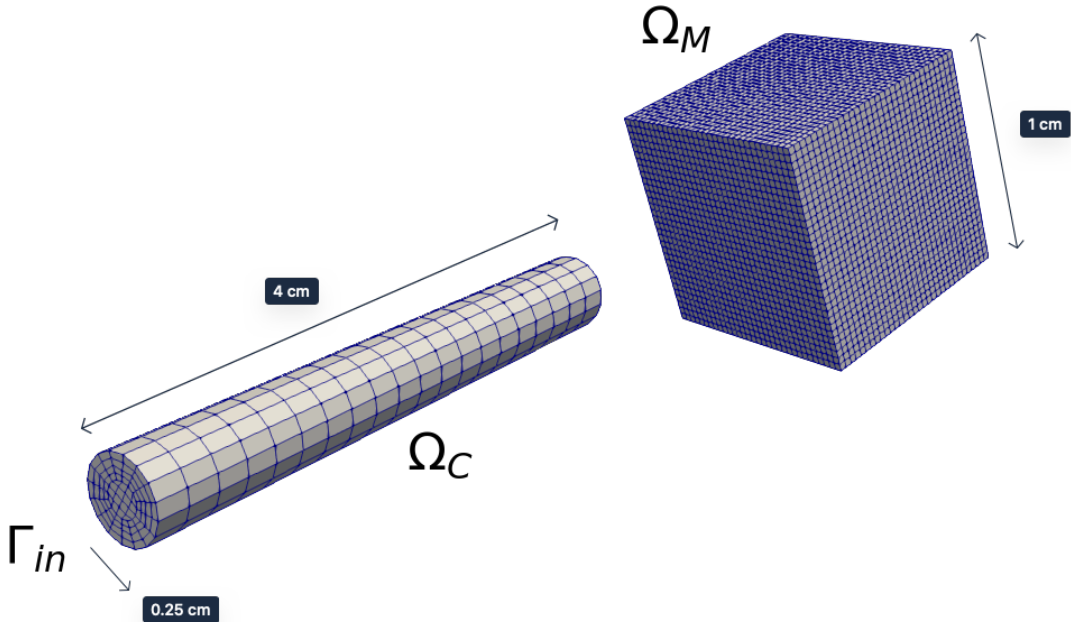


Figure 4.6: Idealized geometries of coronaries Ω_C (cylinder) and myocardium Ω_M (cube).

To ensure the same inward/outward flux (2.33), we imposed Dirichlet condition on the velocity on Γ_{in} . Let (r, θ, z) be the cylindrical spatial coordinate associated with the cylinder Ω_C , in which the boundary Γ_{in} corresponds to $z = 0$. The velocity profile \mathbf{u}_{in} imposed on Γ_{in} has separated space and time dependencies: we use a parabolic profile along radial coordinate r and a sinusoidally pulsatile profile in time t . The expression of \mathbf{u}_{in} is

$$\mathbf{u}_{in}(r, \theta, 0, t) \equiv \begin{bmatrix} 0 \\ 0 \\ 1 - \left(\frac{r}{r_C}\right)^2 \end{bmatrix} \Phi(t), \quad r \in [-r_C, r_C], \theta \in [0, 2\pi], \quad (4.1)$$

where $\Phi(t)$ is equivalent to (2.33) multiplied by $|\Omega_M| = 10^{-6} \text{ m}^3$ since, by coupling condition (2.45f), the flux is distributed on all the volume, but we want to impose a flux per unit volume.

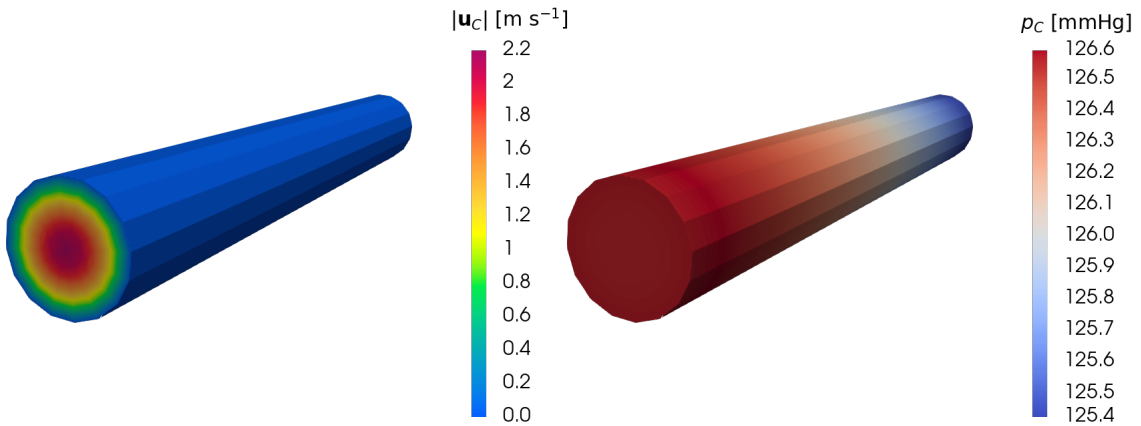


Figure 4.7: Magnitude of \mathbf{u}_C (left) and p_C (right) on Ω_C at peak of the (parabolic) velocity profile ($t = 0.4$ s).

The values of the scalar field p_C and of the magnitude of velocity $|\mathbf{u}_C|$ at $t = 0.4$ s, which corresponds to the peak of the parabolic velocity profile, are depicted in Figure 4.7.

In Figure 4.8 we can see the results of a simulation of 2.8 s duration with $\Delta t = 10^{-2}$ s, one performed with the fully coupled model just described, the other performed with the previously described semi-coupled model. As we can see, the results have a very good matching, confirming that the model is coupled properly with the other physics.

4| Tests and results

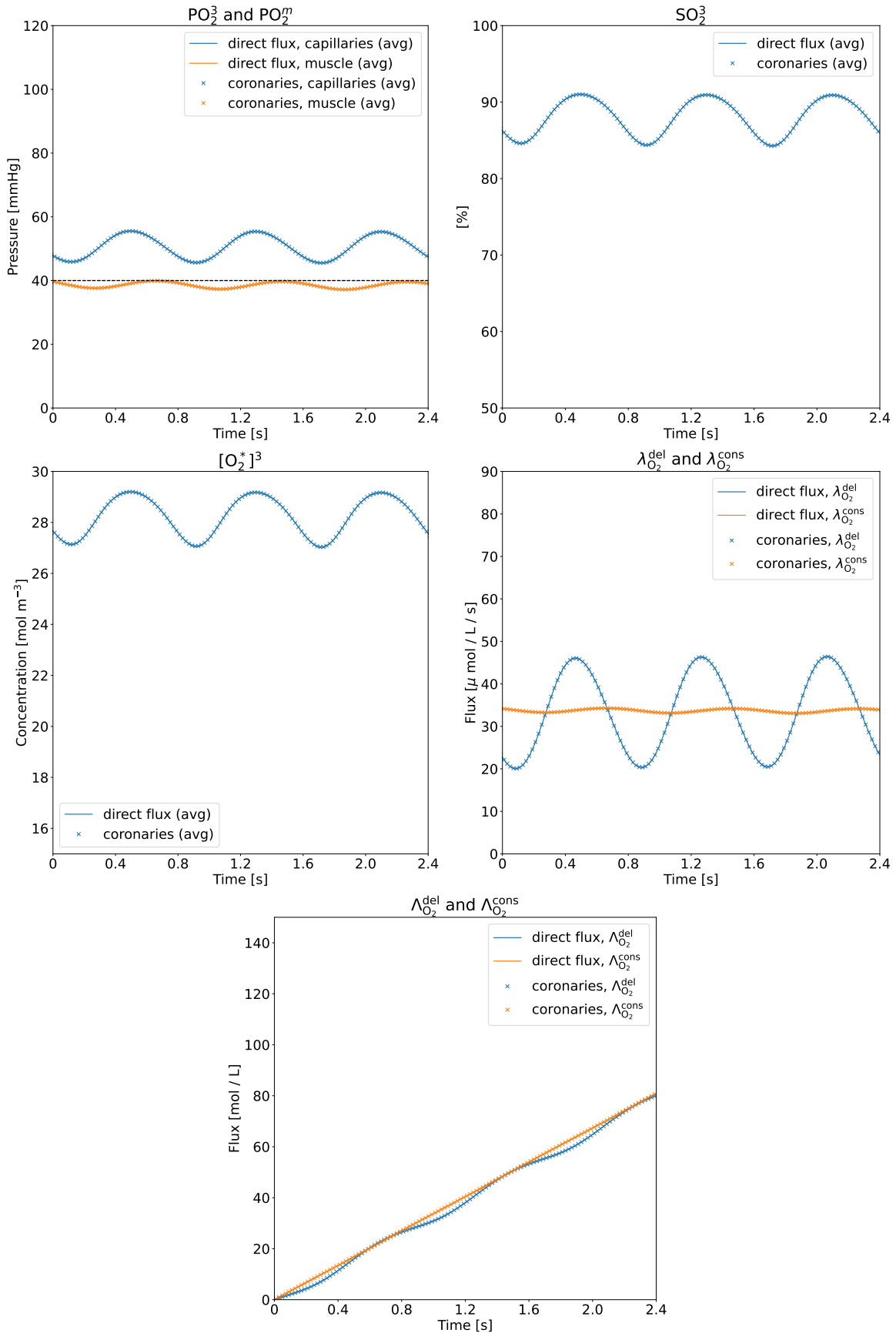


Figure 4.8: Comparison between coupled and semi-coupled model.

4.3. Results on real geometries and discussion

After having validated the model and its implementation in life^x, in this section, we show the main results of this work. We simulated real geometries of coronaries and myocardium in some real-life scenarios, investigating the oxygenation in a patient under both physiological and pathological (i.e., SARS-CoV-2 infection) conditions and the effects of physical activity on both these cases. We discuss

- in Section 4.3.1, the comparison between simulations on real and idealized geometry, to assess if they are particular differences between them or if the idealized geometry can be a good approximation of the real one;
- in Section 4.3.2, the effects of physical activity on a healthy subject;
- in Section 4.3.3, the effects of SARS-CoV-2 infection;
- in Section 4.3.4, we the effects of physical activity on a patient with SARS-CoV-2 infection.

4.3.1. Comparison between real and idealized geometry

We apply the proposed multi-physics computational model in the second numerical test to a realistic 3D human heart geometry. For this purpose, the geometries of the computational domains Ω_C and Ω_M , describing the epicardial coronary arteries and the myocardium of the left and right ventricles, are defined starting from the 3D Human Heart Model provided by Zygote [126] and showed in Figure 4.9. The corresponding computational meshes are composed of 726,982 tetrahedral elements for Ω_C and 214,484 hexahedral elements for Ω_M . The volume of the ventricle is $|\Omega_M| = 1.76 \cdot 10^{-4} \text{ m}^3$, corresponding to 176 mL, in accordance with anatomy [36, 40, 51].

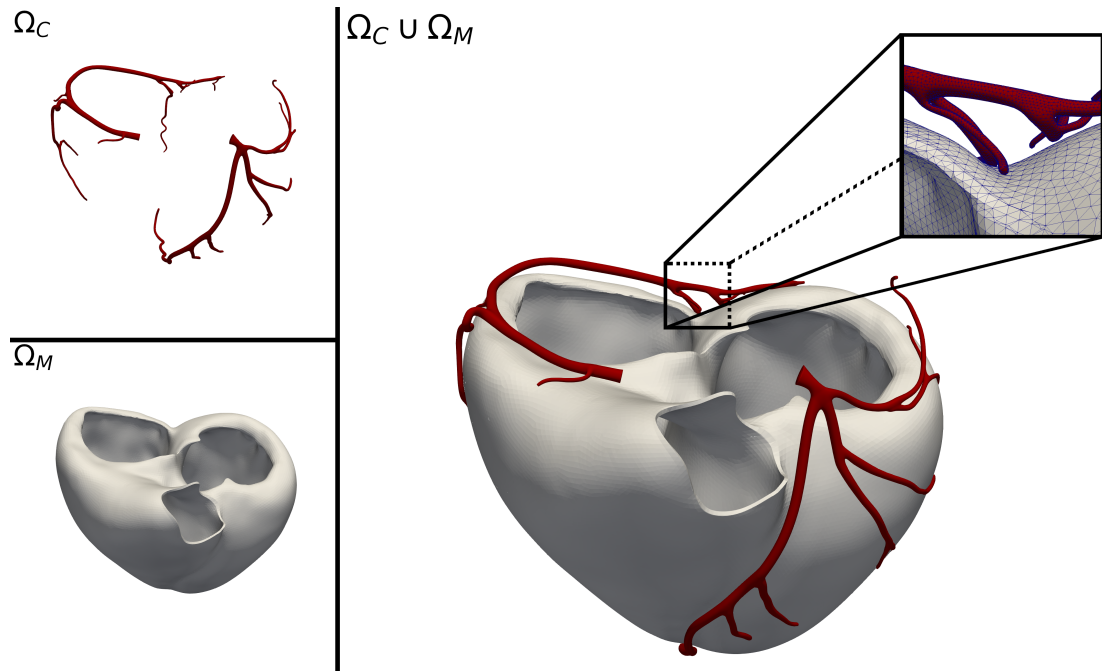


Figure 4.9: Computational domains: coronaries (Ω_C) and myocardium (Ω_M).

The domain Ω_M is partitioned into 17 perfusion regions: the results are shown in Figure 4.10, both with the calibrated parameters [25].

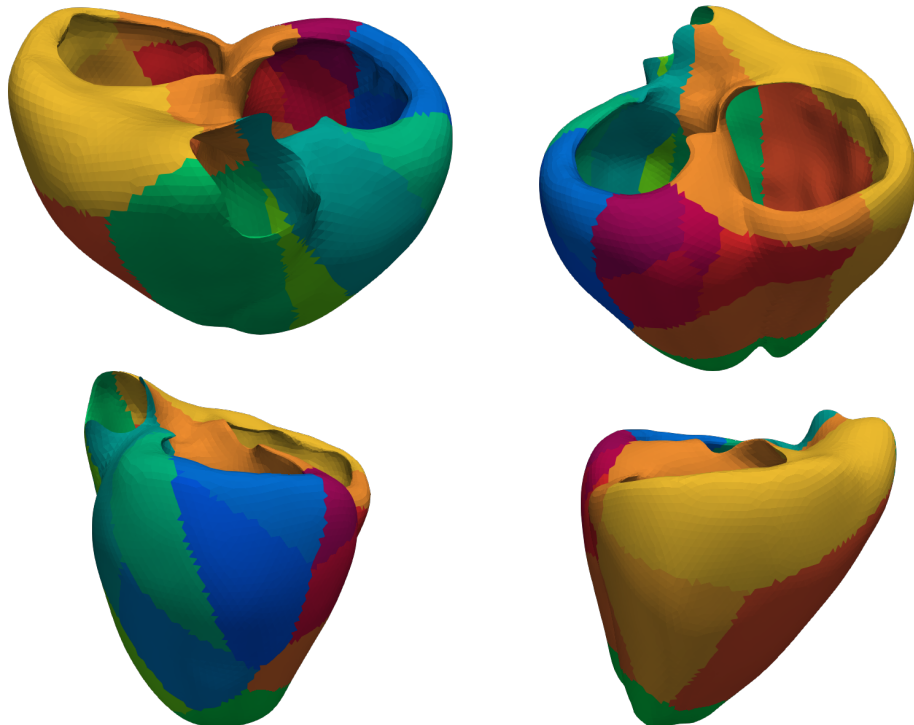


Figure 4.10: Perfusion regions in different myocardium views.

The values of the permeability tensor \mathbf{K}_i and of the pressure-coupling coefficients $\beta_{i,j}$ are taken from [25] and showed in Figure 4.11 and Figure 4.12 respectively.

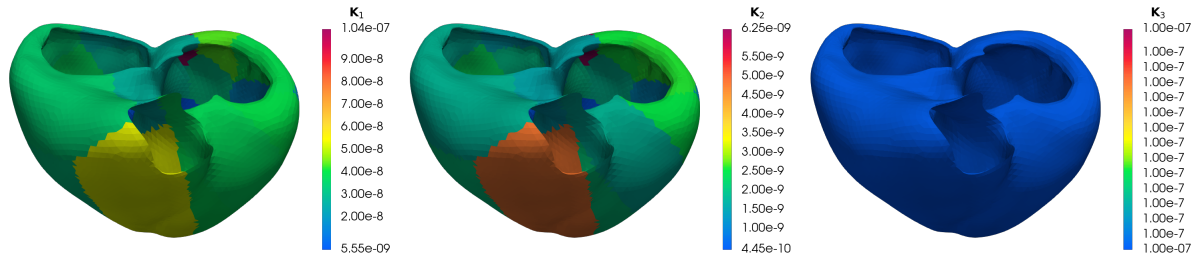


Figure 4.11: Permeability tensors \mathbf{K}_i .

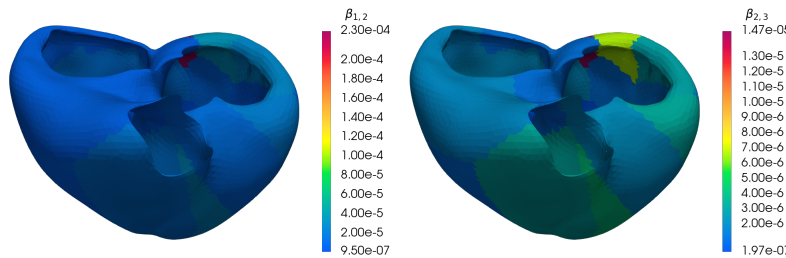


Figure 4.12: Pressure-coupling coefficients $\beta_{i,j}$.

At the inlet sections $\Gamma_{in,k}$, $k = l, r$ of the epicardial left ($k = l$) and right ($k = r$) vessel, we prescribe the flow rate condition

$$\int_{\Gamma_{in,k}} \mathbf{u}_C \cdot \mathbf{n} d\gamma = \Psi_{CBFk}, \quad k = l, r \quad (4.2)$$

with $\Psi_{CBFl} = 0.57\Psi_{CBF}$, $\Psi_{CBFr} = 0.43\Psi_{CBF}$ and Ψ_{CBF} being the inlet CBF with a physiological profile [86] shown in Figure 4.13, also adapted (as explained in the following) to the case of SARS-CoV-2 infection and of a patient under physical activity.

The subdivision of Ψ_{CBF} in Ψ_{CBFl} and Ψ_{CBFr} accounts for percentage of volume perfused by each main epicardial coronary branch as explained in [25]. Thus, we obtain that the peaks reached in $\Gamma_{in,l}$ and $\Gamma_{in,r}$ are $2.28 \cdot 10^{-6} \text{ m}^3 \text{s}^{-1}$ and $1.72 \cdot 10^{-6} \text{ m}^3 \text{s}^{-1}$ respectively, and so the total flux peak is of $4.00 \cdot 10^{-6} \text{ m}^3 \text{s}^{-1}$, corresponding to 4.00 mL s^{-1} . Since the average of the normalized Ψ_{CBF} in one period is 0.51, we have that the total averaged flux to the myocardium is of $2.04 \cdot 10^{-6} \text{ m}^3 \text{s}^{-1}$, namely 2.04 mL s^{-1} . Hence, the average CBF $\bar{\Psi}_{CBF}$ is $2.04 \text{ mL s}^{-1} \cdot 176 \text{ mL} \cdot 60 \text{ s min}^{-1}$, namely $\bar{\Psi}_{CBF} = 0.695 \text{ mL min}^{-1} \text{ g}^{-1}$ (since 1 mL of tissue corresponds to 1 g), in accordance with the literature value of $0.8 \text{ mL min}^{-1} \text{ g}^{-1}$ [24].

In Figure 4.13, the blue, red, and green points denote some notable time instants in the simulation: the beginning of the systole, the beginning of the diastole, and the plateau at the end of the diastole, respectively. For more clarity, they are reported only in the first period, in which the correspondence with time is indicated in Table 4.1.

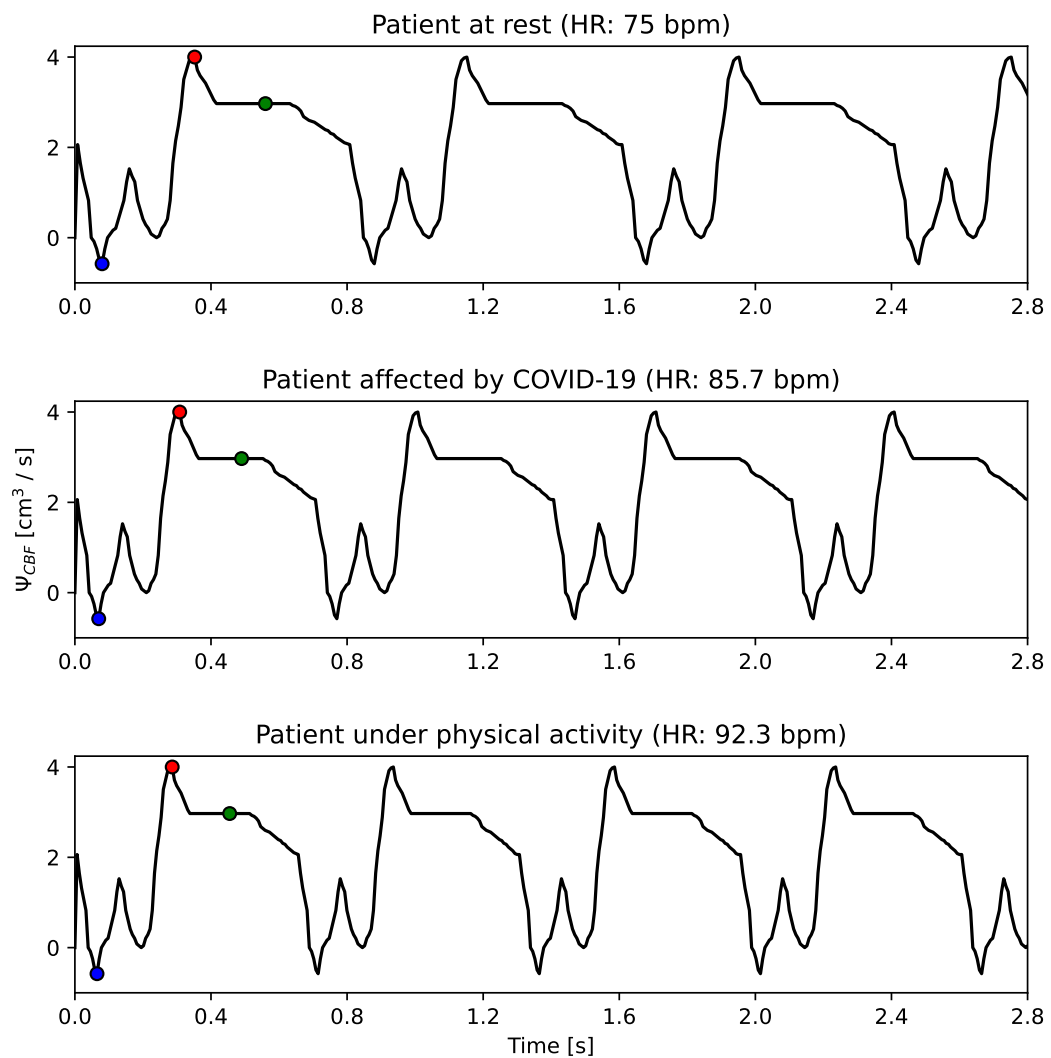


Figure 4.13: Ψ_{CBF} profile imposed in simulated scenarios.

Scenario	Period	HR	Color		
			Blue	Red	Green
Pt. at rest	0.8 s	75 beat min ⁻¹	0.08 s	0.352 s	0.560 s
Pt. with SARS-CoV-2	0.7 s	85.7 beat min ⁻¹	0.070 s	0.308 s	0.490 s
Pt. under p. a.	0.65 s	92.3 beat min ⁻¹	0.065 s	0.286 s	0.455 s

Table 4.1: Correspondences between CBF points and simulation times.

In Figure 4.14, we can see in these time instants the values of p_C in the coronaries and of PO_2^3 , PO_2^m , SO_2^3 and $[\text{O}_2*]^3$ in the myocardium. The tuned initial values of PO_2^3 and PO_2^m are 50 mmHg and 40 mmHg respectively. Notice that the scales of each field are different between the three time steps.

We can observe that at the beginning systole, the pattern of PO_2^3 differs from the other time steps. The fact that the patterns are similar and that there is no large variability in space confirms that the simulation is following the physiology since we are simulating a healthy system of coronaries and myocardium, adequately supplied by the coronaries in each of its points.

For this reason, we can concentrate on the spatially averaged values of the scalar fields, both with the average and total oxygen fluxes, as shown in Figure 4.15. The model seems in good accordance with the literature [24]: values of SO_2^3 oscillates between 85% and 90%, values of PO_2^m are almost constant near the physiological imposed value of 40 mmHg and the average value of $\lambda_{\text{O}_2}^{\text{cons}}$ of 34 $\mu\text{mol L}^{-1} \text{s}^{-1}$, similar to the one available in literature [24, 51].

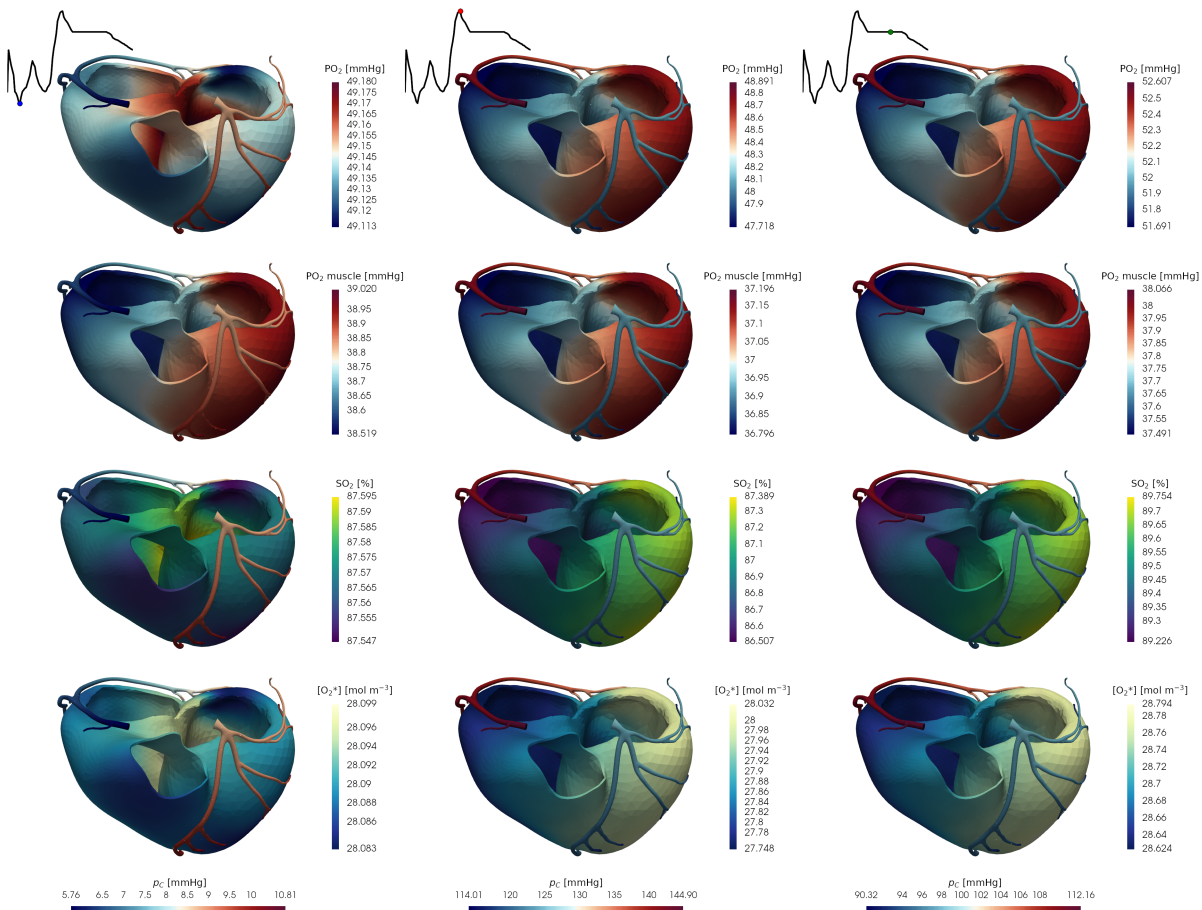


Figure 4.14: Scalar fields of the multi-physics oxygenation model in scenario of a healthy subject.

Finally, we compared the results between real and idealized geometry. The simulation of the idealized geometry is the same as the previous section, and the inward/outward flux was chosen to provide $\bar{\Psi}_{\text{CBF}} = 0.64 \text{ mL min}^{-1} \text{ g}^{-1}$, near to the real one simulated in the coronaries which is $0.695 \text{ mL min}^{-1} \text{ g}^{-1}$ as computed above.

As we can notice, the results are in good accordance, meaning that not only can the idealized geometry be used instead of the real one, but it is also possible to use the 0D model directly. Of course, to do this, one must provide the desired inward/outward flux, which depend on the CBF, which is not available a priori if the goal is to simulate the patient-specific scenario of blood supply of myocardium. Moreover, this is possible only in case of non-pathological tissue: in case spatial heterogeneities, as ischemic regions in myocardium, this would not be possible without properly simulate the fluid dynamics in coronaries and the blood perfusion in the myocardium.

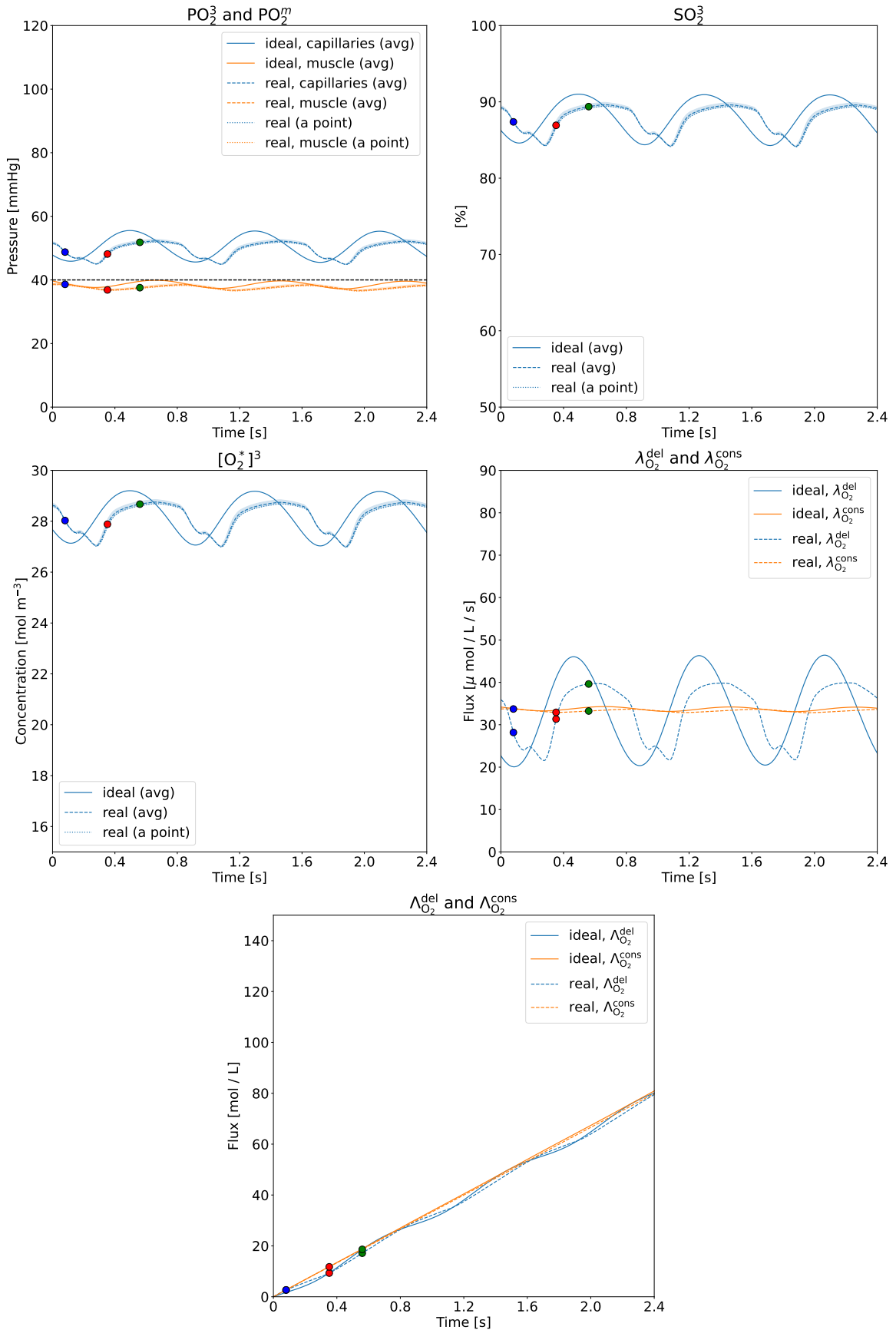


Figure 4.15: Comparison between real and idealized geometries.

4.3.2. Effects of physical activity

We started studying the influence of physical activity, i.e. walking or running, on the model output. In order to do this, we simulated two cases with the default parameters we used also before, but changing the muscle dynamics maximum effective consumption rate: we pass from $\tilde{\xi}_0 = 50 \text{ mmHg s}^{-1}$ for a patient at rest, to $\tilde{\xi}_0 = 130 \text{ mmHg s}^{-1}$ for a patient under physical activity. Moreover, we imposed a heartbeat period of 0.65 s for the patient under physical activity. The initial values of PO_2^3 and PO_2^m are tuned to 42 mmHg and 20 mmHg respectively and in order to make the solutions to be already near to a limit cycle.

In Figure 4.16 we show the scalar fields of this scenarios. Notice that there are no meaningful differences in the patterns since we simulate a healthy tissue. For the same reason, the patterns are similar to the case of patient at rest.

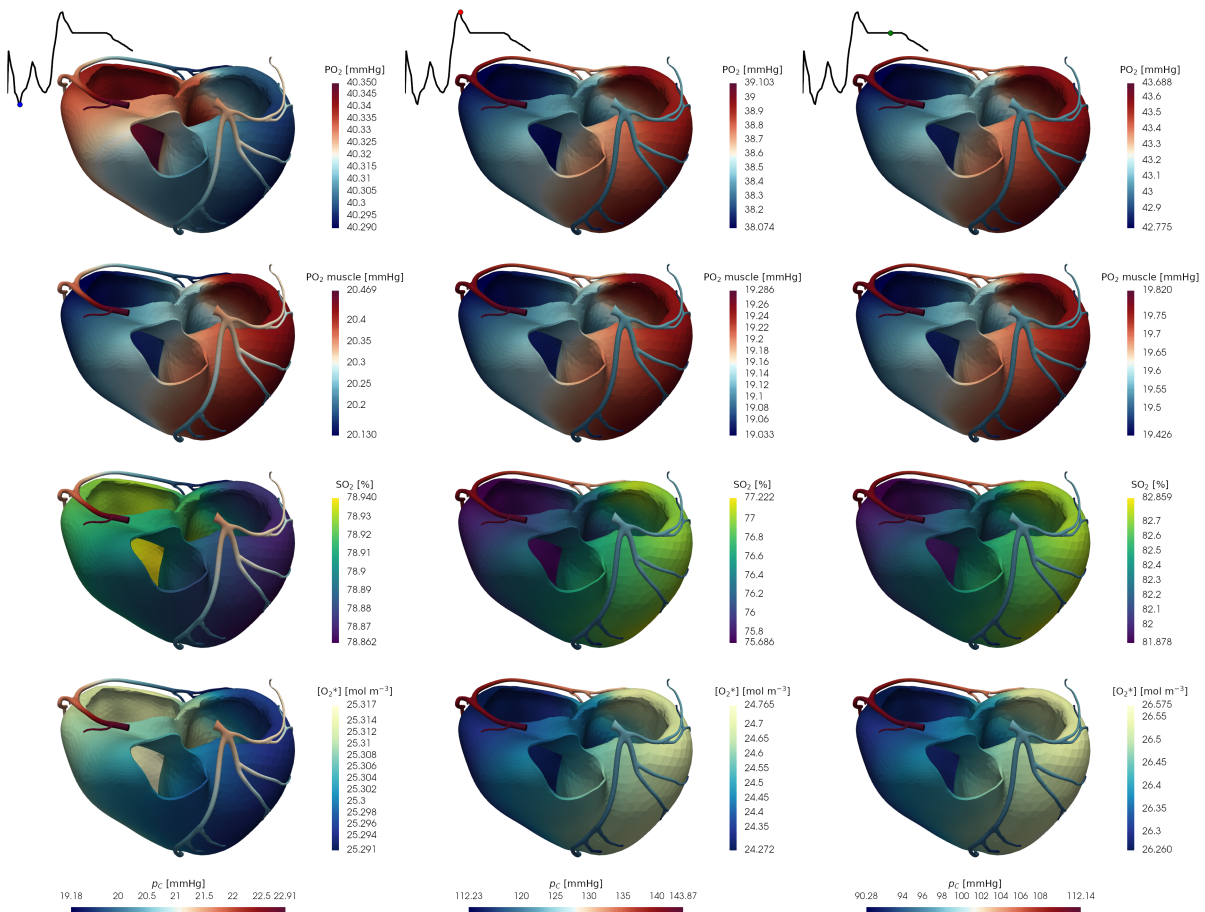


Figure 4.16: Scalar fields of the multi-physics oxygenation model in scenario of a healthy subject under physical activity.

Variable	Measure unit	At rest			Under p. a.		
		min	avg	max	min	avg	max
PO_2^3	mmHg	44.8	49.6	52.8	36.6	41.2	44.4
PO_2^m	mmHg	36.5	37.7	39	18.9	19.8	20.8
SO_2^3	%	84.1	87.8	89.9	73.4	79.9	83.7
$[\text{O}_2*]^3$	mol m^{-3}	27	28.2	28.9	23.5	25.6	26.9
$\lambda_{\text{O}_2}^{\text{del}}$	$\mu\text{mol L}^{-1} \text{s}^{-1}$	21.6	33.1	39.9	47.9	59.4	66.2
$\lambda_{\text{O}_2}^{\text{cons}}$	$\mu\text{mol L}^{-1} \text{s}^{-1}$	32.8	33.3	33.8	57.6	59.1	60.5
$\Lambda_{\text{O}_2}^{\text{del}}$	mol L^{-1}	25.1	63.7	105	46.7	117.5	189.2
$\Lambda_{\text{O}_2}^{\text{cons}}$	mol L^{-1}	26.8	66.8	107	46.8	117.7	188.7

Table 4.2: Comparison between space-temporal minimum, average and maximum values at rest and under physical activity scenarios.

Hence, we show the spatially averaged quantities in Figure 4.17 to better compare the scenarios. Moreover, in Table 4.2 we report more details on the output values.

We see that an increase in the oxygen consumption by the cardiac muscle affects the model output: in particular, we observe a reduction of SO_2^3 , PO_2^3 , and $[\text{O}_2*]^3$ caused by hypotension affecting tissue and organs. The value of PO_2^m is near to the imposed one of 20 mmHg as explained in [51]. The average value of $\lambda_{\text{O}_2}^{\text{cons}}$ rises from $34 \mu\text{mol L}^{-1} \text{s}^{-1}$ of the at rest scenario, to $58 \mu\text{mol L}^{-1} \text{s}^{-1}$, which makes sense since the myocardium needs more oxygen supply from the capillaries to the muscle in order to work properly.

4 | Tests and results

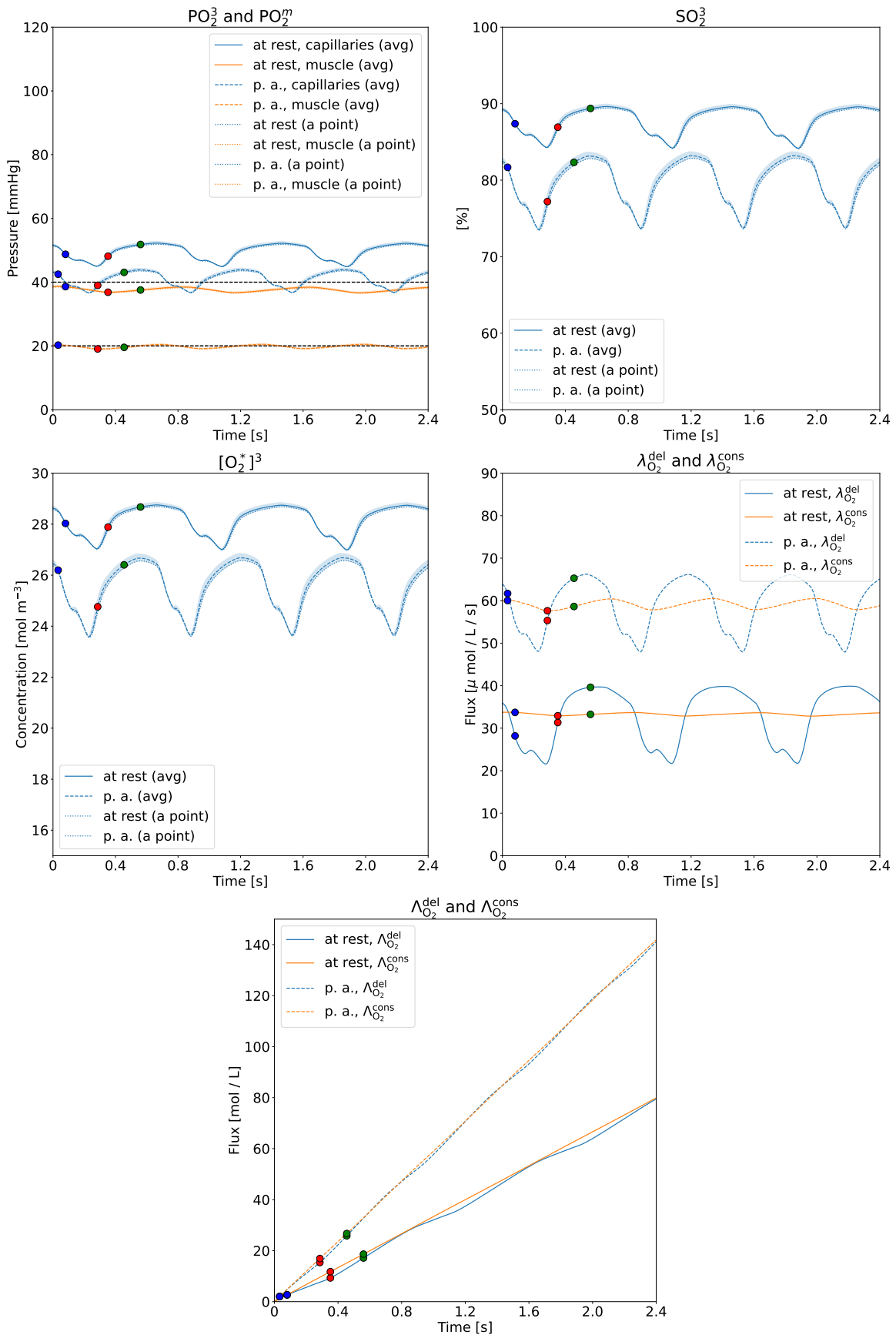


Figure 4.17: Effects of physical activity on a healthy subject.

Variable	Measure unit	Physiological value	Pathological value
SO_2^a	%	0.98	0.92
$[\text{Hb}^*]$	mol m^{-3}	10	8.26
PO_2^{50}	mmHg	26.7	23.4
T_{HB}	s	0.8	0.7

Table 4.3: Pathological parameters to simulate scenario of SARS-CoV-2 infection.

4.3.3. Effects of SARS-CoV-2 infection

Having investigated the scenario of a patient under physical activity, we study in this section the effects of SARS-CoV-2 infection, varying suitable parameters of the model. Hence, we run two simulations with parameters found in the literature for physiological and pathological conditions as in the Table 4.3.

The initial values of PO_2^3 and PO_2^m are tuned quickly reach a limit cycle and are 35 mmHg and 28 mmHg respectively. The value of SO_2^a is the minimum saturation level that has to be reached by providing mechanical ventilation to the patient, while the target saturation level for the patient with SARS-CoV-2, provided by the National Institutes of Health (NIH), is of 92% \div 96% [103]. The value of $[\text{Hb}^*]$ has been selected as the mean value of Hb concentration in SARS-CoV-2 patients computed in the analysis of the Spedali Civili di Brescia, [48] same as the value of the heartbeat period, taken from the same work in which the researchers observed a mean value of cardiac frequency of 85 beat min^{-1} .

We show the results in Figure 4.18, where the model scalar fields are plotted. Although we simulate a pathological case, we do not affect the coronaries or perfusion problem. Thus, the myocardial tissue is healthy and so we do not expect to obtain spatial heterogeneities. Indeed, notice that, as expected, there are no meaningful pattern differences between the scalar fields and with respect to the scenarios previously presented. We use again different time scales to represent the different time instants, so that space variation can be appreciated more.

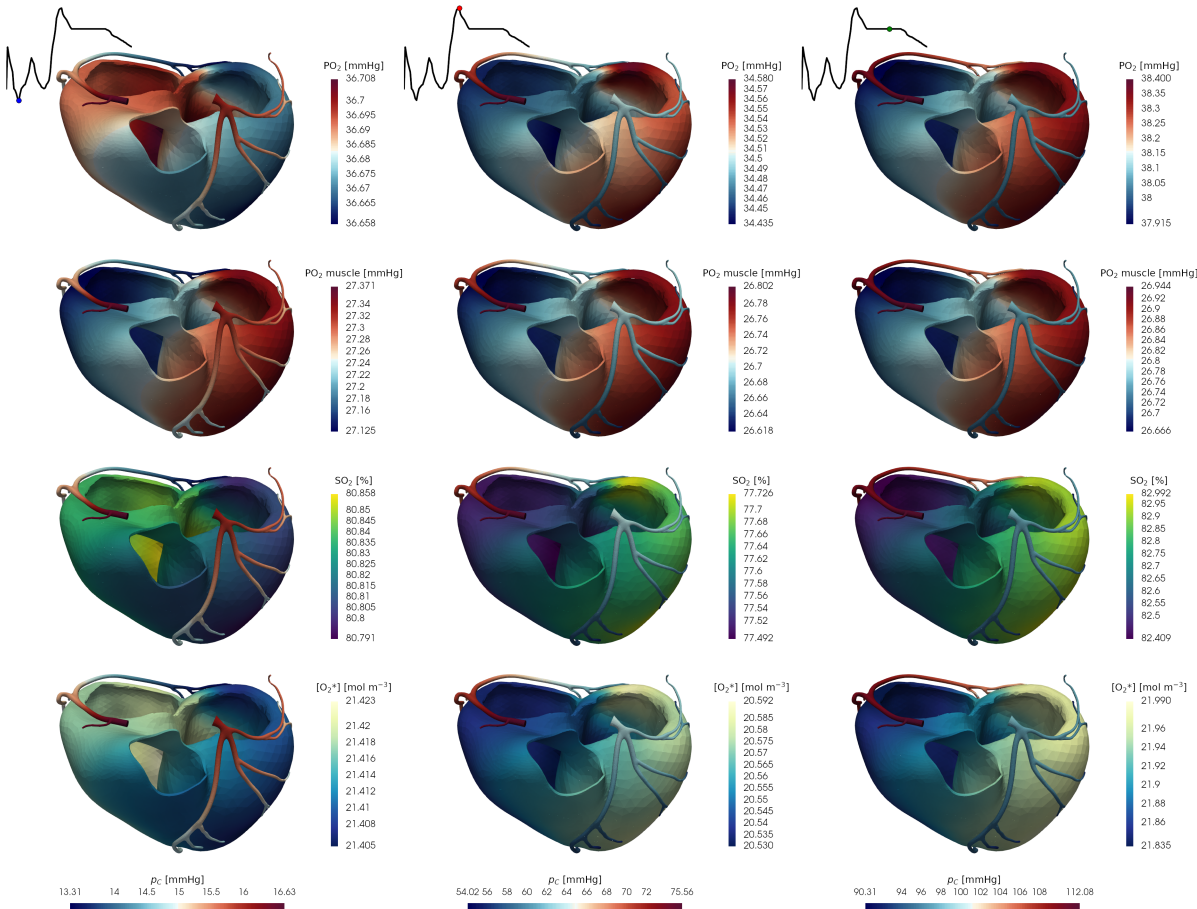


Figure 4.18: Scalar fields of the multi-physics oxygenation model in scenario of patient with SARS-CoV-2.

For this reason, we compare the scenarios showing in Figure 4.19 the spatially averaged quantities, in which we can better analyse the behaviour in time, while in Table 4.4 we can find further details.

Regarding the SO_2^3 , we can see how in the physiological condition, the saturation oscillates between 70% – 95%, while in pathological conditions, between 70% – 89%, hence in a patient with SARS-CoV-2 the curve is lower than for a healthy one. The plots regarding PO_2^3 show a lower magnitude of the curves in the pathological case for both the quantities considered: this confirms the reduction of partial pressure observed in SARS-CoV-2 patients. On the other hand, the oxygen partial pressure in the muscle is not easily measurable in real cases. Hence, although its reduction makes physical sense in a pathological patient, we do not have a corresponding result in the literature. The oxygen concentration in the pathological case shows a lower curve than in the physiological case but with a similar trend. The value of PO_2^m is, in this case, significantly below the physiological one of 40 mmHg.

Variable	Measure	unit	Healthy			SARS-CoV-2		
			min	avg	max	min	avg	max
PO_2^3		mmHg	44.8	49.6	52.8	34.4	37	39
PO_2^m		mmHg	36.5	37.7	39	26.4	27.1	27.8
SO_2^3		%	84.1	87.8	89.9	77.5	81.3	83.8
$[\text{O}_2*]^3$		mol m^{-3}	27	28.2	28.9	20.5	21.5	22.2
$\lambda_{\text{O}_2}^{\text{del}}$		$\mu\text{mol L}^{-1} \text{s}^{-1}$	21.6	33.1	39.9	21.2	27.6	32
$\lambda_{\text{O}_2}^{\text{cons}}$		$\mu\text{mol L}^{-1} \text{s}^{-1}$	32.8	33.3	33.8	27.3	27.7	28.1
$\Lambda_{\text{O}_2}^{\text{del}}$		mol L^{-1}	25.1	63.7	105	20.9	54.1	87.1
$\Lambda_{\text{O}_2}^{\text{cons}}$		mol L^{-1}	26.8	66.8	107	22	55.3	88.6

Table 4.4: Comparison between space-temporal minimum, average and maximum values of healthy and SARS-CoV-2 scenarios.

Finally, regarding the fluxes of oxygen transported from the capillaries to the tissue and used from muscle to produce ATP, we can notice a reduction in both the quantities for a patient with SARS-CoV-2 infection, a difference which becomes larger and larger the more simulation time we consider. The average value of $\lambda_{\text{O}_2}^{\text{cons}}$ drops from $34 \mu\text{mol L}^{-1} \text{s}^{-1}$ of the at rest scenario, to $28 \mu\text{mol L}^{-1} \text{s}^{-1}$, which makes sense since there is minor oxygen availability.

4| Tests and results

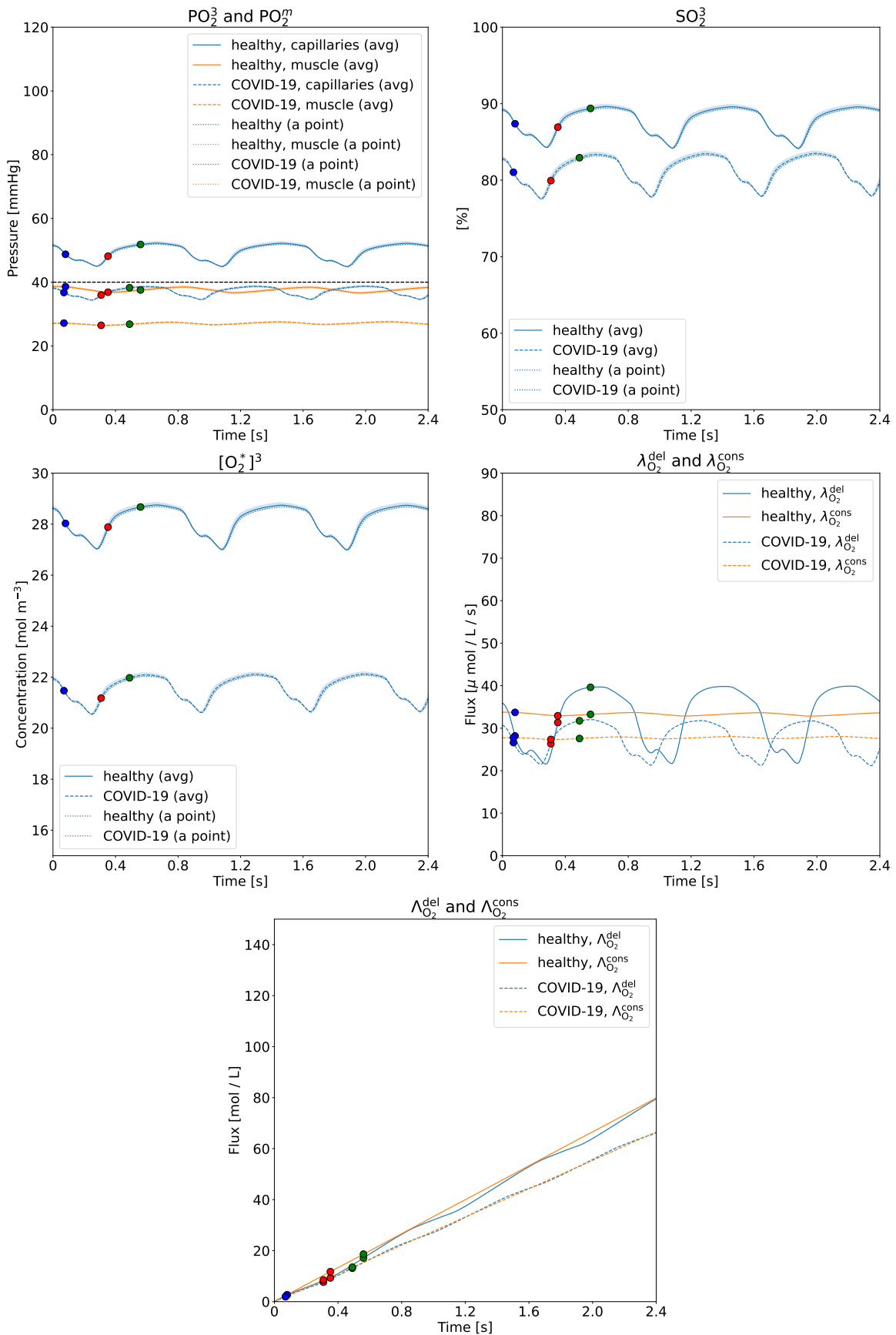


Figure 4.19: Effects of SARS-CoV-2 infection.

4.3.4. Effects of physical activity and SARS-CoV-2 infection

Finally, we study the effects of physical activity on a patient with SARS-CoV-2. In order to do so, we used the pathological parameters listed in Table 4.3 both with $\tilde{\xi}_0 = 130$ mmHg s⁻¹ as done in Section 4.3.2 for the patient under physical activity. The initial values of PO_2^3 and PO_2^m are tuned to quickly reach a limit cycle and are 33 mmHg and 16 mmHg respectively.

Again, as shown in Figure 4.20 and for the reasons described previously, notice that, as expected, there are no meaningful pattern differences in the model output.

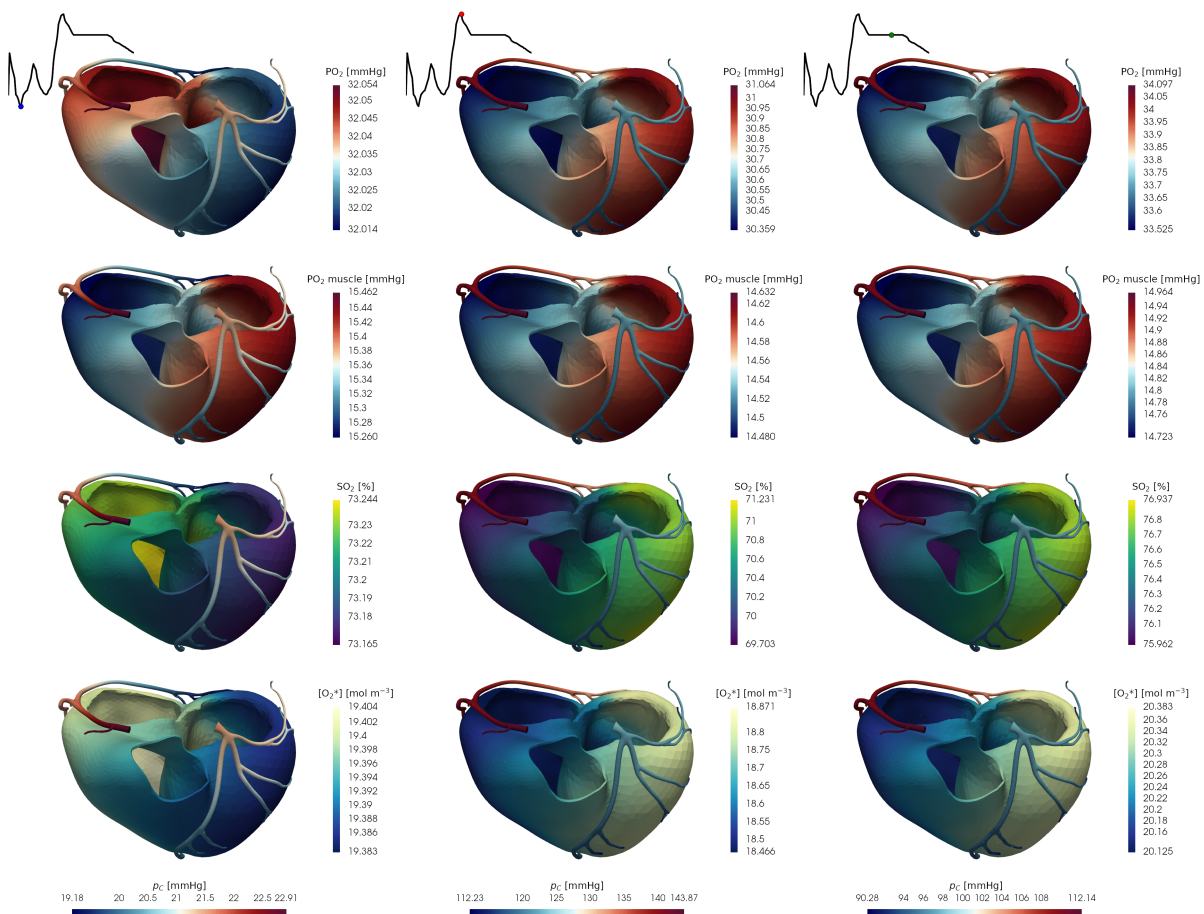


Figure 4.20: Scalar fields of the multi-physics oxygenation model in scenario of a patient with SARS-CoV-2 and under physical activity.

Regarding the spatially averaged quantities, we can find the plots in Figure 4.21, while in Table 4.5 we can find further details on the values of the model output.

4 | Tests and results

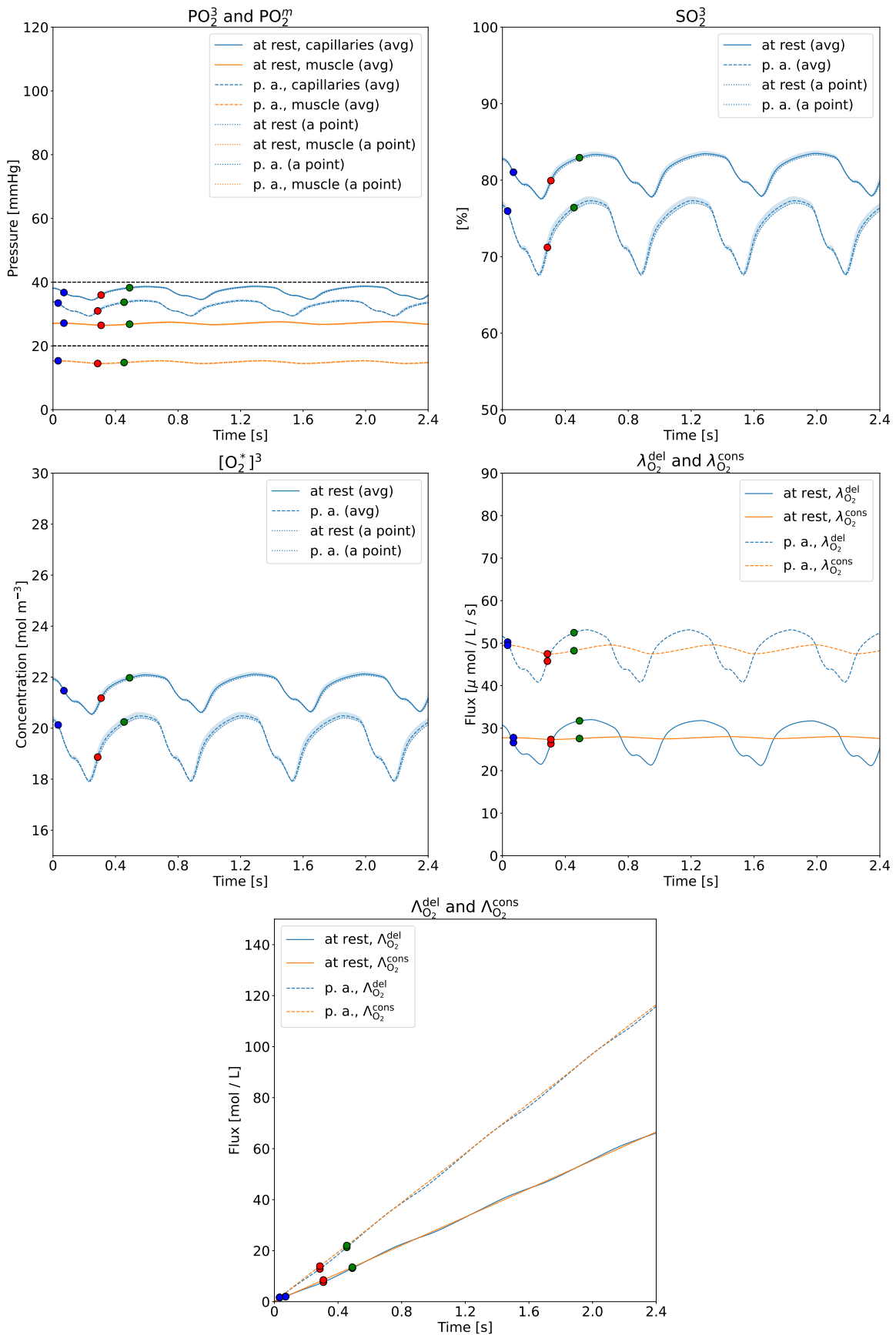


Figure 4.21: Effects of physical activity on a patient with SARS-CoV-2.

Variable	Measure	unit	At rest			Under p. a.		
			min	avg	max	min	avg	max
PO_2^3		mmHg	29.3	32.4	34.6	34.4	37	39
PO_2^m		mmHg	14.4	14.9	15.5	26.4	27.1	27.8
SO_2^3		%	67.5	73.9	77.8	77.5	81.3	83.8
$[\text{O}_2*]^3$		mol m^{-3}	17.9	19.6	20.6	20.5	21.5	22.2
$\lambda_{\text{O}_2}^{\text{del}}$		$\mu\text{mol L}^{-1} \text{s}^{-1}$	40.8	48.6	53.2	21.2	27.6	32
$\lambda_{\text{O}_2}^{\text{cons}}$		$\mu\text{mol L}^{-1} \text{s}^{-1}$	47.5	48.5	49.6	27.3	27.7	28.1
$\Lambda_{\text{O}_2}^{\text{del}}$		mol L^{-1}	37.8	95.8	154.6	20.9	54.1	87.1
$\Lambda_{\text{O}_2}^{\text{cons}}$		mol L^{-1}	39.1	97.3	155.5	22	55.3	88.6

Table 4.5: Comparison between space-temporal minimum, average and maximum values at rest and under physical activity scenarios.

In particular, with respect to a SARS-CoV-2 patient, we can see that, as expected, it has a considerable effect on SO_2^3 , PO_2^3 , PO_2^m , and $[\text{O}_2*]^3$. Also, in this case, we have more delivered oxygen, as explained before. The average value of $\lambda_{\text{O}_2}^{\text{cons}}$ rises from 28 $\mu\text{mol L}^{-1} \text{s}^{-1}$ of the at rest scenario, to 49 $\mu\text{mol L}^{-1} \text{s}^{-1}$, but remaining lower than the value of the healthy subject under physical activity, which was 58 $\mu\text{mol L}^{-1} \text{s}^{-1}$, due to SARS-CoV-2 infection. A patient under SARS-CoV-2 infection, also if apparently in good conditions, has anyway a smaller oxygen reserve: thus starting to perform physical activity can be particularly dangerous since it can suddenly provide oxygen deficit.

5 | Conclusions and further developments

In this work, an innovative oxygenation model was derived, describing the biological parameters involved. The model was coupled with the other physics of blood dynamics in epicardial coronary arteries and intramural coronary vessels. Then, it was discretized in 0D and 3D cases, and implemented inside the high-performance computing library `lifex`, developed within the iHEART project. The implementation leverages on a Runge-Kutta scheme and the FEM for the 0D and 3D case, respectively, and it allows to use of the model by itself or coupled with the other physics through numerical schemes. We performed numerical tests which validated the solver both in uncoupled and coupled form. In this context, we also tuned some physical parameters to improve the model's accordance with the literature and to make the model solutions quickly reach a limit cycle. Finally, we used the coupled model to simulate some real-life scenarios of realistic coronaries and myocardium geometries. The model allows for simulating blood dynamics in epicardial coronary arteries that perfuses the myocardium porous medium, which idealizes the intramural coronary vessels, and finally to obtain the spatial-temporal evolution of the oxygenation values in the myocardium capillaries. This pipeline provided very detailed information about the oxygenation level in the patient. It allowed us to study the differences between a healthy subject and a patient with Sars-CoV-2 infection and assess the effect of physical activity on both of these patients. The results of these comparisons appeared to be in great accordance with the literature confirming the model's soundness. The results of these comparisons appeared to be in great accordance with the literature confirming the model's soundness and showed to which parameters the model is most sensitive.

This work intends to be a little piece of the more significant iHEART project, which represents one of the first attempts in the world to create a complete mathematical model of the human heart, including all the physiological processes that together form the complexity that we call life: i.e., the electrical, mechanical and fluid-dynamic processes and the electro-chemical one, at the cellular level. The ultimate goal is to build a virtual model

of the heart that can describe the interactions that occur within it not only minutely but also possibly predict the dynamics, to build a tool capable of helping clinicians study the genesis and treatment of cardiovascular diseases. Possessing an integrated model of cardiovascular processes could improve prevention, treatment, and cardiac surgery. Thus, iHEART can be assimilated into a virtual microscope, where cardiovascular diseases and their evolution are seen through complex equations that the research team aims to solve.

This work can lead to many future developments and further research. The Michaelis-Menten model for muscle dynamics is a good but simple approximation of the real phenomenon. Hence, a possible improvement could be to couple the oxygenation model with a model for cellular metabolism to improve the accuracy of the muscle dynamics modeling. The latter one, in turn, can be coupled with another model describing how the stored energy can be transformed in work to make the muscle contract. We could also use the results of the oxygenation model to improve the physical accuracy of other models: as an instance, instead of assuming an optimal value of oxygen concentration in the blood, a fluid dynamics problem could use the real one provided by the oxygenation model. This way, the fluid viscosity is better estimated, so the simulation reaches better accuracy.

Although we simulated a pathological scenario, the disease only impacted the oxygenation model. Hence the myocardial tissue remained healthy, so there were no spatial heterogeneities. It would be interesting to study the differences in oxygenation curves when the myocardium presents some ischemic regions or in the case of some coronaries syndromes. Finally, another possible goal would be to use this multi-physics model on patient-specific geometries of coronaries and myocardium, to provide each patient with a digital-twin that helps diagnose and predict complex pathologies.

Bibliography

- [1] P. C. Africa. life^x: a flexible, high performance library for the numerical solution of complex finite element problems, 2022. URL <https://lifex.gitlab.io/>. (cit. on pp. i, iii, 53)
- [2] B. V. Alexeev. Chapter 7 - numerical simulation of vortex gas flow using the generalized euler equations. In B. V. Alexeev, editor, *Generalized Boltzmann Physical Kinetics*, pages 241–286. Elsevier, Amsterdam, 2004. ISBN 978-0-444-51582-7. doi: 10.1016/B978-044451582-7/50033-3. (cit. on pp. 18)
- [3] D. Algranati, G. S. Kassab, and Y. Lanir. Mechanisms of myocardiumcoronary vessel interaction. *American Journal of Physiology-Heart and Circulatory Physiology*, 298(3):861–873, 2010. (cit. on pp. 19)
- [4] P. F. Antonietti, J. De Ponti, L. Formaggia, and A. Scotti. Preconditioning techniques for the numerical solution of flow in fractured porous media. *Journal of Scientific Computing*, 86(1):2, 2020. doi: 10.1007/s10915-020-01372-0. (cit. on pp. 62)
- [5] D. Arndt, W. Bangerth, M. Feder, M. Fehling, R. Gassmöller, T. Heister, L. Heltai, M. Kronbichler, M. Maier, P. Munch, J.-P. Pelteret, S. Sticko, B. Turcksin, and D. Wells. The deal.II Library, Version 9.4. *Journal of Numerical Mathematics*, 0 (0), 2022. doi: doi:10.1515/jnma-2022-0054. (cit. on pp. 53)
- [6] C. J. Arthurs. A mathematical model of coronary blood flow control: simulation of patient-specific three-dimensional hemodynamics during exercise. *American Journal of Physiology-Heart and Circulatory Physiology*, 310(9):1242–1258, 2016. (cit. on pp. 19)
- [7] T. Arts and R. S. Reneman. Interaction between intramyocardial pressure (IMP) and myocardial circulation. *Journal of Biomechanical Engineering*, 107(1):51–56, 1985. (cit. on pp. 19)
- [8] F. Baldissera and C. A. Porro. *Fisiologia e biofisica medica*. Poletto, 2009. (cit. on pp. 4, 16)

- [9] N. Barnafi. Mathematical analysis and numerical approximation of a general linearized poro-hyperelastic model. *Computers & Mathematics with Applications*, 2020. (cit. on pp. 22)
- [10] N. Barnafi, P. Zunino, L. Dedè, and A. Quarteroni. Mathematical analysis and numerical approximation of a general linearized poro-hyperelastic model. *Computers & Mathematics with Applications*, 91:202–228, 2021. (cit. on pp. 20)
- [11] K. E. Barrett et al. *Ganong's review of medical physiology*. McGraw-Hill Education, 2012. (cit. on pp. 4)
- [12] D. Beard and J. Bassingthwaigte. Modeling advection and diffusion of oxygen in complex vascular networks. *Annals of biomedical engineering*, 29:298–310, 05 2001. doi: 10.1114/1.1359450. (cit. on pp. 30)
- [13] M. A. Biot. General theory of three-dimensional consolidation. *Journal of applied physics*, 12(2):155–164, 1941. (cit. on pp. 21)
- [14] W. F. Boron and E. L. Boulpaep. *Medical Physiology: A Cellular and Molecular Approach*. Elsevier health sciences, 2012. (cit. on pp. 16)
- [15] P. H. M. Bovendeerd. Dependence of intramyocardial pressure and coronary flow on ventricular loading and contractility: A model study. *Annals of Biomedical Engineering*, 34(12):1833–1845, 2006. (cit. on pp. 19)
- [16] Britannica. Hemoglobin, 2022. URL <https://bit.ly/3TcpoCv>. [Online, accessed in September 2022]. (cit. on pp. 10)
- [17] B. Burtschell, P. Moireau, and D. Chapelle. Numerical analysis for an energy-stable total discretization of a poromechanics model with inf-sup stability. *Acta Mathematicae Applicatae Sinica, English Series*, 35(1):28–53, 2019. (cit. on pp. 21, 22)
- [18] R. J. Cerci et al. Aligning coronary anatomy and myocardial perfusion territories. *Circulation: Cardiovascular Imaging*, 5(5):587–595, 2012. (cit. on pp. 14)
- [19] M. D. Cerqueira et al. Standardized myocardial segmentation and nomenclature for tomographic imaging of the heart. *Circulation*, 105(4):539–542, 2002. (cit. on pp. 14, 15)
- [20] D. Chapelle and P. Moireau. General coupling of porous flows and hyperelastic formulations—from thermodynamics principles to energy balance and compatible

- time schemes. *European Journal of Mechanics-B/Fluids*, 46:82–96, 2014. (cit. on pp. 21)
- [21] A. N. Cookson. A novel porous mechanical framework for modelling the interaction between coronary perfusion and myocardial mechanics. *Journal of Biomechanics*, 45(5):850–855, 2012. (cit. on pp. 21, 23, 33)
- [22] A. N. Cookson. A spatially-distributed computational model to quantify behaviour of contrast agents in mr perfusion imaging. In *Medical image analysis*. Medical image analysis, 2014. (cit. on pp. 22)
- [23] R. K. Dash and J. B. Bassingthwaigte. Blood HbO₂ and HbCO₂ dissociation curves at varied O₂, CO₂, pH, 2,3-DPG and temperature levels. *Annals of Biomedical Engineering*, 32:1676–1693, 2004. (cit. on pp. 24)
- [24] Deranged Physiology. Myocardial oxygen supply and demand, 2020. URL <https://bit.ly/3AqzuXJ>. [Online, accessed in September 2022]. (cit. on pp. 67, 79, 81)
- [25] S. Di Gregorio, M. Fedele, G. Pontone, A. F. Corno, P. Zunino, C. Vergara, and A. Quarteroni. A multiscale computational model of myocardial perfusion in the human heart. *MOX Report 2019/48, Politecnico di Milano*, 2019. (cit. on pp. 6, 14, 15, 17, 31, 32, 33, 34, 36, 53, 61, 62, 78, 79, 109)
- [26] J. M. Downey and E. S. Kirk. Inhibition of coronary blood flow by a vascular waterfall mechanism. *Circulation Research*, 36(6):753 –760, 1975. (cit. on pp. 18)
- [27] Z. Duanmu. A patient-specific lumped-parameter model of coronary circulation. *Scientific Reports*, 8(1), 2018. (cit. on pp. 18)
- [28] M. Fedele. A patient-specific aortic valve model based on moving resistive immersed implicit surfaces. *Biomechanics and Modeling in Mechanobiology*, 16(5):1779–1803, 2017. (cit. on pp. 53)
- [29] L. Formaggia and C. Vergara. Prescription of general defective boundary conditions in fluid-dynamics. *Milan Journal of Mathematics*, 80(2):333–350, 2012. (cit. on pp. 50)
- [30] D. Forti and L. Dedè. Semi-implicit BDF time discretization of the Navier–Stokes equations with VMS-LES modeling in a high performance computing framework. *Computers & Fluids*, 117:168–182, 2015. (cit. on pp. 53)
- [31] X. Ge. A multi-scale model of the coronary circulation applied to investigate trans-

- mural myocardial flow. *International Journal for Numerical Methods in Biomedical Engineering*, 34(10):3123, 2018. (cit. on pp. 19)
- [32] D. Goldman. Theoretical models of microvascular oxygen transport to tissue. *Microcirculation*, 15(8):795–811, 2008. doi: 10.1080/10739680801938289. PMID: 18608981. (cit. on pp. 17, 23, 24, 26, 27, 28, 29)
- [33] D. Goldman and A. S. Popel. A computational study of the effect of capillary network anastomoses and tortuosity on oxygen transport. *Journal of Theoretical Biology*, 206(2):181–194, 2000. ISSN 0022-5193. doi: 10.1006/jtbi.2000.2113. (cit. on pp. 30)
- [34] A. G. Goodwill et al. Regulation of coronary blood flow. *Comprehensive Physiology* 7.2, pages 321–382, 2011. (cit. on pp. 14, 16, 19)
- [35] S. Goutelle, M. Maurin, F. Rougier, X. Barbaut, L. Bourguignon, M. Ducher, and P. Maire. The Hill equation: a review of its capabilities in pharmacological modelling. *Fundamental & Clinical Pharmacology*, 22(6):633–648, 2008. doi: 10.1111/j.1472-8206.2008.00633.x. (cit. on pp. 44)
- [36] H. Gray and S. Standring. *Gray's anatomy: the anatomical basis of clinical practice*, 2008. (cit. on pp. 1, 3, 4, 77)
- [37] K. Groebe. A versatile model of steady state O₂ supply to tissue. application to skeletal muscle. *Biophysical journal*, 57(3):485—498, March 1990. ISSN 0006-3495. doi: 10.1016/s0006-3495(90)82565-0. (cit. on pp. 29)
- [38] K. Groebe and G. Thews. Role of geometry and anisotropic diffusion for modelling PO₂ profiles in working red muscle. *Respiration Physiology*, 79(3):255–278, 1990. ISSN 0034-5687. doi: 10.1016/0034-5687(90)90131-H. (cit. on pp. 29)
- [39] J. E. Hall and M. E. Hall. Guyton and hall textbook of medical physiology, 2020. (cit. on pp. 6, 109)
- [40] J. T. Hansen. *Netter's Anatomy Flash Cards - 4th Edition*, 2014. (cit. on pp. 1, 3, 4, 77, 109)
- [41] J. D. Hellums, P. K. Nair, N. S. Huang, and N. Ohshima. Simulation of intraluminal gas transport processes in the microcirculation. *Annals of Biomedical Engineering*, 24:1–24, 2007. (cit. on pp. 23, 24)
- [42] M. R. Hestenes and E. Stiefel. Methods of conjugate gradients for solving linear

- systems. *Journal of research of the National Bureau of Standards*, 49:409–435, 1952. (cit. on pp. 62)
- [43] T. P. Hoef et al. Non-hyperaemic coronary pressure measurements to guide coronary interventions. *Nature Reviews Cardiology*, pages 1–12, 2020. (cit. on pp. 16)
- [44] J. Huyghe and D. Campen. Finite deformation theory of hierarchically arranged porous solids—I. balance of mass and momentum. *International Journal of Engineering Science*, 33(13):1861–1871, 1995. (cit. on pp. 21)
- [45] J. M. Huyghe. Porous medium finite element model of the beating left ventricle. *American Journal of Physiology-Heart and Circulatory Physiology*, 262(4):1256–1267, 1992. (cit. on pp. 21)
- [46] J. M. Huyghe and D. H. Campen. Finite deformation theory of hierarchically arranged porous solids—II. constitutive behaviour. *International journal of engineering science*, 33(13):1873–1886, 1995. (cit. on pp. 21)
- [47] E. R. Hyde. Multi-scale parameterisation of a myocardial perfusion model using whole-organ arterial networks. *Annals of Biomedical Engineering*, 42(4):797–811, 2014. (cit. on pp. 21, 23, 33, 34)
- [48] R. M. Inciardi et al. Characteristics and outcomes of patients hospitalized for Covid-19 and cardiac disease in northern italy. *European Heart Journal*, 41(19):1821–1829, 2020. (cit. on pp. 87)
- [49] J. Jacobs, D. Algranati, and Y. Lanir. Lumped flow modeling in dynamically loaded coronary vessels. *Journal of Biomechanical Engineering*, 130(5), 2008. (cit. on pp. 18, 19)
- [50] M. S. Javadi et al. Definition of vascular territories on myocardial perfusion images by integration with true coronary anatomy: A hybrid PET/CT analysis. *Journal of Nuclear Medicine*, 51(2):198–203, 2010. (cit. on pp. 14)
- [51] G. Jenkins, C. Kemnitz, and G. J. Tortora. *Anatomy and Physiology: From Science to Life—Second (2nd) Edition*. Wiley, 2009. (cit. on pp. 1, 2, 3, 4, 5, 7, 8, 10, 13, 38, 44, 46, 67, 77, 81, 85)
- [52] G. Kassab. *Coronary Circulation*. Springer, 2019. (cit. on pp. 3)
- [53] H. J. Kim. Patient-specific modeling of blood flow and pressure in human coronary arteries. *Annals of biomedical engineering*, 38(10):3195–3209, 2010. (cit. on pp. 23)
- [54] H. Y. Kim et al. Physiological severity of coronary artery stenosis depends on the

- amount of myocardial mass subtended by the coronary artery. *JACC: Cardiovascular Interventions*, 9(15):1548–1560, 2016. (cit. on pp. 14)
- [55] J. P. Kirkpatrick, D. M. Brizel, and M. W. Dewhirst. A mathematical model of tumor oxygen and glucose mass transport and metabolism with complex reaction kinetics. *Radiation Research*, 159(3):336–344, 2003. ISSN 00337587, 19385404. (cit. on pp. 28)
- [56] R. E. Klabunde. Cardiovascular Physiology Concepts, 2008. URL <https://bit.ly/3wrbfrk>. [Online, accessed in September 2022]. (cit. on pp. 17)
- [57] B. Klitzman, A. S. Popel, and B. R. Duling. Oxygen transport in resting and contracting hamster cremaster muscles: Experimental and theoretical microvascular studies. *Microvascular Research*, 25(1):108–131, 1983. ISSN 0026-2862. doi: 10.1016/0026-2862(83)90047-X. (cit. on pp. 29)
- [58] A. Krogh. The number and distribution of capillaries in muscles with calculations of the oxygen pressure head necessary for supplying the tissue. *The Journal of Physiology*, 52, 1919. (cit. on pp. 23, 25)
- [59] A. Kurata et al. Quantification of the myocardial area at risk using coronary CT angiography and Voronoi algorithm-based myocardial segmentation. *European Radiology*, 25(1):49–57, 2014. (cit. on pp. 14)
- [60] T. D. Lagerlund and P. A. Low. Axial diffusion and Michaelis-Menten kinetics in oxygen delivery in rat peripheral nerve. *American Journal of Physiology-Regulatory, Integrative and Comparative Physiology*, 260(2):R430–R440, 1991. doi: 10.1152/ajpregu.1991.260.2.R430. PMID: 1996727. (cit. on pp. 26, 28, 43)
- [61] J. Lee. In silico coronary wave intensity analysis: application of an integrated one-dimensional and poromechanical model of cardiac perfusion. *Biomechanics and Modeling in Mechanobiology*, 15(6):1535–, 2016. (cit. on pp. 21, 23)
- [62] J. Lee and N. P. Smith. The multi-scale modelling of coronary blood flow. *Annals of biomedical engineering*, 40(11):2399–2413, 2012. (cit. on pp. 14, 17, 19)
- [63] J. Lee et al. Multiscale modelling of cardiac perfusion. *Modeling the heart and the circulatory system*, pages 51–96, 2015. (cit. on pp. 17)
- [64] Z. Li, T. Yipintsoi, and J. B. Bassingthwaighte. Nonlinear model for capillary-tissue oxygen transport and metabolism. *Annals of Biomedical Engineering*, 25:604–619, 1997. doi: 10.1007/BF02684839. (cit. on pp. 28)

- [65] Z.-Z. Liang and G.-F. Zhang. SIMPLE-like preconditioners for saddle point problems from the steady Navier–Stokes equations. *Journal of Computational and Applied Mathematics*, 302:211–223, 2016. ISSN 0377-0427. doi: 10.1016/j.cam.2016.02.012. (cit. on pp. 62)
- [66] D. Mackay, W. Shiu, and K. Ma. *Henry’s law constant*, pages 69–87. Routledge, 01 2000. (cit. on pp. 42)
- [67] B. Mao. Lumped parameter model based surgical planning for CABG. In *Medicine in Novel Technology and Devices*, volume 2, page 100014. Medicine in Novel Technology and Devices, 2019. (cit. on pp. 18)
- [68] C. Michler. A computationally efficient framework for the simulation of cardiac perfusion using a multi-compartment Darcy porous-media flow model. *International Journal for Numerical Methods in Biomedical Engineering*, 29(2):217–232, 2013. (cit. on pp. 21, 33)
- [69] C. Michler. A computationally efficient framework for the simulation of cardiac perfusion using a multi-compartment Darcy porous-media flow model. *International Journal for Numerical Methods in Biomedical Engineering*, 29(2):217–232, 2013. (cit. on pp. 36)
- [70] M. E. Moghadam. A modular numerical method for implicit 0d/3d coupling in cardiovascular finite element simulations. *Journal of Computational Physics*, 244: 63–79, 2013. (cit. on pp. 23)
- [71] J. P. Mynard and P. Nithiarasu. A 1d arterial blood flow model incorporating ventricular pressure, aortic valve and regional coronary flow using the locally conservative galerkin (lcg) method. *Communications in Numerical Methods in Engineering*, 24(5):367–417, 2008. (cit. on pp. 19)
- [72] J. P. Mynard and J. J. Smolich. One-dimensional haemodynamic modeling and wave dynamics in the entire adult circulation. *Annals of Biomedical Engineering*, 43(6):1443–1460, 2015. (cit. on pp. 19)
- [73] J. P. Mynard and J. J. Smolich. Influence of anatomical dominance and hypertension on coronary conduit arterial and microcirculatory flow patterns: a multiscale modeling study. *American Journal of Physiology-Heart and Circulatory Physiology*, 311(1):11–23, 2016. (cit. on pp. 23)
- [74] P. K. Nair, J. D. Hellums, and J. S. Olson. Prediction of oxygen transport rates

- in blood flowing in large capillaries. *Microvascular Research*, 38(3):269–285, 1989. ISSN 0026-2862. doi: 10.1016/0026-2862(89)90005-8. (cit. on pp. 24, 25)
- [75] R. Namani, G. S. Kassab, and Y. Lanir. Integrative model of coronary flow in anatomically based vasculature under myogenic, shear, and metabolic regulation. *Journal of General Physiology*, 150(1):145–168, 2018. (cit. on pp. 18)
- [76] New Health Advisor. Systemic and pulmonary circulation, 2022. URL <https://bit.ly/3QKLEBZ>. [Online, accessed in September-2022]. (cit. on pp. 7, 109)
- [77] F. Nolte. Myocardial perfusion distribution and coronary arterial pressure and flow signals: clinical relevance in relation to multiscale modeling, a review. *Medical & biological engineering & computing*, 51(11):1271–1286, 2013. (cit. on pp. 22)
- [78] E. Okun, S. Factor, and E. Kirk. End-capillary loops in the heart: an explanation for discrete myocardial infarctions without border zones. *Science*, 206(4418):565–567, 1979. (cit. on pp. 14)
- [79] O. Ortiz-Pérez. Correspondence between the 17-segment model and coronary arterial anatomy using contrast-enhanced cardiac magnetic resonance imaging. *JACC: Cardiovascular Imaging*, 1(3):282–293, 2008. (cit. on pp. 14)
- [80] T. C. Page, W. R. Light, C. B. McKay, and J. D. Hellums. Oxygen transport by erythrocyte/hemoglobin solution mixtures in an in vitro capillary as a model of hemoglobin-based oxygen carrier performance. *Microvascular research*, 55(1): 54–64, January 1998. ISSN 0026-2862. doi: 10.1006/mvre.1997.2055. (cit. on pp. 25)
- [81] J. Peiró and A. Veneziani. Reduced models of the cardiovascular system. In *Cardiovascular Mathematics*, pages 347–394. Springer Milan, 2009. (cit. on pp. 19)
- [82] O. Pereztol-Valdés et al. Correspondence between left ventricular 17 myocardial segments and coronary arteries. *European Heart Journal*, 26(24):2637–2643, 2005. (cit. on pp. 14)
- [83] Physiology Web. Oxyhemoglobin dissociation curve, 2022. URL <https://bit.ly/3AKxydW>. [Online, accessed in September 2022]. (cit. on pp. 12, 109)
- [84] R. Pietrabissa. A lumped parameter model to evaluate the fluid dynamics of different coronary bypasses. *Medical Engineering & Physics*, 18(6):477–484, 1996. (cit. on pp. 18)

- [85] N. H. J. Pijls and B. De Bruyne. *Coronary Pressure*. Springer Netherlands, 2000. (cit. on pp. 16)
- [86] R. Ponzini, C. Vergara, A. Redaelli, and A. Veneziani. Reliable CFD-based estimation of flow rate in haemodynamics measures. *Ultrasound in medicine biology*, 32: 1545–55, 11 2006. doi: 10.1016/j.ultrasmedbio.2006.05.022. (cit. on pp. 79)
- [87] A. S. Popel. Theory of oxygen transport to tissue. *Critical Reviews in Biomedical Engineering*, 17(3):257–321, 1989. ISSN 0278-940X. (cit. on pp. 23, 24)
- [88] A. Porpora. Numerical treatment of boundary conditions to replace lateral branches in haemodynamics. *Int. J. Numer. Meth. Biomed. Eng.*, 28(12):1165–1183, 2012. (cit. on pp. 50)
- [89] A. Quarteroni and L. Formaggia. Mathematical modelling and numerical simulation of the cardiovascular system. In *Handbook of Numerical Analysis*, volume 12, pages 3–127. Springer, 2004. (cit. on pp. 19)
- [90] A. Quarteroni and A. Valli. *Domain Decomposition Methods for Partial Differential Equations*. Oxford Science Publications, 1999. (cit. on pp. 53)
- [91] A. Quarteroni, R. Sacco, and F. Saleri. *Numerical Mathematics*, volume 37. Springer, 01 2007. ISBN 978-1-4757-7394-1. doi: 10.1007/b98885. (cit. on pp. 61, 62, 63)
- [92] A. Quarteroni, A. Veneziani, and C. Vergara. Geometric multiscale modeling of the cardiovascular system, between theory and practice. In *Computer Methods in Applied Mechanics and Engineering*, volume 302, pages 193–252. Springer, 2016. (cit. on pp. 18, 22)
- [93] A. Quarteroni, L. Dede', A. Manzoni, and C. Vergara. *Mathematical Modelling of the Human Cardiovascular System: Data, Numerical Approximation, Clinical Applications*. Cambridge Monographs on Applied and Computational Mathematics. Cambridge University Press, 2019. doi: 10.1017/9781108616096. (cit. on pp. i, iii)
- [94] A. M. Quarteroni and A. Valli. *Numerical Approximation of Partial Differential Equations*. Springer Publishing Company, Incorporated, 1st ed. 1994. 2nd printing edition, 2008. ISBN 3540852670. (cit. on pp. 62, 63)
- [95] F. Regazzoni. Oxygen exchange model. *Internal MOX Report, Politecnico di Milano*, 2020. (cit. on pp. 31)
- [96] M. Rehman, C. Vuik, and G. Segal. SIMPLE-type preconditioners for the oseen

- problem. *Reports of the Department of Applied Mathematical Analysis, 08-09*, 61, 10 2009. doi: 10.1002/fld.1957. (cit. on pp. 62)
- [97] Y. Saad and M. H. Schultz. GMRES: A generalized minimal residual algorithm for solving nonsymmetric linear systems. *SIAM Journal on Scientific and Statistical Computing*, 7(3):856–869, 1986. doi: 10.1137/0907058. (cit. on pp. 62)
- [98] E. P. Salathe. A mathematical method for determining oxygen distribution in skeletal muscle with multiple capillaries and axial diffusion. *Proceedings: Mathematical, Physical and Engineering Sciences*, 461(2056):975–1004, 2005. ISSN 13645021. (cit. on pp. 29)
- [99] R. S. Schacterle, J. M. Adams, and R. J. Ribando. A theoretical model of gas transport between arterioles and tissue. *Microvascular Research*, 41(2):210–228, 1991. ISSN 0026-2862. doi: 10.1016/0026-2862(91)90023-5. (cit. on pp. 28)
- [100] P. T. Schumacker and R. W. Samsel. Analysis of oxygen delivery and uptake relationships in the Krogh tissue model. *Journal of applied physiology*, 67 3:1234–44, 1989. (cit. on pp. 27)
- [101] T. Secomb, T. Ford, E. Park, and M. Dewhirst. Green’s function methods for analysis of oxygen delivery to tissue by microvascular networks. *Annals of biomedical engineering*, 32:1519–29, 12 2004. doi: 10.1114/B:ABME.0000049036.08817.44. (cit. on pp. 29)
- [102] D. Sengupta. Image-based modeling of hemodynamics in coronary artery aneurysms caused by kawasaki disease. *Biomechanics and Modeling in Mechanobiology*, 11(6):915–932, 2012. (cit. on pp. 23)
- [103] N. Shenoy, R. Luchtel, and P. Gulani. Considerations for target oxygen saturation in Covid-19 patients: are we under-shooting? *BMC Medicine*, 18(1):1–6, 2020. (cit. on pp. 87)
- [104] D. U. Silverthorn et al. Human physiology: an integrated approach, 2016. (cit. on pp. 2, 109)
- [105] M. D. Sinclair. Measurement and modeling of coronary blood flow. *Wiley Interdisciplinary Reviews: Systems Biology and Medicine*, 7(6):335–356, 2015. (cit. on pp. 19)
- [106] N. P. Smith, A. J. Pullan, and P. J. Hunter. An anatomically based model of transient coronary blood flow in the heart. *SIAM Journal on Applied Mathematics*, 62(3):990–1018, 2002. (cit. on pp. 19, 23)

- [107] J. A. Spaan, N. P. Breuls, and J. D. Laird. Diastolic-systolic coronary flow differences are caused by intramyocardial pump action in the anesthetized dog. *Circulation Research*, 49(3):584–593, 1981. (cit. on pp. 19)
- [108] J. A. E. Spaan et al. Visualisation of intramural coronary vasculature by an imaging cryomicrotome suggests compartmentalisation of myocardial perfusion areas. *Medical and Biological Engineering and Computing*, 43(4):431–435, 2005. (cit. on pp. 14)
- [109] C. A. Taylor, T. A. Fonte, and J. K. Min. Computational fluid dynamics applied to cardiac computed tomography for noninvasive quantification of fractional flow reserve. *Journal of the American College of Cardiology* 61.22, pages 2233–2241, 2013. (cit. on pp. 17)
- [110] M. Termeer et al. Visualization of myocardial perfusion derived from coronary anatomy. *IEEE Transactions on Visualization and Computer Graphics*, 14(6):1595–1602, 2008. (cit. on pp. 14)
- [111] T. Tezduyar. Stabilized finite element formulations for incompressible flow computations. *Advances in Applied Mechanics*. Elsevier, 28:1 –44, 1991. (cit. on pp. 53)
- [112] L. Tobiska and G. Lube. A modified streamline diffusion method for solving the stationary Navier–Stokes equation. *Numerische Mathematik*, 59(1):13–29, 1991. (cit. on pp. 53)
- [113] S. M. Vahidhosseini, E. Barati, and J. A. Esfahani. Green’s function method (GFM) and mathematical solution for coupled equations of transport problem during convective drying. *Journal of Food Engineering*, 187:24–36, 2016. ISSN 0260-8774. doi: 10.1016/j.jfoodeng.2016.04.017. (cit. on pp. 29)
- [114] A. van der Horst. Towards patient-specific modeling of coronary hemodynamics in healthy and diseased state. In *Computational and Mathematical Methods in Medicine*, pages 1–15. Computational and Mathematical Methods in Medicine, 2013. (cit. on pp. 23)
- [115] W. J. Vankan. Finite element analysis of blood flow through biological tissue. *International Journal of Engineering Science*, 35(4):375–385, 1997. (cit. on pp. 21, 33)
- [116] L. Vera. A 1D computer model of the arterial circulation in horses: An important

- resource for studying global interactions between heart and vessels under normal and pathological conditions. *PLOS ONE*, 14(8):0221425, 2019. (cit. on pp. 19)
- [117] C. Vergara. Nitsche's method for defective boundary value problems in incompressible fluid-dynamics. *J Sci Comp*, 46(1):100–123, 2011. (cit. on pp. 50)
- [118] E. Vidotto. Hybrid models for simulating blood flow in microvascular networks. *Multiscale Modeling Simulation*, 17(3):1076–1102, 2019. (cit. on pp. 50)
- [119] A. T. Vuong, L. Yoshihara, and W. A. Wall. A general approach for modeling interacting flow through porous media under finite deformations. *Computer Methods in Applied Mechanics and Engineering*, 283:1240–1259, 2015. (cit. on pp. 21)
- [120] N. Westerhof et al. Cross-talk between cardiac muscle and coronary vasculature. *Physiological Reviews*, 86(4):1263–1308, 2006. (cit. on pp. 15, 16, 19)
- [121] P. A. Wieringa, H. G. Stassen, J. J. Van Kan, and J. A. Spaan. Oxygen diffusion in a network model of the myocardial microcirculation. *Int J Microcirc Clin Exp*, 13:137–169, 1993. (cit. on pp. 30)
- [122] C. Zakkaroff et al. Patient-specific coronary blood supply territories for quantitative perfusion analysis. *Computer Methods in Biomechanics and Biomedical Engineering: Imaging & Visualization*, 6(2):137–154, 2016. (cit. on pp. 14)
- [123] D. Zinemanas, R. Beyar, and S. Sideman. Effects of myocardial contraction on coronary blood flow: an integrated model. *Annals of biomedical engineering*, 22(6):638–652, 1994. (cit. on pp. 18)
- [124] D. Zinemanas, R. Beyar, and S. Sideman. An integrated model of LV muscle mechanics, coronary flow, and fluid and mass transport. *American Journal of Physiology-Heart and Circulatory Physiology*, 268(2):633–645, 1995. (cit. on pp. 19)
- [125] A. Zingaro, I. Fumagalli, L. Dede, M. Fedele, P. C. Africa, A. F. Corno, and A. Quarteroni. A geometric multiscale model for the numerical simulation of blood flow in the human left heart. *Discrete and Continuous Dynamical Systems - S*, 15(8):2391–2427, 2022. (cit. on pp. 53)
- [126] Zygote Media Group Inc. Zygote solid 3D heart generation II developement report. Tech. rep., Zygote Media Group Inc, 2014. (cit. on pp. 77)

List of Figures

1.1	Illustration of the human heart [104].	2
1.2	Anatomy of the main coronary arteries [40].	4
1.3	Events of the cardiac cycle for the left ventricle (Wiggers diagram) [39].	6
1.4	Systemic and pulmonary circulation [76].	7
1.5	Oxyhemoglobin dissociation curve [83].	12
1.6	Segmental analysis of left ventricle based on schematic view [25].	14
1.7	Polar plot of perfusion regions [25].	15
2.1	Sketch of the computational domain for the epicardial coronary arteries [25].	32
2.2	Schematic overview of the multi-compartment porous medium in a piece of myocardium in case of three compartments [25].	33
2.3	Design of multi-physics oxygenation model.	49
4.1	Results of the 0D model in physiological scenario.	66
4.2	Comparison between reduced and complete model.	69
4.3	Idealized geometry of myocardium Ω_M	70
4.4	Comparison between 3D and 0D model.	71
4.5	Comparison between semi-coupled and uncoupled model.	73
4.6	Idealized geometries of coronaries Ω_C (cylinder) and myocardium Ω_M (cube).	74
4.7	Magnitude of \mathbf{u}_C (left) and p_C (right) on Ω_C at peak of the (parabolic) velocity profile ($t = 0.4$ s).	75
4.8	Comparison between coupled and semi-coupled model.	76
4.9	Computational domains: coronaries (Ω_C) and myocardium (Ω_M).	78
4.10	Perfusion regions in different myocardium views.	78
4.11	Permeability tensors \mathbf{K}_i	79
4.12	Pressure-coupling coefficients $\beta_{i,j}$	79
4.13	Ψ_{CBF} profile imposed in simulated scenarios.	80
4.14	Scalar fields of the multi-physics oxygenation model in scenario of a healthy subject.	82
4.15	Comparison between real and idealized geometries.	83

4.16 Scalar fields of the multi-physics oxygenation model in scenario of a healthy subject under physical activity.	84
4.17 Effects of physical activity on a healthy subject.	86
4.18 Scalar fields of the multi-physics oxygenation model in scenario of patient with SARS-CoV-2.	88
4.19 Effects of SARS-CoV-2 infection.	90
4.20 Scalar fields of the multi-physics oxygenation model in scenario of a patient with SARS-CoV-2 and under physical activity.	91
4.21 Effects of physical activity on a patient with SARS-CoV-2.	92

List of Tables

2.1	List of fluid dynamics parameters.	33
2.2	List of Darcy problem parameters.	36
2.3	List of oxygenation model parameters.	46
2.4	List of oxygenation model parameters for the uncoupled case.	47
2.5	List of α^j parameters for each perfusion region j	51
4.1	Correspondences between CBF points and simulation times.	81
4.2	Comparison between space-temporal minimum, average and maximum values at rest and under physical activity scenarios.	85
4.3	Pathological parameters to simulate scenario of SARS-CoV-2 infection. . .	87
4.4	Comparison between space-temporal minimum, average and maximum values of healthy and SARS-CoV-2 scenarios.	89
4.5	Comparison between space-temporal minimum, average and maximum values at rest and under physical activity scenarios.	93

List of Symbols

Variable	Measure unit	Description
x	—	spatial coordinate
n, τ_i	—	normal and two tangential versors to a surface
Pe	—	Péclét number
\mathbf{u}_C	m s^{-1}	blood velocity in coronaries
\mathbf{u}_i	m s^{-1}	blood velocity in comp. i
ρ	kg m^{-3}	blood density
ρ_i	kg m^{-3}	effective blood density in comp. i
μ_C	mmHg s	blood viscosity
μ	$\text{m}^2 \text{s}^{-1}$	diffusion coefficient in oxygenation model
p_C	mmHg	blood pressure in coronaries
p_i	mmHg	blood pressure in comp. i
p_{veins}	mmHg	blood pressure in venous system
\mathbf{K}_i	$\text{m}^2 \text{s}^{-1} \text{mmHg}^{-1}$	permeability tensor of Darcy in comp. i
$\beta_{i,j}$	$\text{mmHg}^{-1} \text{s}^{-1}$	pressure coupling coefficients of Darcy between comp. i, j
g_i	s^{-1}	volumetric source or sink term of Darcy
γ	$\text{mmHg}^{-1} \text{s}^{-1}$	drain coefficient of Darcy
ψ_i	—	volume fraction occupied by comp. i
$\Phi_{i,j}$	mmHg	mass flux per tissue unit volume between comp. i, j
$\widehat{\phi}_{i,j}$	m s^{-1}	volume flux per tissue unit volume between comp. i, j
n	—	hemoglobin's binding sites for oxygen
k_+, k_-	s^{-1}	association/dissociation rate constant
$[X]$	mol m^{-3}	concentration of the chemical specie X
$\frac{A_v^i}{V_t}$	m^{-1}	vascular surface area per tissue unit volume in comp. i
$P, (\tilde{P})$	$\text{m}^3 \text{s}^{-1} \text{m}^{-2}$	(effective) membrane permeability
$\lambda_{\text{O}_2}^{\text{del}}$	mol m^{-3}	average oxygen amount delivered to the muscle
$\lambda_{\text{O}_2}^{\text{cons}}$	mol m^{-3}	average oxygen amount consumed by the muscle
$\Lambda_{\text{O}_2}^{\text{del}}$	$\text{mol m}^{-3} \text{s}^{-1}$	total oxygen amount delivered to the muscle
$\Lambda_{\text{O}_2}^{\text{cons}}$	$\text{mol m}^{-3} \text{s}^{-1}$	total oxygen amount consumed by the muscle
SO_2	—	oxygen saturation
α	$\text{mmHg m}^3 \text{mol}^{-1}$	Henry law's constant
ξ_0	$\text{mol m}^{-3} \text{s}^{-1}$	maximum oxygen consumption rate
$\tilde{\xi}_0$	$\text{mol m}^{-3} \text{s}^{-1}$	effective maximum oxygen consumption rate
$\text{PO}_2, (\text{PO}_2^m)$	mmHg	O_2 partial pressure (in muscle)
$\text{PO}_2^{50}, (\text{PO}_2^{m,50})$	mmHg	half maximal effective partial pressure (in muscle)
Φ_M	s^{-1}	blood flux magnitude for uncoupled model
T_{HB}	s	blood flux heart beat period for uncoupled model
α^j	$\text{m}^3 \text{s}^{-1} \text{mmHg}^{-1}$	conductance between arteries and porous medium
$\Psi_{\text{CBF}}, (\bar{\Psi}_{\text{CBF}})$	$\text{mL min}^{-1} \text{g}^{-1}$	(averaged) CBF supplying the myocardium

